Multi-Isotope Multi-Pinhole SPECT Imaging in Small Laboratory Animals

Experimental Measurements and Monte Carlo Simulations

Mathias Lukas

Aus der Klinik für Nuklearmedizin
der medizinischen Fakultät Charité – Universitätsmedizin Berlin

Dissertation

Multi-Isotope Multi-Pinhole SPECT Imaging in Small Laboratory Animals

Experimental Measurements and Monte Carlo Simulations

Multi-Isotope Multi-Pinhole SPECT Bildgebung in kleinen Labortieren

Experimentelle Messungen und Monte Carlo Simulationen

zur Erlangung des akademischen Grades
Doctor of Philosophy (PhD)

vorgelegt der Medizinischen Fakultät
Charité – Universitätsmedizin Berlin

von

Mathias Lukas

Datum der Promotion: 30.11.2023

Abstract

Single photon emission computed tomography (SPECT) in small laboratory animals has become an integral part of translational medicine. It enables non-invasive validation of drug targeting, safety and efficacy in living organisms, which is progressively gaining importance in pharmaceutical industry.

The increasing demand for efficiency in pharmaceutical research could be addressed by novel multi-tracer study designs. Multi-isotope multi-pinhole sampling allows validation of multiple tracers in a single experiment and consolidation of consecutive research trials. Due to physical and technical limitations, however, image quality and quantification can be substantially reduced. Advanced corrective procedures are required to establish multi-isotope multi-pinhole SPECT as a reliable and quantitative imaging technique for widespread use.

For this purpose, the present work aimed to investigate the technical capabilities and physical limitations of multi-isotope multi-pinhole SPECT imaging in small laboratory animals. Based on experimental measurements and Monte Carlo simulations, specific error sources have been identified and procedures for quantitative image correction have been developed. A Monte Carlo simulation model of a state-of-the art SPECT/CT system has been established to provide a generalized framework for in-silico optimization of imaging hardware, acquisition protocols and reconstruction algorithms.

The findings of this work can be used to improve image quality and quantification of SPECT in-vivo data for multi-isotope applications. They guide through the laborious process of multi-isotope protocol optimization and support the 3R welfare initiative that aims to replace, reduce and refine animal experimentation.

Kurzfassung

Die Einzelphotonen-Emissionscomputertomographie (SPECT) in kleinen Labortieren hat sich als wichtiger Bestandteil der translationalen Medizin etabliert. Sie ermöglicht die nicht-invasive Validierung der Zielgenauigkeit, Wirksamkeit und Sicherheit von Wirkstoffen in lebenden Organismen und gewinnt zunehmend an Bedeutung in der pharmazeutischen Industrie.

Die Forderung nach mehr Effizienz in der pharmazeutischen Forschung könnte durch neuartige Multitracer-Studien adressiert werden. Die Multi-Isotopen Akquisition mit Multi-Pinhole Kollimatoren ermöglicht die Validierung mehrerer Tracer in einem einzelnen Experiment und die Konsolidierung konsekutiver Bildgebungsstudien. Aufgrund physikalischer und technischer Limitationen ist die Bildqualität und Quantifizierbarkeit bei diesem Verfahren jedoch häufig reduziert. Um die Multi-Isotopen SPECT als zuverlässige und quantitative Bildgebungsmethode für den breiten Einsatz zu etablieren, sind komplexe Korrekturverfahren erforderlich.

Ziel der vorliegenden Arbeit war daher, die technischen Möglichkeiten und physikalischen Limitationen der Multi-Isotopen SPECT-Bildgebung in kleinen Labortieren systematisch zu untersuchen. Mithilfe von experimentellen Messungen und Monte Carlo Simulationen wurden spezifische Fehlerquellen identifiziert und Verfahren zur quantitativen Bildkorrektur entwickelt. Zudem wurde das Monte-Carlo Modell eines neuartigen SPECT/CT-Systems etabliert, um eine Plattform für die in-silico Optimierung von Bildgebungshardware, Aufnahmeprotokollen und Rekonstruktionsalgorithmen zu schaffen.

Die Ergebnisse dieser Arbeit können die Bildqualität und Quantifizierbarkeit von SPECT in-vivo Daten für Multi-Isotopen Anwendungen verbessern. Sie führen beispielhaft durch den Prozess der Multi-Isotopen Protokolloptimierung und unterstützen die 3R-Initiative mit dem Ziel, experimentelle Tierversuche zu vermeiden (Replace), zu vermindern (Reduce) und zu verbessern (Refine).

Contents

List of Abbreviations

APD	Avalanche Photo Diode
CPU	Central Processing Unit
CT	Computed Tomography
CZT	Cadmium Zinc Telluride
FBP	Filtered Back-Projection
FOV	Field Of View
FWHM	Full Width at Half Maximum
Gate	Geant4 Application for Tomographic Emission
Geant4	GEometry And Tracking
GPU	Graphics Processing Unit
MRI	Magnetic Resonance Imaging
MRS	Magnetic Resonance Spectroscopy
OSEM	Ordered Subset Expectation Maximization
PET	Positron Emission Tomography
PMT	Photomultiplier Tube
SPECT	Single Photon Emission Computed Tomography
SSD	Solid-State Detectors

List of Symbols

α	Pinhole acceptance angle
ε	Collimator collection efficiency
ϵ_0	Vacuum permittivity
ϑ	Electron scatter angle
θ	Photon incidence angle
λ	Spatial resolution
μ	Linear attenuation coefficient
μ/ρ	Mass attenuation coefficient
ρ	Volumetric mass density
σ	Photon cross section
φ	Photon scattering angle
ϕ	Detector rotation angle
Φ	Photon flux
A	Detector surface
$\mathcal{B}$	Back-projection
$c_{1\|2}$	Photopeak intersection
d	Pinhole diameter, Material thickness
E_B	Electron binding energy
E_e	Electron energy
E_ν	Photon energy
ΔE_ν	Energy resolution
ΔE_w	Energy window
$f(x, y)$	Activity distribution
h	Focal distance
M	Magnification factor, Molar mass
$m_e c^2$	Electron rest energy
N	Photon count
$\dot{N}$	Photon count rate
N_A	Avogadro constant
$p(r, \phi)$	Angular projection
r_0	Classical electron radius
S	Object or image size
$\mathcal{R}$	Radon transform
$\vec{p}_e$	Electron momentum
$\vec{p}_\nu$	Photon momentum
x_m, y_n	Image grid coordinates
Z_e	Effective atomic number

List of Figures

1 Introduction

In recent years, single photon emission computed tomography (SPECT) in small laboratory animals has become an integral part of translational medicine. It enables fast validation of drug targeting, safety and efficacy at reasonable costs and is therefore progressively establishing as a key technology for pharmaceutical industry [1]. (Chapter 3.1)

SPECT imaging is based on tracer principle and external radiation detection, utilizing the physicochemical properties of radioisotopes to transform molecular signals into spatiotemporal information [2]. Linked to molecular probes, γ- and x-ray emitting isotopes can be traced in space and time to characterize biological processes in living organisms. Therefore, it is a powerful tool for non-invasive imaging of physiological and pathological pathways down to the picomolar range [3]. (Chapter 3.2)

A strength of SPECT is its capability to image multiple radioisotopes simultaneously based on spectral separation of individual emission energies. This enables the visualization and characterization of multiple molecular pathways and their mutual interaction in single experiments. Particularly for rapidly changing pathophysiology, temporal information cannot be assessed by consecutive trials. Multi-isotope SPECT imaging, therefore, can be valuable for comparative studies [4], competing studies [5] and dose-response assessment in therapeutic applications [6]. It also can improve the experimental throughput by parallelizing sequential study designs. (Chapter 3.3)

However, the technical demand on preclinical SPECT is high. Imaging objects are small and physiological processes are fast compared to clinical studies. Small injection volumes, low count rates as well as a variety of non-conventional radioisotopes need to be handled, while data acquisition should be fast, sensitive and quantitative at once. Recent advances in SPECT instrumentation, therefore, aimed to improve accuracy especially for small animal applications [7]. The physically limited spatial resolution of scintillation detectors has been overcome by the magnifying nature of pinhole collimation and multiplexing of multiple pinholes could increase count rate sensitivity [8]. Adoption of iterative reconstruction algorithms enabled sparse data sampling for fast acquisition schemes [9, 10] and novel detector designs further improved energy resolution for multi-isotope applications [11]. (Chapter 3.4, Chapter 3.5)

Still, multiplexed multi-pinhole SPECT operates at the edge of technological feasibility and simultaneous sampling of multiple isotopes introduces additional interferences that degrade image quality and quantification [12]. Decomposition of such error sources is required, albeit challenging, but can be approached by Monte Carlo simulations [13]. Based on repeated random variable sampling and first principles of physics, Monte Carlo simulations are well suited to address a variety of problems that are difficult to study by experimental techniques [14]. (Chapter 3.6)

However, only few investigations have been published on quantitative accuracy, all related to specific applications [15, 16]. A systematic and comprehensive assessment of errors for multi-isotope multi-pinhole SPECT is missing so far. Identification of specific error sources and derivation of corrective procedures is required to establish multiplexed multi-isotope multi-pinhole SPECT as a reliable and quantitative imaging technique for the molecular imaging community.

2 Research Objectives

A state-of-the-art small animal NanoSPECT/CT system has been installed at Charité Berlin and a 3R initiative aims to replace, reduce and refine animal experimentation. There is an increasing demand for scientific and economic efficiency that should be addressed by multi-tracer study designs.

For this purpose, multi-isotope multi-pinhole SPECT imaging should be established in small laboratory animals. Specific error sources should be identified and procedures for quantitative correction should be developed.

In a first study, the multi-isotope capabilities of the imaging system have been evaluated. Basic performance parameters, limitations and error sources have been quantified and assessed for multiple radioisotopes. Due to the lack of standards, numerous experimental and mathematical procedures had to be established.

In a second study, a Monte Carlo simulation model of the imaging system has been developed with emphasis on high accuracy for multi-isotope applications. The model provides accurate information on attenuation, scatter and spectral crosstalk for quantitative correction of multi-isotope SPECT in-vivo data. It can also be used as substitute for preliminary animal experiments in the process of multi-isotope protocol optimization.

3 Theoretical Background

The focus of this thesis is on measurement and simulation of multi-isotope multi-pinhole SPECT in small laboratory animals. This section elaborates the theoretical principles that have been used to deduce the experimental procedures and to interpret the results. For a more detailed treatise please refer to the technical literature [3, 14, 17, 18].

3.1 Molecular Imaging

Molecular imaging refers to the use of non-invasive imaging techniques for visualization and characterization of biological processes at the molecular level in living organisms. It can provide information about the spatial distribution and expression level of specific molecular targets over time, as well as changes in their functional activity due to physiological or pathological stimuli. Targets may be gene products such as receptors or enzymes, but can also be gene reporter molecules in experimental animals with specifically inserted genes [3]. The ability to quantify metabolic rates, binding affinities and uptake ratios of molecular probes makes molecular imaging a valuable tool for diagnostic and therapeutic applications in basic pharmaceutical science.

However, different molecular imaging techniques are available including Single Photon Emission Computed Tomography (SPECT), Positron Emission Tomography (PET), Magnetic Resonance Imaging (MRI), Magnetic Resonance Spectroscopy (MRS), Bioluminescence and Fluorescence. Differences in the underlying physical principles determine their sensitivity, specificity, spatial resolution and possible time of observation, characteristics that have to be traded off according to the biological question under study (Figure 3.1 A). SPECT and PET have become among the leading technologies as they provide advantageous imaging characteristics, a combination of exquisite sensitivity, spatial resolution, signal-tissue penetration depth and quantifiability [3].

Both, PET and SPECT are based on tracer principle and external radiation detection. Molecular probes labeled with radioisotopes are brought inside a subject, usually by intravenous injection, where they can be traced in space and time non-invasively. Due to the high detection efficiency of emission tomography, the amount of tracer required is only in the order of nano- to micrograms compared to several grams for other modalities. This enables virtual unlimited selection of possible carrier molecules as tracer since the toxicity always is a function of dosage.

However, SPECT offers several advantages over PET, particularly in small animal research. The spatial resolution of SPECT, for example, is not limited by nature [17]. In PET, positrons travel a finite distance before annihilating with an electron, which places a fundamental physical limit. After annihilation, the photon pair detected by the PET instrumentation originates from a location that is different from the positron source, which results in energy-depended spatial blurring. The acollinearity of annihilation photons arising from momentum conservation during the electron-positron annihilation process and parallax effects caused by finite detector elements further degrade image resolution. Therefore, the spatial resolution of PET ranges between 0.5 mm (^{18}F) and 2.8 mm (^{68}Ga), depending on the radioisotope used. SPECT, by contrast, utilizes photon-emitting isotopes that can be localized without displacement, allowing spatial resolutions down to the submillimeter range.

A second advantage of SPECT is its ability to image slow kinetics and therefore endogenous ligand interactions (Figure 3.1 B). Peptides, antibodies, hormones and selectins, for example, are relatively large molecules, which diffuse slowly into tissue and have slow clearance from blood [3]. The time required for localization and clearance favors radioisotopes with longer half-lives such as

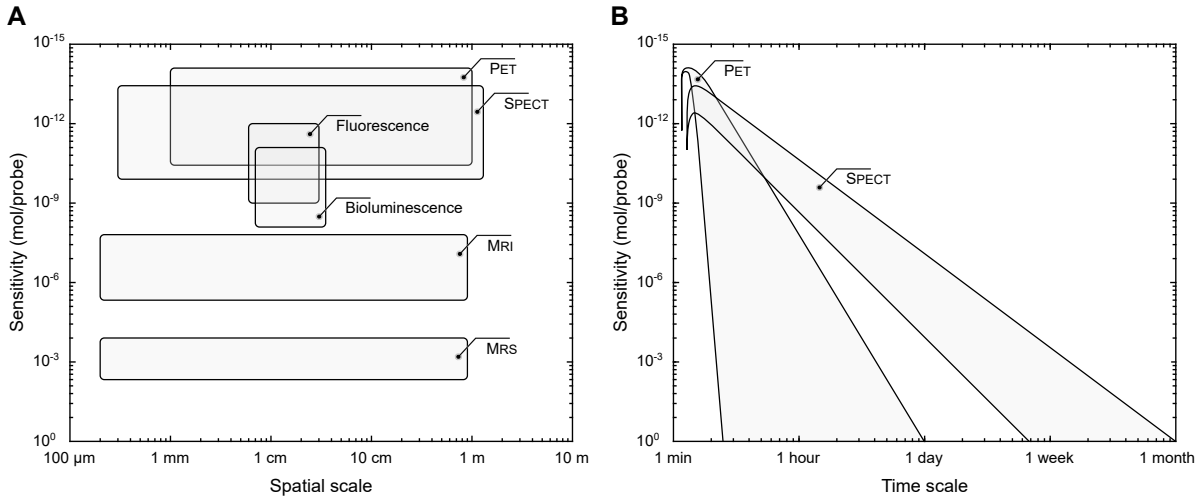

Figure 3.1. Sensitivity matrix of molecular imaging modalities with respect to their spatial (A) and temporal (B) capabilities. SPECT occupies an important niche in the molecular imaging matrix. It offers high sensitivity, spatial resolution and penetration depth as well as a wide time window for observation. Sensitivity (mol/probe) refers to the in vivo concentration of the labeled contrast agent required to elicit a certain signal-to-noise ratio. The spatial scale is the domain bounded by the limiting resolution (left limit) and the depth of penetration of the signal-generating radiation (right limit) for a given technology. The time scale is defined by the decay properties of commonly used radioisotopes in SPECT and PET, respectively. (adapted from Meikle et al. [3])

^{99m}Tc (6.02 h), ^{123}I (13.2 h) and ^{111}In (2.8 days) commonly used in SPECT. Positron emitters for PET, such as ^{11}C (20 min) and ^{18}F (109 min), show relatively short half-lives making them less well suited for labeling of endogenous biomolecules. The production of such short living positron emitters also requires expensive instrumentation and their bonding to probes involves complex organic-synthetic chemistry. SPECT tracers usually do not require specialist radiochemistry expertise or facilities, which substantially reduces the lead time for probe development and broadens the range of biological targets that can be studied.

Another promising advantage of SPECT, although not yet well studied, is the ability to image multiple molecular pathways in a single subject simultaneously. SPECT is able to separate different photon energies and thus multiple radioisotopes, which enables access to a variety of scientific applications that cannot be addressed by sequential experimentation. Multi-isotope labeling of single probe substructures, for example, allow kinetic study of metabolic cleavage. Multi-isotope labeling of multiple probes, on the other hand, can be used to study mutual interactions of comparative or competing molecular processes. Multi-isotope SPECT imaging, therefore, holds great potential but is not yet established for widespread use. It is affected by physical and technical perturbations degrading image quality and quantification [19]. A systematic evaluation of quantitative accuracy and the development of corrective procedures is required and a major objective of the present work.

In conclusion, SPECT occupies an important niche in the molecular imaging matrix. It allows observation of processes that span a time window from minutes to weeks and has no physical limit on spatial resolution. Shortened lead times for probe labeling and, in particular, the unique ability to image multiple radioisotopes simultaneously make it a powerful tool for a wide range of scientific applications.

3.2 SPECT Imaging

SPECT is a molecular imaging technique used to measure the spatial and temporal distribution of radiolabeled tracers in living organisms. The tracers are brought into the subject by injection, ingestion or inhalation to participate in biochemical processes. Due to nuclear decay of the ligated radioisotope, characteristic γ- or x-ray photons are emitted, which may leave the subject and can be detected. The rate of this emission within a given volume corresponds to the concentration of the radiotracer and can be related to a functional activity.

In SPECT, the radiation signal is acquired by one or more gamma cameras that are rotated around the imaging object to obtain three-dimensional information on the tracer distribution (Figure 3.2 A). Each detector head is equipped with a mechanical collimator to define the direction of the incident photon, a converter material for photon energy moderation and readout electronics for position-sensitive data sampling (Figure 3.2 B). Photons that pass the collimator can be absorbed by the converter material and generate an electronic signal attributed with incident time, energy and position for further processing. The signals are arranged into a stack of two-dimensional matrices representing the spatial distribution of the detected events for different angular views. The angular projections can be used to reconstruct three- or even four-dimensional activity distributions for biological interpretation.

However, the sensitivity and spatial resolution of a SPECT system is largely defined by its collimator design. Parallel-hole collimators are often used in clinical practice due to their large field of view relative to the sensitive detector size (Figure 3.3 A). Their sensitivity and resolution can be modified by variation of septum length and thickness, but are limited by the intrinsic properties of the radiation detector itself. Cone-beam collimators with converging septa can increase volume sensitivity and resolution for a smaller field of view, which is why they are frequently used to image organs of smaller size (Figure 3.3 B). Pinhole collimation, finally, enables submillimeter resolution by object magnification, setting the stage for small animal imaging in basic science (Figure 3.3 C). A variety of other collimators is available, optimized for different isotopes and applications. The field of view, sensitivity and resolution, however, is always a trade-off and must be chosen with care.

The intrinsic sensitivity and energy resolution of a detector system depends on the converter material and readout electronics used. The converters usually consist of high-density materials

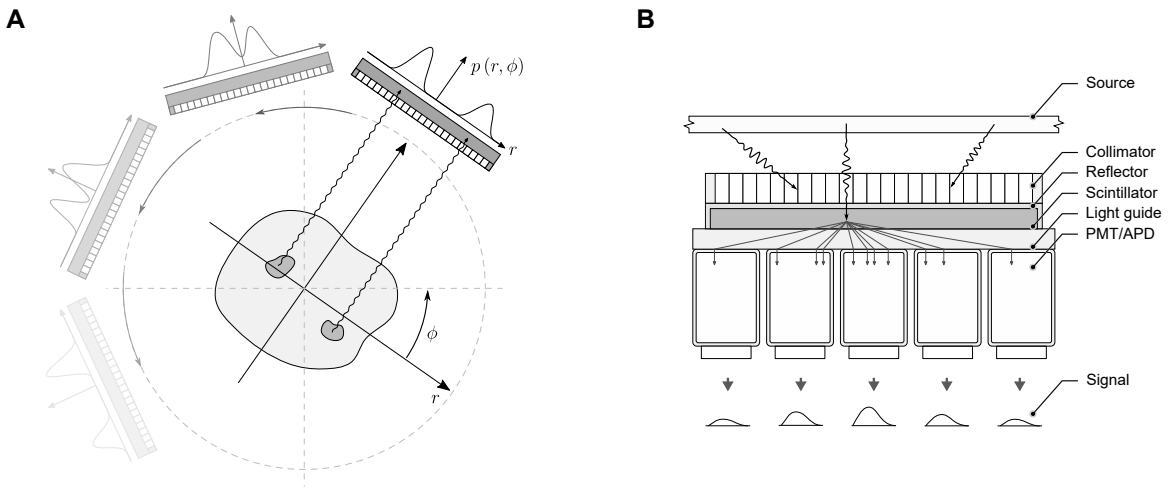

Figure 3.2. Data acquisition scheme of a SPECT gantry (A) and gamma detector (B). The gantry consists of one or multiple detector heads rotating around the imaging object to acquire projections of the radioactivity distribution from different angular views (A). Each detector head consists of a collimator to define the geometric properties of the incident radiation field, a scintillator for energy absorption, a reflector for light collection, a light guide for light distribution, and multiple position-sensitive photodetectors for electronic signal formation (B).

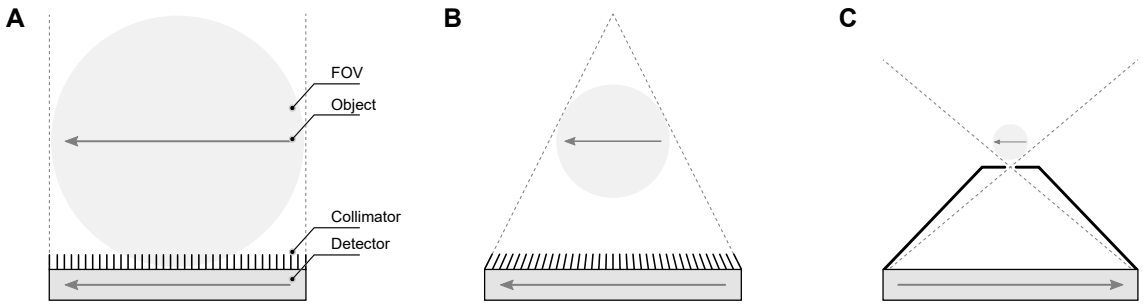

Figure 3.3. Schematic representation of parallel-hole (A), cone-beam (B), and pinhole (C) collimation used for SPECT imaging. The field of view (FOV), sensitivity and spatial resolution of each collimator is a trade-off that needs to be adapted to specific radioisotopes and applications.

such as thallium-doped sodium iodine (NaI(Tl)) or Cadmium Zinc Telluride (CZT) to increase the probability for incident photons to be absorbed. Compton scattering and photoelectric absorption induce electron-hole pairs in the converter material that can be sensed as electronic signal using different ionization detection schemes (Figure 3.4 A).

In scintillation-based detectors, e.g. based on NaI(Tl), the absorbed energy is transferred to luminescent centers of the scintillator, which radiate scintillation photons accompanied by a cascade of secondary x-ray, Auger electrons, vibration excitations or combinations thereof (Figure 3.4 A). Thus, the incident photon is converted into multiple photons with lower energy that can be detected more efficiently. The scintillation light is distributed to an array of photomultiplier tubes (PMT) or avalanche photo diodes (APD) via light guide to enable position sensitive detection (Figure 3.2 B). By weighting the position of each PMT or APD with its signal intensity, the location of the ionizing event can be derived as centroid. The total sum of all PMT or APD signals in the array is proportional to the photon energy absorbed by the converter.

In contrast, solid-state detectors (SSD, e.g. based on CZT) are capable to detect high-energy photons more directly by discharge of the electric current generated by the ionization process itself (Figure 3.4 A). They usually consist of pixelated materials and readout electronics that allow straight localization of each ionization event. However, for all detector designs, high-voltage capacitor-resistor circuits finally provide electric voltages that are proportional to the energy and position of the incident photon flux. These signals are digitalized and saved in projection matrices that can be further processed.

Both direct- and indirect-converting detector schemes have their pros and cons, especially for multi-isotope applications. Scintillators, for example, are well established and highly efficient, but non-proportional light yield due to imperfect crystal structures can impair the intrinsic resolution (NaI: ~10 % at 140 keV) and long luminescence decay times (NaI: 250 ns) may cause dead-time effects. CZT detectors, on the other hand, show excellent energy resolutions (CZT: ~6 % at 140 keV) but are affected by non-proportional charge carrier effects. Self-shielding of the electric field during electron-hole transport leads to asymmetric photopeaks with low-energy tails (Figure 3.4 B). The extent of this spectrum shift depends on both photon flux and energy, which is why it is hard to predict.

In the present work, scintillation based NaI(Tl) detectors are used together with PMTs. Their high efficiency and well-predictable signal response are favorable for the study of multi-isotope applications.

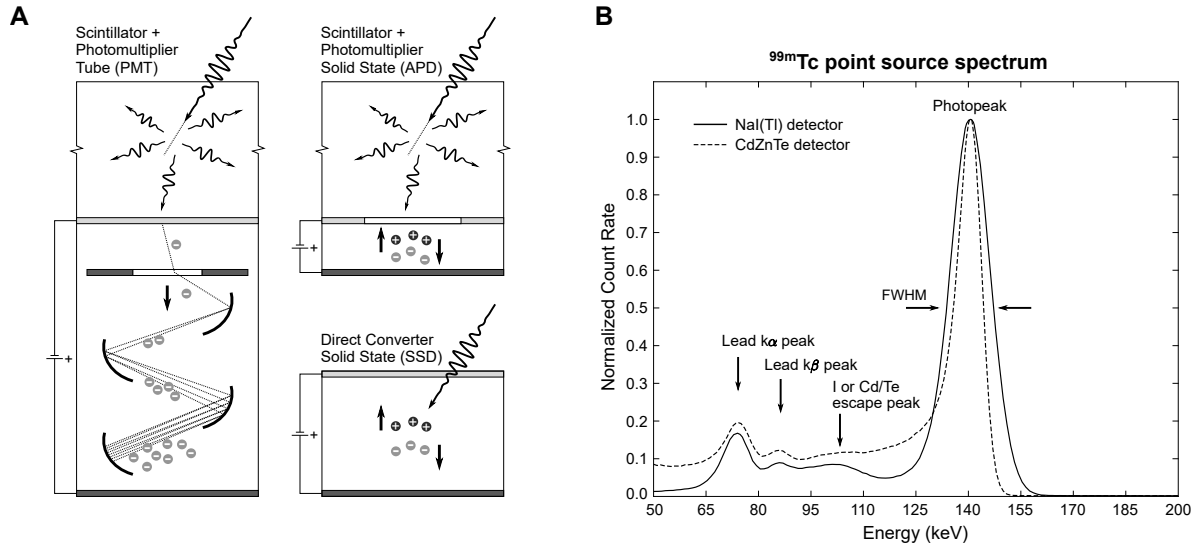

Figure 3.4. Detection principle (A) and count rate spectra (B) for different radiation detector designs. Incident photons are absorbed by converter materials mainly due to Compton scattering and photoelectric absorption. The resultant ionization of the converter material can be detected either directly (SSD) or indirectly via detection of scintillation light (PMT, APD) (A). Direct conversion provides higher energy resolution but suffers from asymmetric photopeaks with low-energy tails (B). SSD refers to solid-state detectors, PMT to photomultiplier tubes, and APD to avalanche photo diodes.

3.3 Multi-Isotope SPECT

3.3.1 Basic Principles

SPECT imaging is based on the detection of photon radiation that is emitted by unstable isotopes due to their nuclear decay. Each radioisotope has a characteristic de-excitation scheme that differs in mode, rate and energy. Different radioisotopes, therefore, can be distinguished by spectral separation of their individual emission energies. The simultaneous sampling of multiple isotopes becomes possible if detected photopeaks are characteristic and do not interfere (Figure 3.5)[19].

Technically, projection data are recorded with isotope-specific energy windows that need to be adapted to the particular application. Energy windows discriminate photons that are assumed to be not associated with the primary radiation of the intended radioisotope. For multi-isotope acquisitions, multiple energy windows can be used to generate a data set for each individual isotope. These data sets then can be reconstructed to multiple single-isotope SPECT images. The number of radioisotopes that can be acquired simultaneously is limited only by technical reasons, but each additional isotope increases spectral interference and further degrades image quality.

3.3.2 Radioisotopes

For diagnostic imaging, radioisotopes with gamma decay are often preferred (Figure 3.6 A). Gamma photons are emitted by excited nuclei during the transition from high- to low-energy states. Due to quantized nuclear excitation levels, the energy of gamma photons can be considered well defined. However, nuclear de-excitation is often accompanied by other forms of physical decay. Characteristic x-ray, for example, is generated by the release of inner shell electrons and subsequent de-excitation of the atomic shell. Gamma emitters can also have significant probabilities for particle decay, which can be utilized for therapeutic applications (Figure 3.6 B). The gamma component of such theranostic isotopes is usually overlaid by a continuous spectrum of Bremsstrahlung, but can still be imaged with acceptable validity.

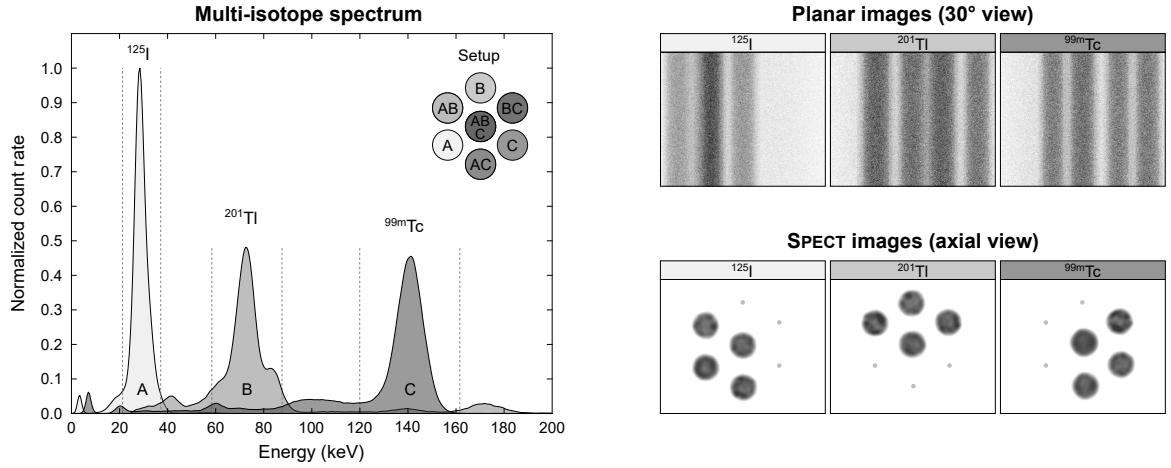

Figure 3.5. Acquisition scheme of a multi-isotope experiment with advantageous photopeak distribution. Multiple energy windows can be used for spectral separation of individual photopeaks. Projections are generated for each radioisotope and can be reconstructed to multiple single-isotope SPECT images. Image quality may be reduced due to scatter, which can lead to spectral crosstalk between different energy windows.

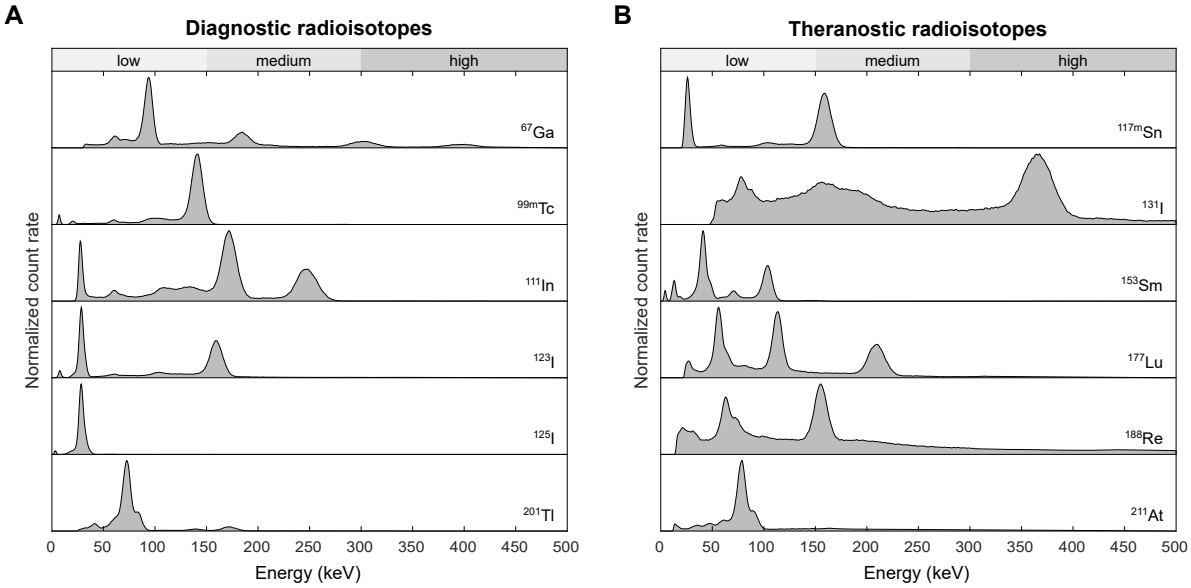

Figure 3.6. Emission spectra of diagnostic (A) and theranostic (B) radioisotopes used in nuclear medicine. Multi-isotope imaging is feasible for radioisotopes with individual photopeaks that do not interfere (A). Theranostic radioisotopes additionally emit charged particles and thus Bremsstrahlung, which may affect the photopeak (B). The spectra were acquired using point sources and a NaI detector, therefore Bremsstrahlung and Compton scattering shows decreased. (adapted from Lukas et al. [19])

The ideal nuclides for multi-isotope imaging, however, would be gamma emitters with low probability for other modes of decay. Since the radioisotopes are to be introduced into biological systems and are often ligated to molecular probes, chemical and physiological properties need to be considered as well. Electronegativity, solubility, toxicity and other aspects are essential for safe and functional tracer use. Due to its favorable properties and high availability, ^{99m}Tc is used for about 85 % of nuclear medicine applications [20]. Other isotopes for diagnostic imaging include ^{67}Ga, ^{123}I, ^{125}I, ^{111}In and ^{201}Tl (Figure 3.6 A). For theranostics applications, ^{117m}Sn, ^{131}I, ^{153}Sm, ^{177}Lu, ^{188}Re and ^{211}At are increasingly used (Figure 3.6 B). Basically, all these isotopes could be sampled simultaneously as long as their energy spectra show at least one individual photopeak.

However, energy spectra are distorted by several physical processes during photon transport and detection. Attenuation and scatter, the main sources of error in nuclear imaging, can limit

the accuracy of photopeak discrimination. Especially for multi-isotope applications, spectral crosstalk due to scatter may contribute a significant portion of error. Avoidance strategies and correctives can be deduced from physical theory or by Monte Carlo simulations, which allow multi-isotope imaging with still acceptable accuracy.

3.3.3 Photon Attenuation

Photons are attenuated by different physical processes that depend on isotope- and material-specific properties. If a photon beam of energy E_ν with an incident flux Φ_0 penetrates a material layer of thickness d, it is exponentially attenuated by partial or total energy transfer. The emerging flux Φ can be calculated according to Lambert-Beer's law

$$\Phi(E_\nu) = \Phi_0 \, e^{-\mu(E_\nu)d} \tag{3.1}$$

where μ is the linear attenuation coefficient that defines the probability for a photon to interact within a certain distance in matter. The linear attenuation coefficient μ depends on energy E_ν and is related to the sum of probabilities for different photon-matter interaction modes (Figure 3.7).

$$\mu(E_\nu) = \rho \, \frac{N_A}{M} \left(\sigma_p(E_\nu) + \sigma_c(E_\nu) + \sigma_r(E_\nu)\right) \tag{3.2}$$

In the energy range of SPECT, typically 20 to 400 keV, attenuation is mainly caused by photoelectric absorption σ_p and Compton scattering σ_c (incoherent, inelastic). At low energies, Rayleigh scattering σ_r (coherent, elastic) can also make a small contribution. Pair production and photodisintegration can be neglected, since they occur only at higher energies. The volumetric mass density ρ and the atomic density, given by the quotient of Avogadro's Number N_A and molar mass M, are used to scale the probability per atom (cross section) to a material-specific factor that can be practically used for attenuation correction. The linear mass attenuation coefficients for composite materials μ/ρ can be obtained by weighted additivity

$$\mu/\rho = \sum_i w_i \, (\mu/\rho)_i \tag{3.3}$$

where w_i is the fraction by weight of the i-th atomic constituent. The probability for one or the other physical process, therefore, depends on the material that is traversed. Body tissue, for example, contains 18 % to 86 % water with a moderate electron ($0.6 - 5.6 \times 10^{23}$ electrons/cm^3) and mass density (0.3 - 1.9 g/cm^3)[21], so Compton scattering is the leading process down to 30 keV (Figure 3.8 A). For high-density scintillators such as NaI (3.7 g/cm^3), photoelectric absorption predominates for energies up to 250 keV (Figure 3.8 B). The detection efficiency for each individual isotope, therefore, is a compromise between soft tissue penetration and absorption in high-dense detector materials (Figure 3.9).

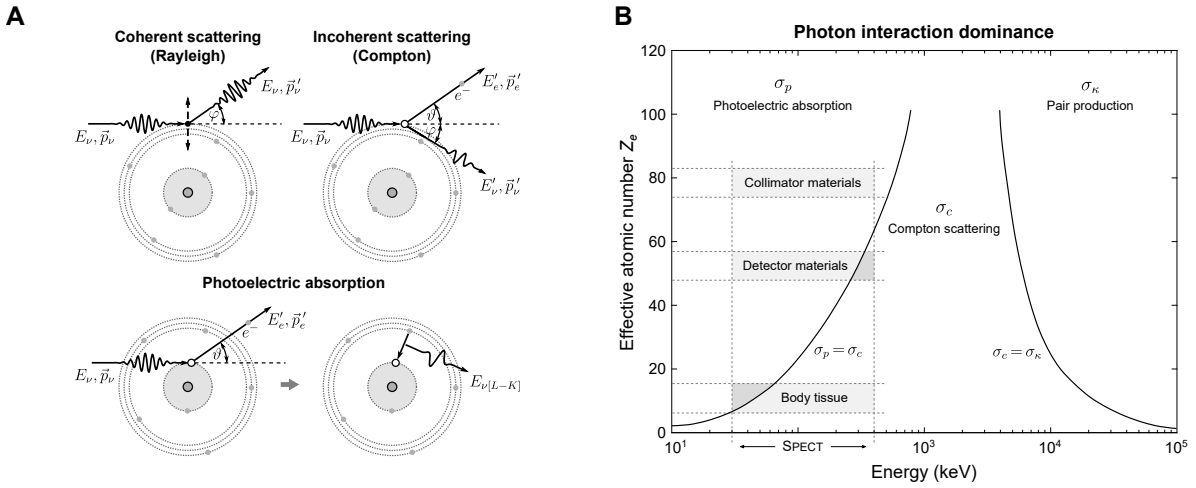

Figure 3.7. Schematic representation of photon-matter interaction modes (A) and their dominance (B) in the energy range of SPECT. In body tissue, Compton scattering is the predominant process and leads to spectral and spatial data blur. Materials with high atomic numbers are dominated by photoelectric absorption, which is favorable for detectors, collimators and shieldings. (data from NIST database [22])

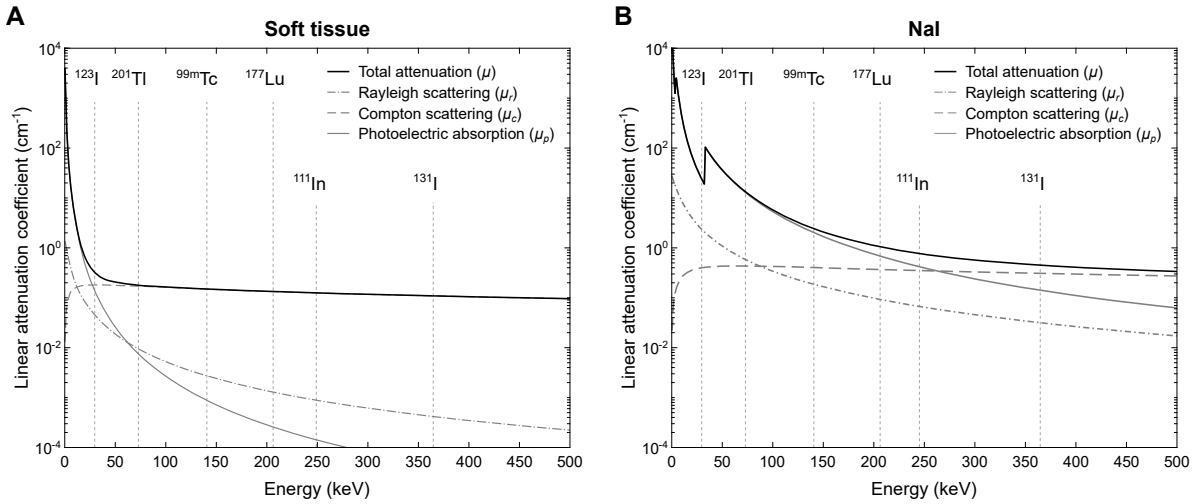

Figure 3.8. Linear mass attenuation coefficients for soft tissue (A) and the scintillator material NaI (B). The probabilities for different interaction modes depend on the radioisotope and on the material being traversed. In the energy range of SPECT, Compton scattering and photoelectric absorption predominate. (data from NIST database [23])

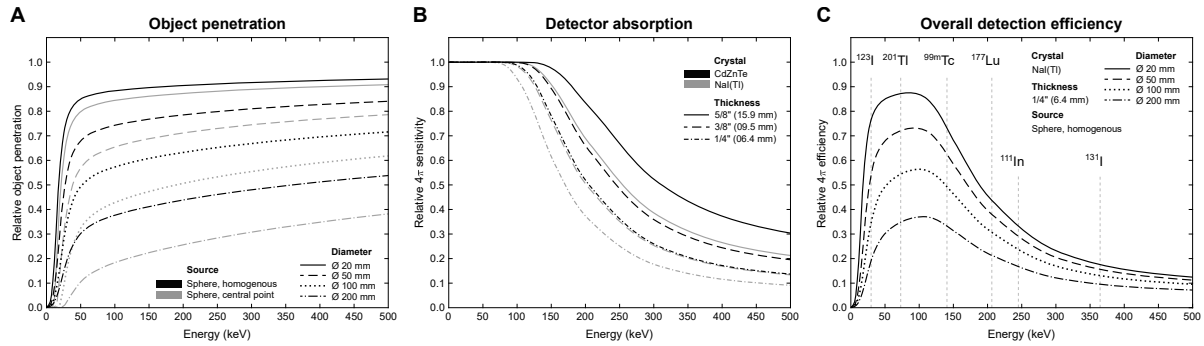

Figure 3.9. Exemplary Monte Carlo simulation of object penetration (A), detector absorption (B), and total detection efficiency (C) as a function of energy. With increasing energy, the self-attenuation of an imaging object (A), but also the detector absorption (B) is reduced. The resulting detection efficiency therefore differs for each individual isotope (C).

Photoelectric Absorption

In photoelectric absorption, the entire energy of an incident photon E_ν is transferred to an electron of the inner atomic shell with binding energy E_B (Figure 3.7 A). The electron is released with kinetic energy $E'_\nu = E_\nu - E_B$ and continues interacting with the converter material. Photoelectric absorption can therefore only take place if the incident photon energy is higher than the binding energy of the electron. The residual electron hole may recombine by relaxation of a higher-state electron, whereby characteristic x-ray, Auger electrons or atomic lattice vibrations may occur. The probability for photoelectric absorption σ_p sharply decreases with the photon energy E_ν, but also depends on the effective atomic number Z_e of the traversed material.

$$\sigma_p \propto \frac{{Z_e}^{3.5}}{{E_\nu}^3} \tag{3.4}$$

Photoelectric absorption is the predominant process in high-density materials as those used for scintillators, collimators and shieldings (Figure 3.7 B). It is the physical process that forms the spectral photopeak.

Compton Scattering

Compton scattering is the quantum theory of elastic, relativistic collision of photons with a free or loosely bound charged particle, usually an electron of the outer atomic shell (Figure 3.7 A). An incident photon deposits a portion of its energy E_ν to a recoil electron and is deflected with a lower energy E'_ν. The shell electron is released with kinetic energy E'_e and continues interacting with the material. The process can be described by the Compton scatter equations.

$$E'_\nu(\varphi) = \frac{E_\nu}{1 + \dfrac{E_\nu}{m_e c^2}(1 - \cos\varphi)} \tag{3.5}$$

$$E'_e(\varphi) = E_\nu - E'_\nu(\varphi) \tag{3.6}$$

The energies for the scattered photon $E'_\nu(\varphi)$ and electron $E'_e(\varphi)$ depend on the scattering angle φ, the incident photon energy E_ν and the electron rest energy $m_e c^2$. Compton scattering within the detector material creates electrons with kinetic energy E'_e that directly contribute to the detector signal along with photoelectric absorption. Photons scattered in body tissue, by contrast, will have a reduced energy E'_ν and a changed direction resulting in spatial and spectral misinterpretation (Figure 3.10 A).

The probability for Compton scattering σ_c does not depend on materials' effective atomic number Z_e and only slightly on energy E_ν.

$$\sigma_c \propto \frac{{Z_e}^0}{{E_\nu}^1} \neq f(Z_e) \tag{3.7}$$

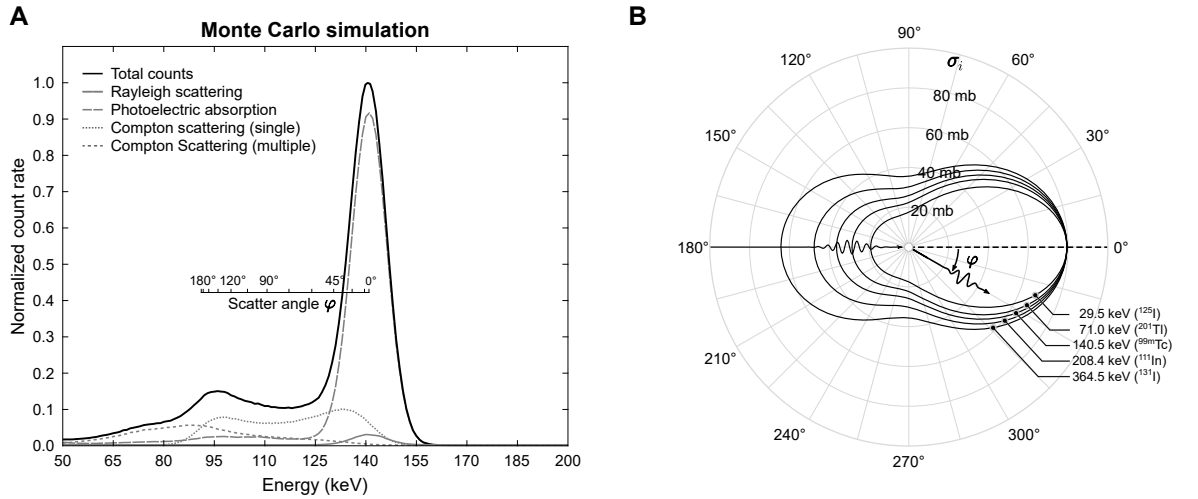

Figure 3.10. Energy spectrum (A) and angular distribution (B) of Compton scattering. The detector signal is shaped by different spectral components, of which the photopeak and Compton scatter contributes the majority. Compton scattering results in a downshift of energy and therefore spectral misinterpretation (A). The scattering angle φ of a Compton photon depends on the incident photon energy, with the forward and backward directions being preferred (B). (Monte Carlo simulation, $E_\nu = 140.5\,\mathrm{keV}$, water sphere with $\varnothing 10\,\mathrm{mm}$, NaI detector (A); Klein-Nishina-Plot [24] (B))

The probability for a photon to be scattered in a certain solid angle $d\sigma_c/d\Omega$ also changes with the photon energy E_ν (Figure 3.10 B). The differential cross sections can be derived from quantum electrodynamic for unpolarized photons using the Klein-Nishina equation [24]

$$\frac{d\sigma_c}{d\Omega} = \frac{r_0^2}{2}\left(\frac{E'_\nu}{E_\nu}\right)^2\left(\frac{E'_\nu}{E_\nu} + \frac{E_\nu}{E'_\nu} - \sin^2\varphi\right) \tag{3.8}$$

where r_0 is the classical electron radius with $r_0 = e^2/(4\pi\,\epsilon_0\,mc^2) = 2.815\times10^{-15}\,\mathrm{m}$. At low energies, forward and backward scattering are equally likely, but as energy increases, the portion of forward scattering rises. The lateral scattering component is less pronounced at all energies.

Compton scattering is the most prominent process in low-density materials such as body tissue and water (Figure 3.7 B). It is the physical process that affects the photopeak most.

Rayleigh Scattering

In Rayleigh scattering, the incident photon does not have enough energy to liberate a shell electron from its bound state (Figure 3.7 A). The electron remains in its shell and is forced together with other electrons to a collective oscillation. The oscillating electrons act like a transmitter and completely re-radiate the energy that was absorbed. The incident and radiated photon therefore have the same energy but may differ in direction. The scattered photons are emitted in a fixed phase relation to the incident photon preferentially in forward and backward direction. The probability for Rayleigh scattering σ_r decreases with the photon energy E_ν and increases with the effective atomic number Z_e of the traversed material.

$$\sigma_r \propto \frac{{Z_e}^{1.5}}{{E_\nu}^2} \tag{3.9}$$

For low atomic numbers, such as those in body tissue, Rayleigh scattering is relevant only for energies below 40 keV (Figure 3.8 A). It contributes only a minor fraction to the photopeak, but may compromise the accuracy of its spatial correlation.

3.3.4 Spectral Separation

Different physical processes in the course of photon transport and detection can blur the experimental energy spectra. Imperfect crystal structures of the detector material and limited electronic sampling, for example, deteriorate the intrinsic energy resolution of the detector system (Figure 3.4 B) and thus limit the accuracy of isotope separation (Figure 3.11).

The energy spectrum $\dot{N}(E)$ of a radiation field with monochromatic energy E_ν can only be detected with a statistical uncertainty, which can be described by a Gaussian distribution

$$\dot{N}(E) = \dot{N}_{max}\, e^{-4\ln(2)\frac{(E-E_\nu)^2}{\Delta {E_\nu}^2}} \tag{3.10}$$

where $\dot{N}_{max}$ means the maximal count rate and ΔE_ν the full width at half maximum of detector's energy resolution. For two closely spaced photopeaks with energy E_1 and E_2 that can be resolved with the energy resolutions ΔE_1 and ΔE_2, the intersection $c_{1|2}$ can be calculated.

$$c_{1|2} = \frac{\Delta {E_2}^2 E_1 - \Delta {E_1}^2 E_2 + \Delta E_1 \Delta E_2 \sqrt{(E_1 - E_2)^2 + \frac{1}{4\ln(2)}\left(\Delta {E_2}^2 - \Delta {E_1}^2\right) \ln\left(\frac{\dot{N}_{max,1}\,\Delta E_2}{\dot{N}_{max,2}\,\Delta E_1}\right)}}{\Delta {E_2}^2 - \Delta {E_1}^2} \tag{3.11}$$

The intersection $c_{1|2}$ can be used to define the optimal energy windows for photopeak separation. The spectral crosstalk between two different photopeaks depends on the ratio of their signal intensities. Therefore, it may change due to different tracer uptake or different half-lives over time (Figure 3.12). If the maximal count rates $\dot{N}_{max,1}$ and $\dot{N}_{max,2}$ or the energy resolutions ΔE_1 and ΔE_2 are unknown, the energy window width ΔE_w can be approximated assuming similar photopeak shapes.

$$\Delta E_w = \frac{E_2 - E_1}{E_2 + E_1} \cdot 100\% \tag{3.12}$$

The photopeak usually represents the unscattered photons that have fully been absorbed and is the spectral component most qualified for imaging use. Its intensity, however, is reduced by attenuation or Compton scattering, which causes a downward energy shift (Figure 3.11). Compton photons will cover the energy range from $E'_\nu(0) = E_\nu$ (zero scatter) to $E'_\nu(\pi)$ (180° backscatter), so the energy window for the photopeak has to be narrowed to discriminate (Figure 3.10). Since each additional gamma line increases the spectral complexity, optimization of experimental setups and development of corrective procedures are necessary to preserve image quality, especially for multi-isotope applications.

The present work, therefore, aimed to implement different procedures for accurate separation of multiple photopeaks. Several representative radioisotopes with decay properties covering a wide range of spectral interference were used to evaluate and advance multi-energy SPECT for multi-isotope applications.

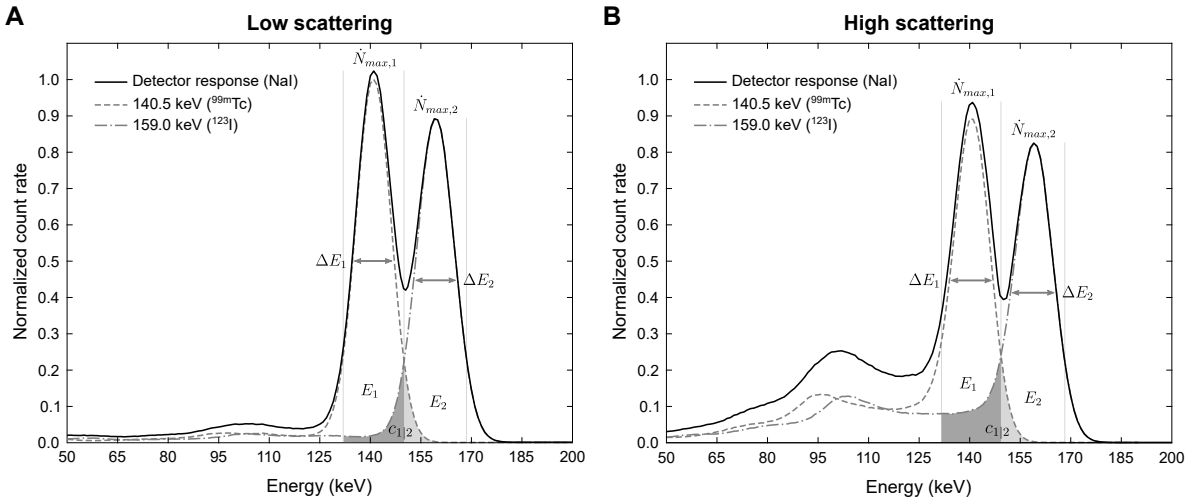

Figure 3.11. Separability of multiple photopeaks under low (A) and high (B) scattering conditions. Two closely spaced photopeaks cannot be separated entirely due to the limited energy resolution of the detector system (A). Spectral crosstalk (gray shading) increases with scattering, especially for the lower energy photopeak (B). E refers to photon energy, ΔE to energy resolution, N_{max} to maximal photopeak count rate, and $c_{1|2}$ to photopeak intersection.

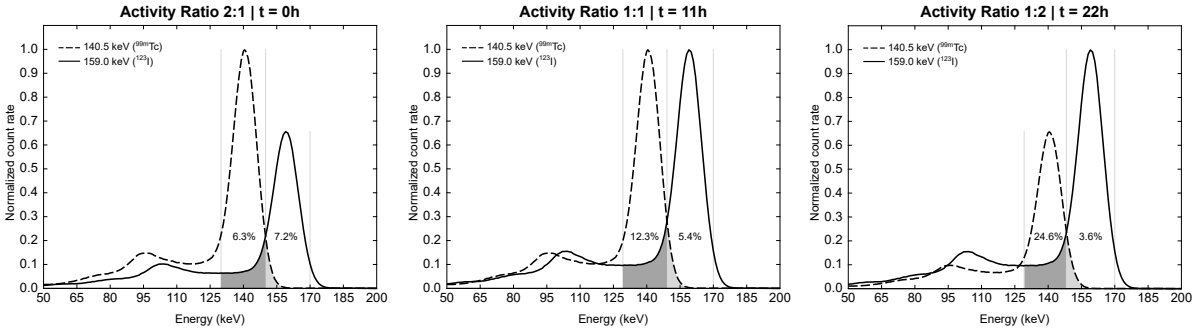

Figure 3.12. Spectral crosstalk fractions for different photopeak-intensity ratios. The mutual crosstalk for a given radioisotope combination depends on the ratio of signal intensities. It may change due to different tracer uptake or different half-lives over time.

3.4 Multi-Pinhole SPECT

In SPECT, mechanical collimators are used to restrict the photon acceptance angle of a detector system. They are made of high-density materials, usually lead or tungsten, to absorb photons of undesirable origin. Only photons with trajectories in line with the collimator holes can be detected. Thus, geometry, size and orientation of the detectors' field of view can be defined (Figure 3.3).

In clinical SPECT, collimators with parallel or focusing hole arrays are widely used (Figure 3.3). Their spatial resolution is in the centimeter to millimeter range and physically limited by the intrinsic resolution of the detector system. In preclinical imaging, however, the organs of interest may be submillimeter in size and therefore cannot be directly resolved. Pinhole collimators are able to overcome the physical limitation by magnification of the imaging scene. A pinhole aperture, adequately placed between the source and the detector, creates a magnified inverted projection of the source distribution onto the detector plane (Figure 3.13 A). The magnification M of a pinhole can be derived from intercept theorem

$$M = \frac{S_d}{S_s} = \frac{h_d}{h_s} \tag{3.13}$$

where S_s means the size of the source, S_d the size of the detected image, h_s the source-to-focus

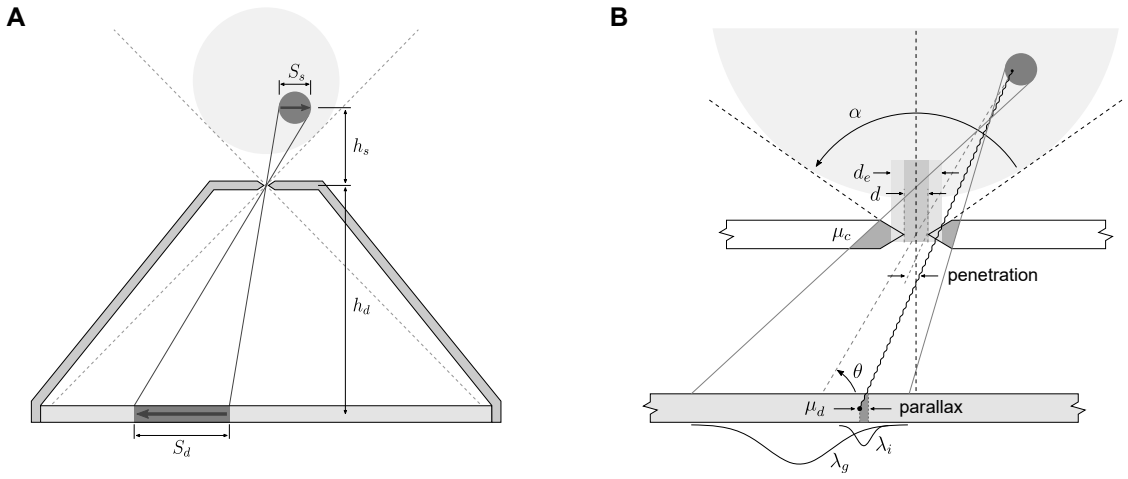

Figure 3.13. Geometric representation of the magnification (A) and angular relationships (B) for a knife-edge pinhole collimator. Pinhole collimators are used to magnify imaging objects to overcome the intrinsic resolution of a detector system (A). Septal penetration may cause the pinhole to appear wider and parallax may cause the photon to be detected displaced (B). With larger pinhole acceptance angles, both errors increase.

distance, and h_d the detector-to-focus distance. The spatial resolution of the imaging system λ_s can then be described as a function of this magnification M according to

$$\lambda_s = \sqrt{\frac{\lambda_i^2}{M^2} + {\lambda_g}^2} \quad | \; {\lambda_g}^2 = d^2 \left(1 + \frac{1}{M^2}\right) \tag{3.14}$$

where λ_i is the intrinsic detector resolution and λ_g is the geometric collimator resolution that depends on pinhole diameter d (Figure 3.13 B)[25]. When the detector-to-focus distance is larger than the source-to-focus distance ($h_d > h_s$), the spatial resolution of the imaging system λ_s can exceed the intrinsic resolution of the detector system λ_i. By variation of pinhole size and magnification, the system resolution can be adjusted to any specific application, which is used in small animal imaging to achieve the required submillimeter resolution.

However, also the collection efficiency ε of a pinhole collimator depends on pinhole size and magnification. It changes with the incidence photon angle θ and follows a steep $1/r^2$ fall-off with the source-to-collimator distance h_s [26].

$$\varepsilon = \sin^3 \theta \left(\frac{d}{4\, h_s}\right)^2 \tag{3.15}$$

For ideal pinholes, photons are entirely absorbed if the pinhole is missed or the incident angle θ is too small for a given acceptance angle α (Figure 3.13 B). Real pinholes, however, are usually formed as knife-edges where photons can partly penetrate the collimator material even if they miss the hole. This results in more photons passing the collimator than in the ideal case, so that the pinhole appears larger than its actual geometrical dimension is. For consideration, the ideal pinhole diameter d can be replaced by an effective pinhole diameter d_e given by Paix [18].

$$d_e = \sqrt{d\left(d + \frac{2}{\mu_c} \tan\frac{\alpha}{2}\right) + \frac{2}{{\mu_c}^2} \tan^2\frac{\alpha}{2}} \tag{3.16}$$

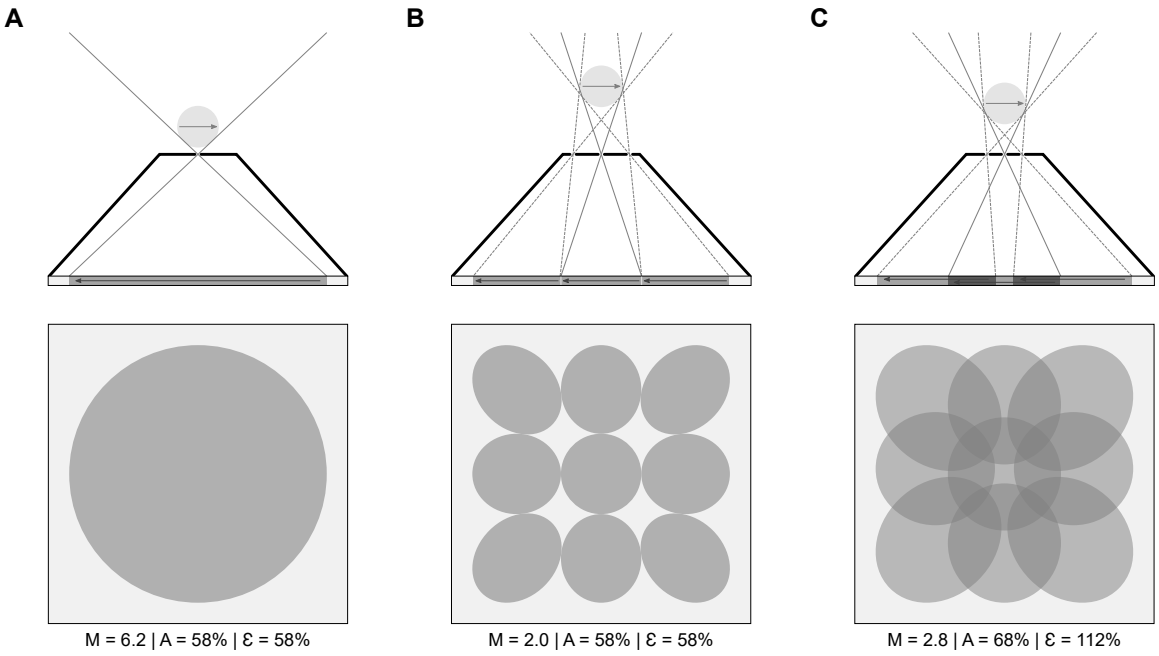

Figure 3.14. Collimation geometry and detector utilization for single-pinhole (A), non-multiplexed multi-pinhole (B), and multiplexed multi-pinhole (C) acquisitions. Multiplexed multi-pinhole collimators provide high utilization of the detector surface but spatial ambiguities may degrade image quality and quantification. For image reconstruction of multiplexed acquisition schemes, iterative algorithms are mandatory. M refers to magnification factor, A to utilized detector surface, and ε to collimator collection efficiency.

The effective pinhole diameter d_e depends on pinhole acceptance angle α and the attenuation coefficient of the collimator material μ_c. In consequence, photon penetration increases sensitivity, but deteriorates scatter errors and spatial resolution. It also reinforces parallax errors, which are a major source of spatial degradation, especially for pinhole-collimated acquisitions [27]. Photons are allowed to intercept the detector at oblique angles and may be recorded displaced, which is different from parallel-hole collimator design (Figure 3.13 B).

The allowance for oblique angles may also cause large sensitivity variation over the entire field of view, which can be acute particularly in preclinical imaging. To achieve a sufficient level of statistical accuracy, the total number of counts recorded for each voxel must be similar to those recorded in clinical SPECT. The voxel volumes are several orders of magnitude smaller, which requires the tracer concentration, scan duration, collimator efficiency, or a combination thereof to be increased accordingly to compensate.

Multi-pinhole collimators can be used to increase the efficiency of photon collection (Figure 3.14). The position, size, angulation and acceptance angle of each pinhole can be freely designed. An overlap of multiple pinhole projections on the detector surface can be avoided (non-multiplexing) (Figure 3.14 B) or allowed (multiplexing) (Figure 3.14 C). However, multiplexing provides more efficient coverage of the detector surface and improved sampling resolutions, but spatial ambiguities due to overlapping regions may degrade image quality and quantification. The number of pinholes and the degree of multiplexing need be optimized for specific applications so that efficiency gains outweigh the image degradation [28].

Multi-pinhole collimators also enable stationary data sampling to increase the temporal resolution of SPECT acquisitions [9]. The detector in conventional SPECT needs to rotate around the imaging object to sample different projective views for a three-dimensional reconstruction. Multi-pinhole collimators, by contrast, can be designed to provide multiple projective views without any detector motion (Figure 3.15 A). Different pinhole foci and angulations allow more uniform sensitivity profiles for the entire field of view and can provide complete datasets for three-dimensional image

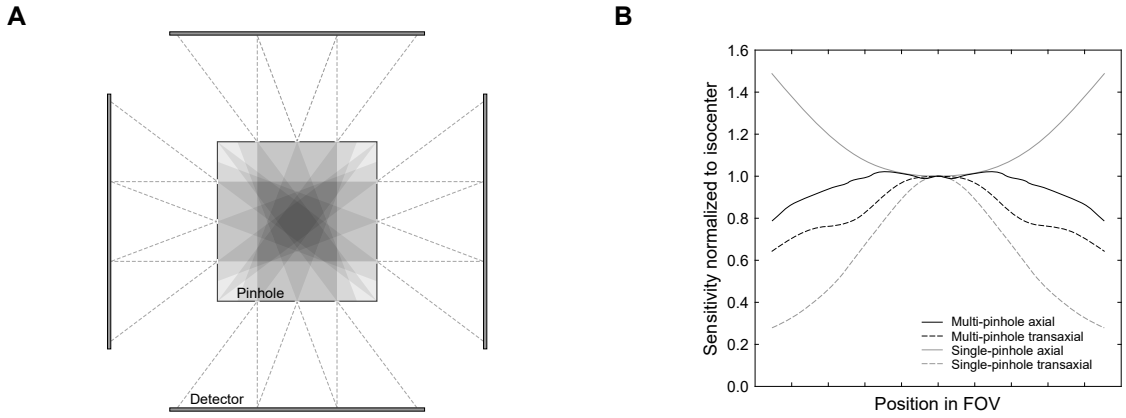

Figure 3.15. Field of view (A) and sensitivity profiles (B) of stationary multi-pinhole SPECT acquisitions. Multi-pinhole SPECT can provide sufficient angular coverage for three-dimensional image reconstruction without detector rotation (A). Different foci and angulations of multiple pinholes result in more uniform sensitivity profiles in axial and transaxial direction than single-pinhole colimation (B).

reconstruction (Figure 3.15 B). Therefore, it can be used to image biological processes without loss of information that may occur due to dead-time effects.

In this work, different single- and multiplexed multi-pinhole collimators were used, varying in sensitivity and magnification. Determination of their imaging properties for a wide range of multi-isotope applications was a major objective of the present work.

3.5 Image Reconstruction

Image reconstruction in emission tomography is a computational approach to obtain the three-dimensional distribution of a radiotracer from its angular projections. The raw data must be a set of projections $p(r, \phi)$ acquired at discrete angles ϕ and sampled at discrete intervals along the radial direction r (Figure 3.16 A), generically known as sinogram (Figure 3.16 B)[17].

For an ideal parallel-hole collimator, the radiation can only be measured along straight lines orthogonal to the detector surface with angle ϕ. Each measured projection $p(r, \phi)$, therefore, represents a series of line integrals along L, given by the Radon transform $\mathcal{R}$ of the true activity distribution $f(x, y)$.

$$p(r, \phi) = \mathcal{R}[f(x, y)] = \int_L f(x, y)\, d\tau \tag{3.17}$$

When a sufficient number of line integrals is measured, an estimate $f'(x, y)$ of the true activity distribution can be recovered by back-projection $\mathcal{B}$, which is a first approximation of the inverse Radon transform $\mathcal{R}^{-1}$.

$$f'(x, y) = \mathcal{B}[p(r, \phi)] = \frac{1}{\pi} \int_0^{\pi} p(r, \phi)\, d\phi \tag{3.18}$$

According to the central slice theorem, the activity distribution $f'(x, y)$ can be reconstructed exactly if an infinite number of angles ϕ and line integrals along r are given. In practice, however, datasets are finite and images are reconstructed into two-dimensional matrices with discrete

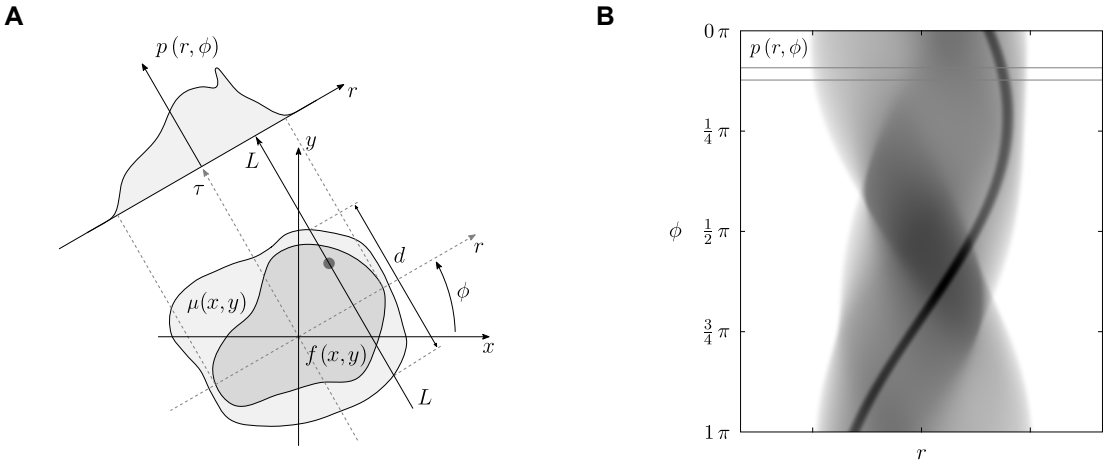

Figure 3.16. Geometric representation of the attenuated Radon transform (A) and the resulting sinogram (B). The Radon transform is an integral transform that is determined by a set of line integrals of function $f(x, y)$ along all straight lines L and is attenuated by the surrounding material $\mu(x, y)$ (A). The Radon transform is usually represented as sinogram, which can be used for image reconstruction (B).

pixilation (x_m, y_n). Mathematically, simple back-projection in discrete image space can be described by

$$f'(x_m, y_n) = \frac{1}{N} \sum_{i=1}^{N} p(r, \phi_i) \tag{3.19}$$

$$f'(x_m, y_n) = \frac{1}{N} \sum_{i=1}^{N} p(x_m \cos \phi_i + y_n \sin \phi_i, \phi_i) \tag{3.20}$$

where N is the number of projections and ϕ_i the angle of the i-th projection. The data from each element of the profile $p(r, \phi_i)$ is distributed back across the image grid (x_m, y_n) of size $[\, m \times n \,]$ [17]. The weighted sum of all back-projections will then give an image estimate $f'(x_m, y_n)$ of the true activity distribution (Figure 3.17, Figure 3.18).

However, with simple back-projection, the counts are projected also to the outside of the activity containing volume, resulting in image blurring artifacts (Figure 3.18 B). Filtering prior to back-projection (FBP) is commonly used to resolve those artifacts, which are known to decrease with radial distance r (Figure 3.18 C). The filters are designed to suppress low-frequency components and are usually applied in Fourier's frequency domain. A major disadvantage of FBP, however, is the amplification of high-frequency noise. Streaking artifacts may arise from poor counting statistics and ghosting due to incomplete emission data.

Iterative reconstruction algorithms can approach the true activity distribution more accurately by successive improvement of an initial image estimate (Figure 3.17). The initial image is forward-projected into sinogram space to be compared with the measured emission data. From this comparison, correction values can be back-projected into image space to improve the estimate accordingly. This process is repeated until the difference between the forward-projected estimate and the measured emission data is sufficiently small. Iterative reconstruction algorithms are computationally intensive, but are regarded to perform better than FBP, especially in low-counting regions where they significantly reduce the image noise (Figure 3.18 D).

A further advantage of iterative algorithms is the ability to take a-priori knowledge into account. Especially in small animal imaging with pinhole collimation, minor physical and geometrical effects gain importance. Consideration of parallax and septal penetration during reconstruction

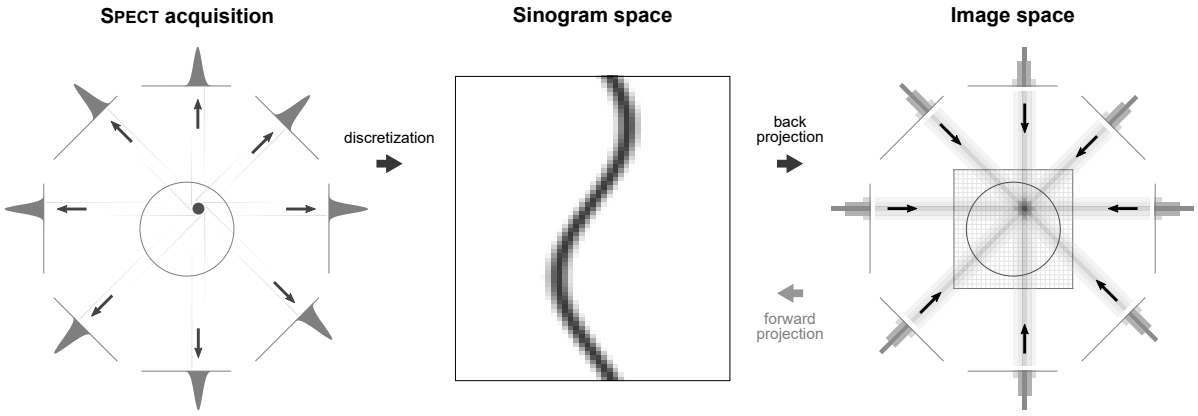

Figure 3.17. Schematic representation of simple back-projection of a point source. A set of projection profiles is acquired at discrete angles and discrete intervals along the radial direction. An approximation of the source distribution can be reconstructed by projecting the data from each element in a profile back across the entire image grid. In iterative reconstruction, forward-projection into sinogram space and backward-projection into image space are performed repeatedly, with a-priori information and quantitative corrections applied at each step.

can improve the image quality substantially. For multiplexed multi-pinhole acquisitions, iterative algorithms are mandatory to resolve the spatial ambiguities of overlapping detector regions.

For quantitative image reconstruction, however, further corrections need to be applied (Figure 3.19). Detector specific properties p_n, attenuation p_a and scatter p_s need to be considered and are typically implemented as a series of multiplicative factors in sinogram space.

$$p \propto p_n \cdot p_a \cdot p_s \cdot ... \tag{3.21}$$

The normalization factor p_n is used to compensate for inequalities in efficiency for each individual line integral of the projection profile p (Figure 3.19 A). This includes individual detector efficiencies, geometrical sensitivity variations, dead time, and energy dependencies. It is virtually invariant for each system and can be determined from a scan of a flood source centered in the field of view.

The correction for attenuation p_a, however, depends on the object that is imaged and needs to be calculated for each individual scan. The probability σ of a photon with energy E_ν to reach the detector depends on the linear attenuation coefficient μ and on the thickness d of the material that is penetrated within the field of view.

$$\sigma(E_\nu) = e^{-\mu(E_\nu)d} \tag{3.22}$$

Without correction, the activity concentration in the center of the attenuating object would appear lower than near its outer boundary (Figure 3.19 B). A simple attenuation estimate can be obtained by assuming a uniform distribution within the imaging object with constant attenuation coefficient μ. The simple back-projection can then be rewritten into its attenuated form to estimate the activity distribution $f'(x, y)$ and its discrete representation $f'(x_m, y_n)$ [29].

$$f'(x, y) = \frac{1}{2\pi} \int_0^{2\pi} p(r, \phi)\, e^{-\mu(E_\nu)d}\, d\phi \tag{3.23}$$

$$f'(x_m, y_n) = \frac{1}{N} \sum_{i=1}^{N} p(x_m \cos\phi_i + y_n \sin\phi_i, \phi_i)\, e^{-\mu(E_\nu)d} \tag{3.24}$$

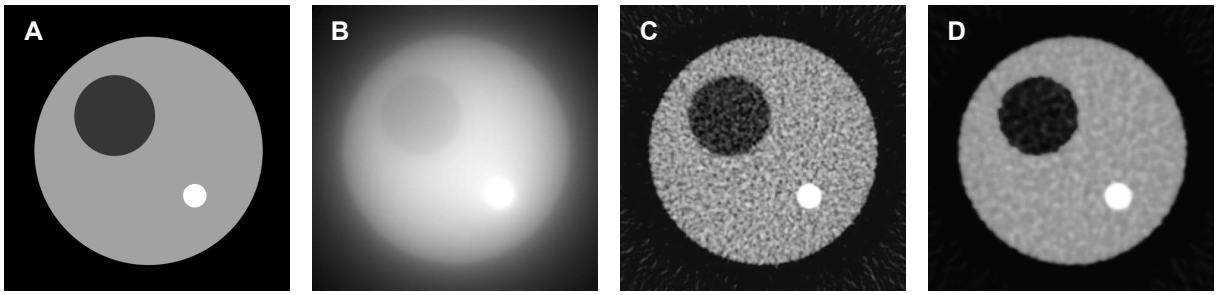

Figure 3.18. Image reconstructions of a digital phantom (A) using simple back-projection (B), filtered back-projection (C), and an iterative OSEM algorithm (D). Iterative reconstruction algorithms usually provide better image quality than filtered back-projection but are computationally more expensive. (adapted from Cherry et al. [17])

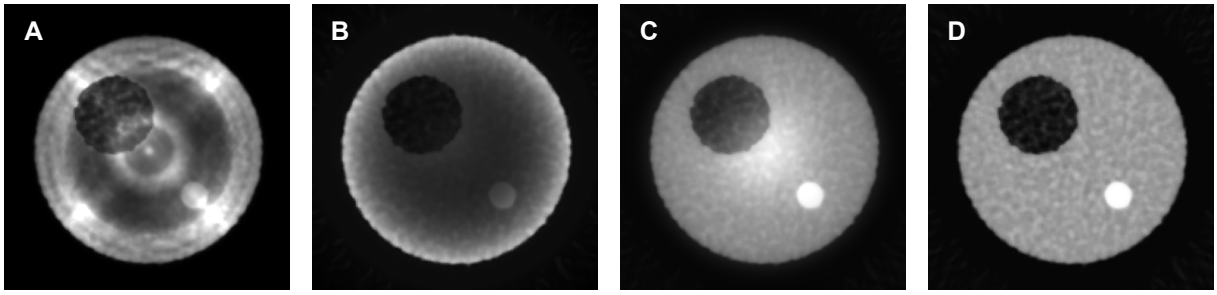

Figure 3.19. Image reconstructions of a digital phantom with no correction (A), normalization (B), attenuation correction (C), and scatter correction (D). For quantitative assessment of molecular processes, advanced image correction is essential. Correction of scatter can be challenging especially for multi-isotope applications (adapted from Cherry et al. [17])

For uniform objects with small thickness d, this method can be sufficiently accurate, but it always requires projection data over full 360 degree.

To improve the estimate for the attenuation coefficient distribution, mathematical models or direct measurements are commonly used. Transmission scans, for example, provide more differentiated three-dimensional data of the attenuating materials in the field of view. Monte Carlo simulations, on the other hand, are based on physical principles and can be directly integrated into the forward and backward projector of an iterative reconstruction algorithm. For non-uniform attenuation coefficients, the attenuation term for the discrete Radon transform $\mu(E_\nu)d$ then extends to

$$\mu(E_\nu)\, d = \sum_i \mu_i(E_\nu)\, \Delta d_i \tag{3.25}$$

where μ_i is the linear attenuation coefficient of the i-th pixel and Δd_i is the path length through it.

The scatter correction factor p_s is of lesser magnitude compared to the attenuation. However, Compton scattering, and at low energies also coherent scattering, can have a significant effect on image quality and quantification (Figure 3.19 C). The photon can no longer be assumed to be in a straight line with its origin and will be detected with lower energy. In practice, therefore, scatter correctives can be estimated by additional energy windows around the photopeak. The count rate in such scatter windows can be used to approximate the scattering fraction for each single element of the projection set p_s. Model-based scatter correction, however, offers much higher accuracy and is increasingly used. It takes the attenuation map obtained from a transmission scan and Monte Carlo simulations to calculate the percentage of photons being scattered. Especially for multi-isotope applications, such advanced scatter correction is mandatory, since spectral crosstalk caused by scatter is a major error source [19].

In this work, an iterative three-dimensional ordered subset expectation maximization algorithm (3D-OSEM) has been used together with advanced Monte Carlo simulations. It allows accurate estimation of attenuation, scatter and spectral crosstalk to improve image quality and quantification of measured datasets. The development of a reconstruction framework dedicated for multi-isotope and multiplexed multi-pinhole applications was a major task of the present work.

3.6 Monte Carlo Simulation

Monte Carlo methods are a class of computational algorithms that rely on repeated random variable sampling. They are used in many cases of applied mathematics including finance, medicine, chemistry and physics to solve deterministic problems by drawing random samples from a probability distribution. An early variant of this method was devised to solve the Buffon's needle problem, in which the number π could be approximated using stochastics and integral geometry (Figure 3.20 A)[30]. With the development of electronic calculators, Monte Carlo techniques became interesting also for complex multidimensional integrals and partial differential equations in advanced nuclear physics. Mathematics and algorithmics have been developed largely by the Los Alamos National Laboratory and were named after a famous casino in Monte Carlo due to its gambling characteristics.

Based on these fundamentals, general-purpose Monte Carlo computer codes have been developed to simulate geometries, materials and physics of entire real world experiments. GEANT4 [31], GATE [32], MCNP [33], EGSNRC [34], FLUKA [35] and Penelope [36] might be examples, able to simulate radiation fields and particle transport for applied physical applications. They all compute the path of a single physical particle in individual steps from the moment it enters matter until it leaves or is absorbed. For each single interaction, the location, type, daughter particles, scattering angles, paths and energies are determined by random calculations, whose probability distributions result from known cross sections of quantum physics. Thus, the transport of mass, momentum and energy can be modeled to describe microscopic fluxes of these quantities. Repeated for a large number of particles, Monte Carlo simulations can also predict macroscopic properties, such as particles flux densities, energy spectra or dose distributions of real world

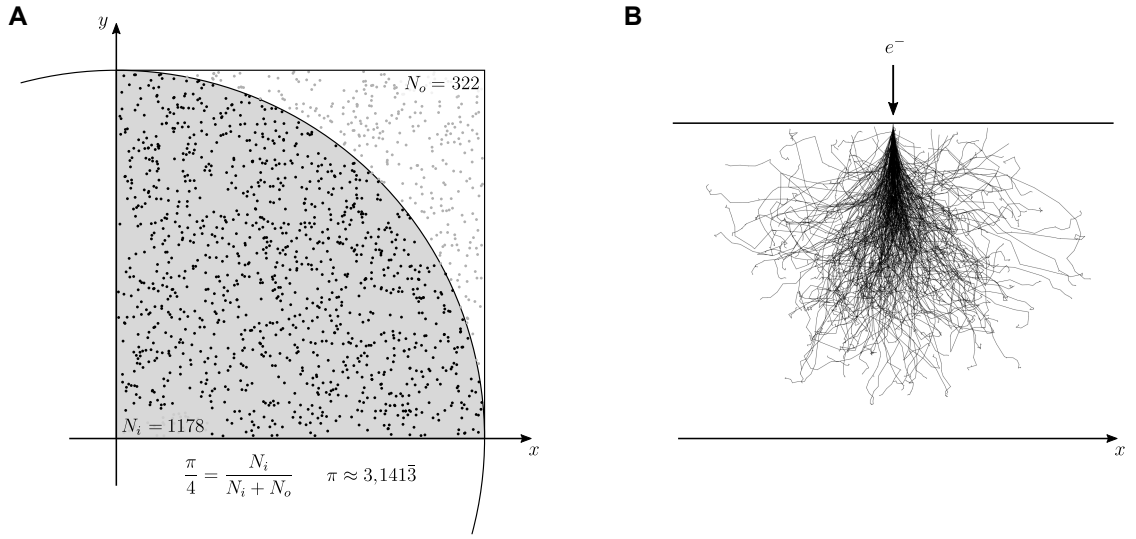

Figure 3.20. Exemplary Monte Carlo simulation in integral geometry (A) and radiation physics (B). Monte Carlo simulations are widely used for numerical integration. An example might be π, which can be estimated by random variable sampling of Cartesian coordinates and geometric relations between circular and square area integrals (A). The technique is particularly efficient in solving coupled integral differential equations in radiation physics. Transport of mass, momentum and energy of particle showers can be modeled to predict macroscopic quantities of radiation fields (B).

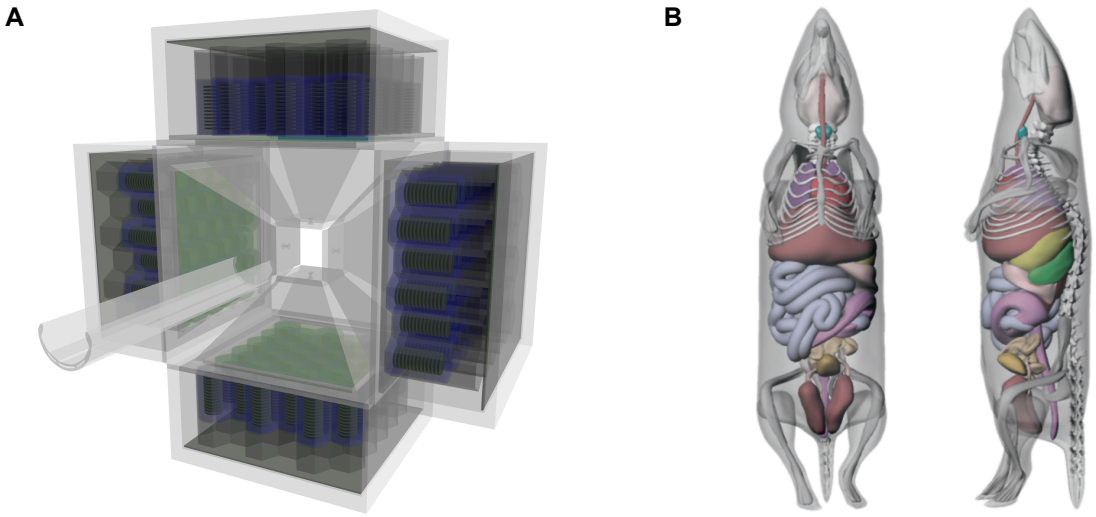

Figure 3.21. Exemplary geometric model of a SPECT gantry (A) and mouse phantom (B) for Monte Carlo simulations. GATE enables accurate modeling of entire imaging systems including geometry, materials and time-dependent processes such as detector rotation, object motion or activity distribution changes (A). GATE also allows inclusion of voxalized image files to simulate complex animal models and heterogeneous activity distributions (B). (adapted from Lukas et al. [37] and Segars et al. [38], visualized with Blender [39])

experiments (Figure 3.20 B). In medical physics, this is widely used to optimize imaging hardware and reconstruction algorithms in-silico to reduce the development costs.

In this work, a combination of GEANT4 (GEometry AND Tracking) [31] and GATE (GEANT4 Application for Tomographic Emission) [32] has been used and adapted for the specific needs of multi-isotope multi-pinhole SPECT simulation. GEANT4 is one of the most powerful all-purpose C++ code compilations for radiation transport calculations. It covers a wide range of physical processes including electromagnetic, hadronic and optical interactions within a broad energy range of 250 eV to 1 PeV. A large set of subatomic particles, elements and materials is supported along with a simplified geometric description framework. The physics modeling capabilities have been validated against authoritative reference data and experimental results [40].

GATE, a C++ code extension for GEANT4, adds dedicated features for medical imaging applications. It encapsulates the GEANT4 libraries to provide a modular, versatile and scriptable simulation toolkit for nuclear emission tomography. The core layer attached to the GEANT4 kernel comprises basic classes for management of time, geometry, radiation source and read-out of the simulation. The application layer is scriptable and provides functions to facilitate advanced modeling tasks. Specific volume shapes, materials and spatial operations can be easily defined. Basic volume shapes can be replicated along regular patterns and irregular shaped volumes with inhomogeneous material compositions can be defined using voxelized imaging files (Figure 3.21). GATE also allows the handling of time-dependent phenomena such as detector rotation, object motion or activity distribution changes during simulation.

Besides geometry and physics, the entire process of radiation detection and signal formation can be modeled with GATE. Imperfect materials and electronic limitations are unique for each detector system and need to be considered for realistic simulation results. GATE provides advanced modulation capabilities for signal-processing related phenomena such as spatial, spectral and temporal blurring, energy discrimination, dead time, pileup, electronic noise and transfer rate limitations (Figure 3.22). They all are based on mathematical models and are usually sufficiently accurate for regular SPECT systems and for single-isotope applications.

For multi-isotope multi-pinhole applications, however, modeling efforts increase substantially. Multi-isotope simulations require high accuracy for a wider range of energies and the magnifying nature of pinholes does not excuse smallest geometric inaccuracies. The small object sizes

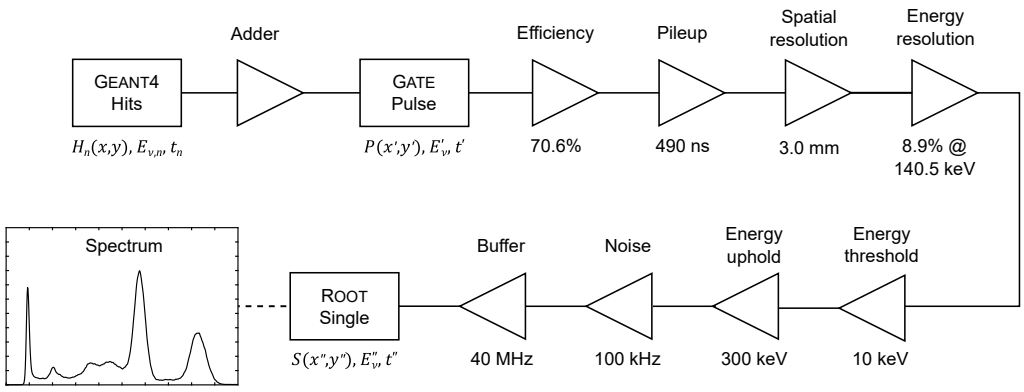

Figure 3.22. Exemplary signal processing model of a virtual SPECT experiment. The simulation of realistic detector response is challenging. GATE provides a variety of tools to imitate unideal signal formation of real radiation detectors that is mainly caused by imperfect scintillation materials and electronic limitations. (adapted from Lukas et al. [37])

in preclinical imaging also cause the scatter spectra to be dominated by hardware-related perturbations, making accurate modeling of the entire signal chain and all substructures of the detector back compartment of particularly importance [19].

Therefore, parametrization and advancement of the GATE signal modulators requires extensive measurement of system performance parameters and was one of the major challenges of the present work.

4 Materials and Methods

This section is a brief summary of the materials and methods originally published in the Journal of Nuclear Medicine [19] and in Ieee Transaction on Medical Imaging [37]. For a detailed description of the methodology, please refer to the Original Publications.

4.1 NanoSpect/ct

In this research, measurements and simulations were performed for the NanoSpect/ct^{plus} (Mediso, Hungary), a high-resolution, high-sensitivity Spect/ct system dedicated for small animal imaging. The system consists of four Anger-camera detectors and an x-ray cone-beam CT for functional and anatomical imaging. It is equipped with a heatable bed and a physiological monitoring system for small animal long-term anesthesia (Figure 4.1).

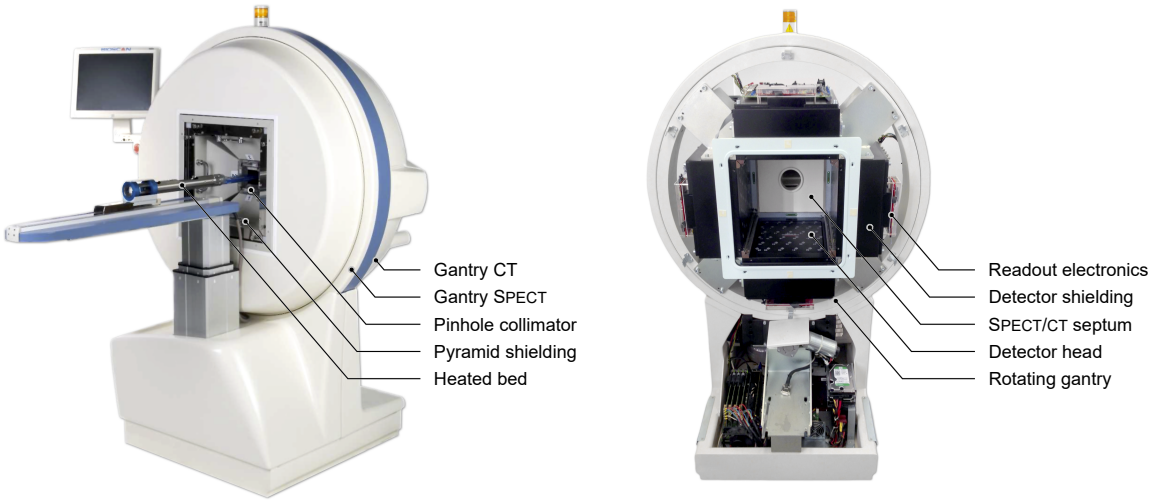

Figure 4.1. The NanoSpect/ct^{plus} system.

Photon collimation was achieved by patented single- and multi-pinhole apertures mounted to leaden pyramid shieldings. Two multiplexed multi-pinhole collimators for mouse (NSP 106, NSP 116), two multiplexed multi-pinhole collimators for rat (NSP 105, NSP 125) and one single-pinhole collimator for general purpose (NSP 115) were investigated (Figure 4.2).

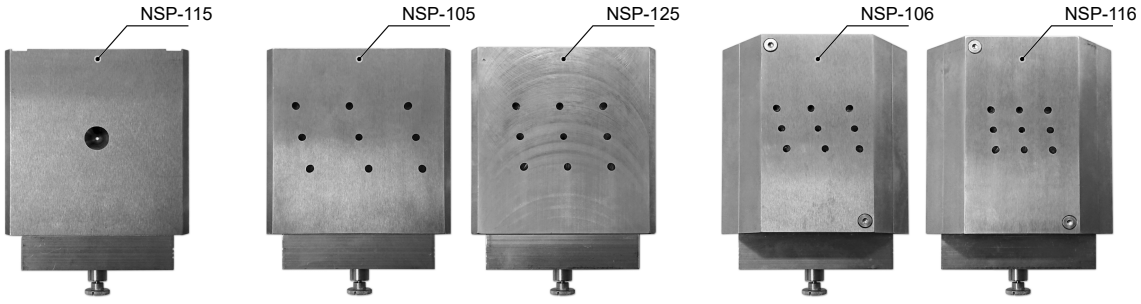

Figure 4.2. Pinhole collimators of the NanoSpect/ct^{plus} system.

4.2 Experimental Measurements

In the first study, the performance of the NanoSPECT/CT^{plus} system was evaluated with emphasis on simultaneous multi-isotope sampling. Due to the lack of standards for both multi-isotope and multi-pinhole SPECT imaging, experimental and mathematical procedures had to be developed.

For this purpose, theoretical consideration on multi-isotope imaging were translated to dedicated experiments using five representative radioisotopes (^{99m}Tc, ^{111}In, ^{123}I, ^{177}Lu, ^{201}Tl) (Figure 3.6). The isotopes were selected based on their specific decay properties to cover a wide range of spectral interference.

Using these isotopes, basic performance parameters of the SPECT system were determined and specific error sources were assessed. Image quality and quantification accuracy of multi-isotope image reconstructions were evaluated for adjacent and superimposed activity distributions.

Finally, spectral crosstalk errors were quantified for different pinhole collimators and generalized procedures for quantitative first-order corrections were proposed.

4.3 Monte Carlo Simulations

In the second study, a detailed Monte Carlo simulation model of the NanoSPECT/CT^{plus} system was developed with emphasis on high accuracy for multi-isotope applications. The system was modeled using the general-purpose Monte Carlo simulation framework GATE/GEANT4 [31, 32].

For this purpose, the geometric properties of the system components were modeled with particular precision. Material compositions were determined by x-ray fluorescence spectroscopy using a high-purity germanium detector. The signal processing of the readout electronics was modeled according to basic parameters determined in the first study. The Monte Carlo source code for energy resolution and background noise modeling was extended to incorporate non-simplified measured response functions. The entire model was validated by comparing complex single- and multi-isotope measurements with corresponding simulations.

Finally, the Monte Carlo model was used for quantitative high-order corrections of multi-isotope in-vivo data. A variety of applications was proposed to demonstrate the potential for cost-effective optimization of imaging hardware, acquisition protocols and quantitative reconstruction algorithms.

5 Results

This section is a brief summary of the results originally published in the Journal of Nuclear Medicine [19] and in Ieee Transaction on Medical Imaging [37]. For a detailed description of the results, please refer to the Original Publications.

5.1 Experimental Measurements

The NanoSPECT/CT^{plus} system revealed excellent performance in terms of count rate sensitivity, spatial resolution and energy resolution. Simultaneous multi-isotope sampling was feasible with up to three isotopes.

Due to the small object sizes in preclinical imaging, attenuation and scatter was reduced, while hardware-related perturbations turned out to be the predominant source of error. Spectral crosstalk between multiple radioisotopes was more likely mediated by hardware scatter than by source scatter. For particular isotopes, collimator penetration and x-ray fluorescence contributed a significant portion of error. Multiplexing of multiple pinholes introduced spectrospatial double ambiguities that could be avoided using collimators with larger field of view.

Depending on the multi-isotope combination, quantitative image correction by first-order calibration was sufficient only for mouse-sized objects. With increasing object size, secondary processes increasingly impaired image quality and quantitative accuracy, especially for superimposed activity distributions.

Therefore, advanced high-order corrections were required for radioisotopes with complex decay schemes and for objects larger than mice. For this purpose, quantitative Monte Carlo simulations would provide the most accurate correctives.

5.2 Monte Carlo Simulations

The NanoSPECT/CT^{plus} system could be modeled successfully in its entirety. The Monte Carlo simulations were able to predict energy spectra, planar images and tomographic reconstructions of real-world experiments with particularly high accuracy.

The model efficiently incorporated non-simplified response functions for energy resolution and background noise and therefore significantly improved the accuracy for an extended range of energy and noise levels. The simulation model was integrated into a software framework to provide consecutive workflows for parallelized simulation, proprietary raw data conversion and quantitative image reconstruction.

Finally, the simulation framework was used to optimize the imaging protocol of a specific dual-isotope triple-tracer in-vivo experiment. Procedures for optimization of collimator setup, energy windows, activity ratios and injection timing were proposed. After experimental measurements, the simulation framework was successfully used to compute four-dimensional attenuation, scatter and crosstalk maps for quantitative image correction of measured multi-isotope in-vivo data.

6 Discussion

In this work, multi-isotope multi-pinhole SPECT imaging in small laboratory animals has been investigated using a state-of-the-art SPECT/CT system and advanced Monte Carlo simulations. It was intended to provide a reliable and quantitative framework for multi-tracer studies in single subjects supporting the 3R animal welfare initiative at Charité – Universitätsmedizin Berlin for ethical, scientific and economic reasons.

In a first study, technical performance parameters of the SPECT/CT system have been evaluated with emphasis on multi-isotope applications. It has been shown that multi-isotope sampling was feasible with up to three isotopes but was frequently affected by physical limitations. Multi-isotope experiments need to deal with different half-lives, emission energies and count rate sensitivities during single measurements, so system calibrations can only be trade-offs and small interferences become important. In the present work, the resulting errors were systematically assessed and different procedures for objective characterization were proposed. Specific values for common radioisotopes have been tabulated and can be used for initial single- or multi-isotope study design. A small subset of these findings could be confirmed by publications in which single isotopes or specific applications have been investigated [9, 10, 13, 15, 41]. To our knowledge, it was the first comprehensive analysis on physical side effects and technical limitations in the field of preclinical multi-isotope SPECT imaging. Few procedures were adapted from publications NU 1 and NU 4 of the National Electrical Manufacturers Association, which were originally intended for clinical parallel-hole SPECT and preclinical PET imaging, respectively [42, 43].

The second study aimed to develop a Monte Carlo simulation model for multi-isotope protocol optimization and quantitative image reconstruction. Few investigations on multi-pinhole SPECT simulation have been published [44, 45, 46], but accurate modeling of the detector subcompartments and the entire signal chain has been given a low priority. For single-isotope experiments and standard conditions, simple models may provide sufficient results. For multiple isotopes, however, they fail in spectral accuracy [47]. In small animal imaging, spectral crosstalk is largely caused by hardware-related perturbations, which is why accurate modeling is of particular importance [15]. Therefore, in this work geometric properties, material compositions and signal processing chains were modeled with special care to achieve highest accuracy. Especially the energy resolution and spectrospatial noise distribution could be improved by introducing non-simplified measured response functions. This allows accurate simulation of ultra-low to ultra-high count rates and emission energies as frequently encountered in multi-isotope experiments. The model was validated by comparing numerous measurements with corresponding simulations and revealed high consistency. To our knowledge, it is the most complete in-silico replication of any multi-pinhole SPECT/CT system for multi-isotope applications.

However, a limitation of Monte Carlo simulations is the required computing time. Depending on the real time simulated, the amount of radioactivity and isotopes' decay scheme complexity, a full simulation may last several days to complete. A software framework for parallelized simulation, proprietary raw data conversion and quantitative image reconstruction was developed, but simulation time could only be reduced by the factor of available central processing units (CPU). Upcoming efforts, therefore, will deal with migrating simulations to the graphics processing unit (GPU) [48]. A second limitation could be the restricted number of radioisotopes with which the model has been validated. Simulations were performed on four representative diagnostic isotopes. Theranostic radioisotopes with relevant branching ratios for β- and α-decay are pending.

However, the results of this work will expand the capabilities of small animal research at Charité – Universitätsmedizin Berlin and facilitates several central and recurring tasks. Preparatory optimization procedures previously performed on laboratory animals will be replaced by Monte

Carlo simulations. Hardware configurations, energy windows and activity ratios will be studied in-silico and three-dimensional estimations of attenuation, scatter and crosstalk will improve quality and quantification of measured in-vivo data.

Finally, quantitative multi-isotope multi-pinhole SPECT imaging enables simultaneous characterization of different molecular pathways in a single experiment and has great potential for a variety of scientific applications. It will increase experimental throughput by parallelizing sequential studies and will add scientific value by enabling competing or comparative multi-tracer study designs.

7 Conclusion

In this work, quantitative multi-isotope multi-pinhole SPECT imaging in small laboratory animals has been established. Using a state-of-the-art SPECT/CT system and advanced Monte Carlo simulations, specific error sources have been identified and procedures for quantitative image correction have been developed.

The findings of this work will improve image quality and quantification of multi-isotope multi-pinhole SPECT in small laboratory animals. They may guide through the laborious process of multi-isotope protocol optimization and finally will support the 3R initiative at Charité Berlin that aims to replace, reduce and refine animal experimentation.

8 References

1. Franc BL, Acton PD, Mari C, and Hasegawa BH. Small-Animal SPECT and SPECT/CT: Important Tools for Preclinical Investigation. *J Nucl Med.* 2008 Oct; 49:1651–63.
2. Zanzonico P. Principles of nuclear medicine imaging: planar, SPECT, PET, multi-modality, and autoradiography systems. *Radiat Res.* 2012 Apr; 177:349–64.
3. Meikle SR, Kench P, Kassiou M, and Banati RB. Small animal SPECT and its place in the matrix of molecular imaging technologies. *Phys Med Biol.* 2005 Nov; 50:R45–61.
4. Martin EB, Williams A, Richey T, Stuckey AR, Heidel E, Kennel SJ, and Wall JS. Comparative evaluation of p5+14 with SAP and peptide p5 by dual-energy SPECT imaging of mice with AA amyloidosis. *Sci Rep.* 2016 Mar; 6:22695.
5. Dresel SH, Kung MP, Huang XF, Plössl K, Hou C, Meegalla SK, Patselas G, Mu M, Saffer JR, and Kung HF. Simultaneous SPECT studies of pre- and postsynaptic dopamine binding sites in baboons. *J Nucl Med.* 1999 Apr; 40:660–6.
6. Xu B, Shokeen M, Sudlow GP, Harpstrite SE, Liang K, Cheney PP, Edwards WB, Sharma V, Laforest R, Akers WJ, and Achilefu S. Utilizing the Multiradionuclide Resolving Power of SPECT and Dual Radiolabeled Single Molecules to Assess Treatment Response of Tumors. *Mol Imaging Biol.* 2015 Oct; 17:671–9.
7. Peterson TE and Shokouhi S. Advances in preclinical SPECT instrumentation. *J Nucl Med.* 2012 Jun; 53:841–4.
8. Islamian JP, Azazrm A, Mahmoudian B, and Gharapapagh E. Advances in pinhole and multi-pinhole collimators for single photon emission computed tomography imaging. *World J Nucl Med.* 2015 Feb; 14:3–9.
9. Lange C, Apostolova I, Lukas M, Huang KP, Hofheinz F, Gregor-Mamoudou B, Brenner W, and Buchert R. Performance evaluation of stationary and semi-stationary acquisition with a non-stationary small animal multi-pinhole SPECT system. *Mol Imaging Biol.* 2014 Jun; 16:311–6.
10. Finucane CM, Murray I, Sosabowski JK, Foster JM, and Mather SJ. Quantitative Accuracy of Low-Count SPECT Imaging in Phantom and In Vivo Mouse Studies. *Int J Mol Imaging.* 2011 Mar; 2011:197381.
11. Darambara DG and Todd-Pokropek A. Solid state detectors in nuclear medicine. *Q J Nucl Med.* 2002 Mar; 46:3–7.
12. Hutton BF, Buvat I, and Beekman FJ. Review and current status of SPECT scatter correction. *Phys Med Biol.* 2011 Jul; 56:R85–112.
13. Chen CL, Wang Y, Lee JJS, and Tsui BMW. Toward quantitative small animal pinhole SPECT: assessment of quantitation accuracy prior to image compensations. *Mol Imaging Biol.* 2009 May; 11:195–203.
14. Buvat I and Castiglioni I. Monte Carlo simulations in SPET and PET. *Q J Nucl Med.* 2002 Mar; 46:48–61.
15. Hwang AB, Franc BL, Gullberg GT, and Hasegawa BH. Assessment of the sources of error affecting the quantitative accuracy of SPECT imaging in small animals. *Phys Med Biol.* 2008 May; 53:2233–52.
16. Fan P, Hutton BF, Holstensson M, Ljungberg MP, Pretorius H, Prasad R, Ma T, Liu Y, Wang S, Thorn S, Stacy MR, Sinusas AJ, and Liu C. Scatter and crosstalk corrections for (99m)Tc/(123)I dual-radionuclide imaging using a CZT SPECT system with pinhole collimators. *Med Phys.* 2015 Dec; 42:6895–911.

17. Cherry SR, Sorenson JA, and Phelps ME. Physics in Nuclear Medicine. Fourth Edition. Philadelphia: W.B. Saunders, 2012.

18. Paix D. Pinhole imaging of gamma rays. *Phys Med Biol.* 1967 Oct; 12:489–500.

19. Lukas M, Kluge A, Beindorff N, and Brenner W. Multi-Isotope Capabilities of a Small-Animal Multi-Pinhole SPECT System. *J Nucl Med.* 2020 Jan; 61:152–61.

20. Boschi A, Martini P, Pasquali M, and Uccelli L. Recent achievements in Tc-99m radiopharmaceutical direct production by medical cyclotrons. *Drug Dev Ind Pharm.* 2017 Sep; 43:1402–12.

21. Shrimptont PC. Electron density values of various human tissues. *Phys Med Biol.* 1981 Sep; 26:907–11.

22. Berger MJ, Hubbell JH, Seltzer SM, Chang J, Coursey JS, Sukumar R, Zucker DS, and Olsen K. XCOM: Photon Cross Sections Database | NIST Standard Reference Database 8. 2010.

23. Hubbell JH and Seltzer SM. X-Ray Mass Attenuation Coefficients | NIST Standard Reference Database 126. 2004.

24. Klein O and Nishina Y. Ueber die Streuung von Strahlung durch freie Elektronen nach der neuen relativistischen Quantendynamik von Dirac. *Z Phys.* 1929 Nov; 52:853–68.

25. Accorsi R and Metzler SD. Analytic determination of the resolution-equivalent effective diameter of a pinhole collimator. *IEEE Trans Med Imaging.* 2004 Jun; 23:750–63.

26. Metzler SD, Bowsher JE, Smith MF, and Jaszczak RJ. Analytic determination of pinhole collimator sensitivity with penetration. *IEEE Trans Med Imaging.* 2001 Aug; 20:730–41.

27. Wieczorek H, Goedicke A, Edstroem F, Degenhardt C, Botterweck H, and Bippus R. Collimator spatial resolution. *IEEE Trans Nucl Sci.* 2005 Oct; 3:1717–21.

28. Van Audenhaege K, Vanhove C, Vandenberghe S, and Van Holen R. The evaluation of data completeness and image quality in multiplexing multi-pinhole SPECT. *IEEE Trans Med Imaging.* 2015 Feb; 34:474–86.

29. Natterer F. Inversion of the attenuated Radon transform. *Inverse Problems.* 2001 Jan; 17:113–9.

30. Compte de Buffon GLL. Essai d'arithmétique morale. *Supplément à l'Histoire Naturelle.* 1777; 4:46–123.

31. Agostinelli S et al. GEANT4 - A simulation toolkit. *Nucl Instrum Methods Phys Res A.* 2003 Jul; 506:250–303.

32. Jan S et al. GATE: a simulation toolkit for PET and SPECT. *Phys Med Biol.* 2004 Oct; 49:4543–61.

33. Forster RA and Godfrey TNK. MCNP - a general Monte Carlo code for neutron and photon transport. *Monte-Carlo Methods and Applications in Neutronics, Photonics and Statistical Physics.* 1985 Feb; 240:33–55.

34. Kawrakow I. Accurate condensed history Monte Carlo simulation of electron transport. I. EGSnrc, the new EGS4 version. *Med Phys.* 2000 Mar; 27:485–98.

35. Battistoni G, Bauer J, Boehlen TT, Cerutti F, Chin MPW, Dos Santos Augusto R, Ferrari A, Ortega PG, Kozlowska W, Magro G, Mairani A, Parodi K, Sala PR, Schoofs P, Tessonnier T, and Vlachoudis V. The FLUKA code: An accurate simulation tool for particle therapy. *Front Oncol.* 2016 May; 6:116.

36. Baro J, Sempau J, Fernandez-Varea JM, and Salvat F. PENELOPE: An algorithm for Monte Carlo simulation of the penetration and energy loss of electrons and positrons in matter. *Nucl Instrum Methods Phys Res B.* 1995 May; 100:31–46.

37. Lukas M, Kluge A, Beindorff N, and Brenner W. Accurate Monte Carlo Modeling of Small-Animal Multi-Pinhole SPECT for Non-Standard Multi-Isotope Applications. *IEEE Trans Med Imaging*. 2021 Sep; 40:2208–20.

38. Segars WP, Tsui BM, Frey EC, Johnson GA, and Berr SS. Development of a 4-D digital mouse phantom for molecular imaging research. *Mol Imaging Biol*. 2004 May; 6:149–59.

39. Blender Online Community. Blender - a 3D modelling and rendering package. Stichting Blender Foundation, Amsterdam, 2018.

40. Amako K, Guatelli S, Ivanchenko VN, Maire M, Mascialino B, Murakami K, Nieminen P, Pandola L, Parlati S, Pia MG, Piergentili M, Sasaki T, and Urban L. Comparison of Geant4 electromagnetic physics models against the NIST reference data. *IEEE Trans Nucl Sci*. 2005 Aug; 52:910–8.

41. Strydhorst JH and Wells RG. Quantitative Measurement of In Vivo Tracer Concentration in Rats with Multiplexed Multi-Pinhole SPECT. *IEEE Trans Nucl Sci*. 2014 Jun; 61:1136–42.

42. National Electrical Manufacturers Association. NEMA Standards Publication NU 1-2012: Performance measurements of gamma cameras. 2012.

43. National Electrical Manufacturers Association. NEMA Standards Publication NU 4-2008: Performance measurements of small animal positron emission tomographs. 2008.

44. Mok GSP, Du Y, Wang Y, Frey EC, and Tsui BMW. Development and validation of a Monte Carlo simulation tool for multi-pinhole SPECT. *Mol Imaging Biol*. 2010 Jun; 12:295–304.

45. Chen CL, Wang Y, Lee JJS, and Tsui BMW. Integration of SimSET photon history generator in GATE for efficient Monte Carlo simulations of pinhole SPECT. *Med Phys*. 2008 Jul; 35:3278–84.

46. Lee S, Gregor J, and Osborne D. Development and validation of a complete GATE model of the Siemens Inveon trimodal imaging platform. *Mol Imaging*. 2013 Oct; 12:1–13.

47. Rault E, Staelens S, Van Holen R, De Beenhouwer J, and Vandenberghe S. Accurate Monte Carlo modelling of the back compartments of SPECT cameras. *Phys Med Biol*. 2011 Jan; 56:87–104.

48. Garcia MP, Bert J, Benoit D, Bardies M, and Visvikis D. Accelerated GPU based SPECT Monte Carlo simulations. *Phys Med Biol*. 2016 Jun; 61:4001–18.

Original Publication | Experimental Measurements

Journal Summary List

Lukas M, Kluge A, Beindorff N, Brenner W. Multi-Isotope Capabilities of a Small-Animal Multi-Pinhole SPECT System. *J Nucl Med.* 2020 Jan; 61:152-161.

Journal Data Filtered By: **Selected JCR Year: 2020** Selected Editions: SCIE,SSCI
Selected Categories: **"RADIOLOGY, NUCLEAR MEDICINE and MEDICAL IMAGING"**
Selected Category Scheme: WoS
Gesamtanzahl: 134 Journale

Rank	Full Journal Title	Total Cites	Journal Impact Factor	Eigenfactor Score
1	JACC-Cardiovascular Imaging	14,398	14.805	0.032190
2	RADIOLOGY	72,249	11.105	0.053000
3	**JOURNAL OF NUCLEAR MEDICINE**	**32,949**	**10.057**	**0.032490**
4	IEEE TRANSACTIONS ON MEDICAL IMAGING	27,030	10.048	0.033600
5	EUROPEAN JOURNAL OF NUCLEAR MEDICINE AND MOLECULAR IMAGING	20,634	9.236	0.024430
6	MEDICAL IMAGE ANALYSIS	11,568	8.545	0.018360
7	Photoacoustics	1,093	8.484	0.001780
8	CLINICAL NUCLEAR MEDICINE	6,344	7.794	0.006990
9	Circulation-Cardiovascular Imaging	7,640	7.792	0.015510
10	ULTRASOUND IN OBSTETRICS & GYNECOLOGY	18,164	7.299	0.018820
11	INTERNATIONAL JOURNAL OF RADIATION ONCOLOGY BIOLOGY PHYSICS	50,525	7.038	0.039410
12	European Heart Journal - Cardiovascular Imaging	8,423	6.875	0.020790
13	NEUROIMAGE	119,618	6.556	0.105820
14	ULTRASCHALL IN DER MEDIZIN	2,911	6.548	0.003340
15	RADIOTHERAPY AND ONCOLOGY	22,462	6.280	0.024940
16	INVESTIGATIVE RADIOLOGY	7,700	6.016	0.007870
17	JOURNAL OF NUCLEAR CARDIOLOGY	5,882	5.952	0.005390
18	SEMINARS IN RADIATION ONCOLOGY	2,837	5.934	0.002710
19	Journal of the American College of Radiology	6,584	5.532	0.013810
20	JOURNAL OF CARDIOVASCULAR MAGNETIC RESONANCE	6,935	5.364	0.010460
…				
134	Physical and Engineering Sciences in Medicine	184	Not Available	0.000020

Multi-Isotope Capabilities of a Small-Animal Multi-Pinhole SPECT System

Mathias Lukas[1], Anne Kluge[2], Nicola Beindorff[3], and Winfried Brenner[1,4]

[1]Department of Nuclear Medicine, Charité–Universitätsmedizin Berlin, Berlin, Germany; [2]Department of Radiation Oncology and Radiotherapy, Charité–Universitätsmedizin Berlin, Berlin, Germany; [3]Berlin Experimental Radionuclide Imaging Center, Charité–Universitätsmedizin Berlin, Berlin, Germany; and [4]German Cancer Consortium, Charité Campus Berlin, Berlin, Germany

The quantitative accuracy and image quality of multi-isotope SPECT is affected by various hardware-related perturbations. The present study evaluates the simultaneous acquisition of multiple isotopes using a multiplexed multi-pinhole SPECT system, assesses the extent of different error sources, and proposes experimental procedures for its objective characterization. **Methods:** Phantom measurements with single-, dual- and triple-isotope combinations of ^{99m}Tc, ^{111}In, ^{123}I, ^{177}Lu, and ^{201}Tl were performed with the NanoSPECT/CT^{PLUS} to evaluate system energy resolution, count rate performance, sensitivity, collimator penetration, hardware versus object scatter, spectral crosstalk, spatial resolution, spatial registration accuracy, image uniformity, image noise, and image quality. **Results:** The intrinsic detector properties were suitable for the simultaneous acquisition of up to 3 isotopes with limitations for count rates exceeding 104 kcps and γ-energies lower than 75 keV. Spectral crosstalk between isotopes was more likely mediated by hardware than by source scatter and was strongly dependent on the isotope combination. Simultaneous multi-isotope acquisitions slightly degraded spatial resolution and image uniformity for spatially superimposed but not for spatially separated activity distributions while the background noise level was increased for all multi-isotope studies. For particular isotopes, collimator penetration and x-ray fluorescence contributed a significant portion of error. **Conclusion:** The NanoSPECT/CT^{PLUS} enables the simultaneous acquisition of 3 radioisotopes with high quantitative accuracy and only little loss of image quality when the activity ratio is adapted to isotope-specific count rate sensitivities and when the system calibration is performed with phantoms of appropriate size.

Key Words: multi-isotope; multiplexed multi-pinhole SPECT; performance; quantification; image quality

J Nucl Med 2020; 61:152–161
DOI: 10.2967/jnumed.119.226027

SPECT is a powerful tool for noninvasive imaging of molecular processes in living organisms (*1*). A strength of SPECT is its capability to image multiple radioisotopes simultaneously based on spectral separation of their emitted γ- or x-ray energies. This not only improves economic efficiency and subject comfort but also provides complementary functional information. Bound to biologically acting molecules, multiple isotopes enable the simultaneous characterization of different physiologic and pathologic pathways and their mutual interactions down to the picomolar range (*1*). Particularly for rapidly changing pathophysiology, the temporal information cannot be assessed by consecutive studies. Therefore, dual-isotope imaging has been used successfully for comparative studies (*2*), competing studies (*3*), and dose–response assessment in therapeutic applications (*4*).

However, imaging multiple isotopes introduces several physical interferences that hamper image quality and quantification accuracy. Additional isotopes, for instance, inevitably increase the amount of radioactivity in the field of view (FOV). Moreover, each radioisotope has its own decay schema with different half-lives, decay modes, and emission energies. Specific attenuation, scatter, and γ-branching ratios lead to different detection efficiencies, and multi-isotope activity ratios therefore need to be selected with care.

The main limitation for multi-isotope imaging is the finite separability of energies, which causes crosstalk between isotope-specific energy windows (*5*). Spectral crosstalk can arise from partially overlapping photo peaks due to detector system imperfect energy resolution or as down-scatter from higher-energy emissions. Crosstalk can also arise from collimator effects such as x-ray fluorescence or collimator penetration. The related energy ambiguities, finally, degrade the quantitation accuracy, spatial resolution, and quality of the reconstructed SPECT images.

Crosstalk correction methods have been described for a variety of radioisotope combinations based on energy window subtraction or modeling (*5*). The former methods can fail for lower photon energies because of insufficient energy resolution. They are usually restricted to dual-isotope combinations, as commercial preclinical SPECT systems support only a few energy windows that can be acquired simultaneously. Modeling approaches, on the other hand, can be applied to an arbitrary number of emission energies but are computationally intensive. For this reason, models typically focus on source scatter and neglect scatter contribution from hardware components. However, in preclinical SPECT, hardware effects are the predominant source of error (*6*), whereas the imaging subjects are small and, therefore, crosstalk caused by subject scatter is small as well (*7*). Knowledge about the individual system response for each radioisotope and its hardware-mediated crosstalk effects turns out to be important for preclinical multi-isotope study design and protocol optimization.

The aim of the present study was to evaluate the multi-isotope capabilities of the NanoSPECT/CT^{PLUS} (Mediso) with regard to intrinsic detector properties, quantification accuracy, and reconstructed

Received Jan. 14, 2019; revision accepted Jun. 12, 2019.
For correspondence or reprints contact: Mathias Lukas, Department of Nuclear Medicine, Charité–Universitätsmedizin Berlin, Augustenburger Platz 1, 13353 Berlin, Germany.
E-mail: mathias.lukas@charite.de

image quality. Performance metrics for single-, dual-, and triple-isotope combinations of ^{99m}Tc, ^{111}In, ^{123}I, ^{177}Lu, and ^{201}Tl and their hardware-mediated crosstalk errors were determined. These data are used to assess the need for complex correction methods and, finally, to optimize the experimental design of future multi-isotope experiments.

MATERIALS AND METHODS

System Description

The NanoSPECT/CT^{PLUS} is a dedicated SPECT/CT system designed for high-resolution, high-sensitivity small-animal imaging that can be configured with up to 4 detector heads. Each of its thallium-doped sodium iodide scintillation crystals (NaI(Tl)) has a size of 262 × 255 × 6.35 mm^3 and is coupled to 33 position-sensitive 50.8 mm (2 in) diameter photomultiplier tubes that yield an intrinsic spatial resolution of 3.5 mm for ^{99m}Tc (*8*). Imaging collimation is achieved either by parallel-hole or by combined pyramid-pinhole collimators that ensure bore opening sizes of 250 mm or up to 80 mm, respectively. To increase the count rate sensitivity for pinhole acquisitions, the detectors feature multiplexed multi-pinhole collimation with 9–16 pinholes per detector. The pinhole projections are interlaced to optimize use of detector surface while minimizing multiplexing. The NanoSPECT/CT^{PLUS} is able to acquire 4 energy windows simultaneously. It is delivered with the software HiSPECT (Scivis GmbH), an ordered-subset expectation maximization algorithm for image reconstruction.

Data Acquisition and Processing

In this study, 4 different 9-pinhole collimators were used: mouse high resolution (MH), mouse ultra-high resolution (MU), rat high resolution (RH), and rat ultra-high resolution (RU). Their geometric specifications are listed in Supplemental Table 1 (supplemental materials are available at http://jnm.snmjournals.org). For planar and SPECT scans, the image acquisition matrix was set to 256 × 256 pixels^2 with a resolution of 1.0 × 1.0 mm^3/pixel^3. All SPECT images were acquired with 56 angular projections and 60 s duration using the energy windows shown in supplemental Table 2. Radioisotope emission spectra were sampled with equidistant but energy-range-adapted channel width from 0.2 to 0.7 keV/channel. Before the measurements, the SPECT system was calibrated according to the manufacturer's instructions, which included calibrations for energy, linearity, uniformity, center of rotation, and collimator offset.

Ordered-subset expectation maximization reconstruction was set either to standard (0.3 × 0.3 × 0.3 mm^3, 9 iterations, 35% gaussian smoothing, crosstalk correction) or to phantom (0.2 × 0.2 × 0.2 mm^3, 24 iterations, 25% gaussian smoothing, crosstalk correction). The gaussian filter was applied to the projections before reconstruction and was given as a percentage of a reference resolution predefined by the vendor.

For region-of-interest analyses, the PMOD software package (version 3.7; PMOD Technologies) was used. Image processing and mathematic analyses were performed with Matlab 9.0 (MathWorks).

Energy Resolution

Measurements were performed with MH collimators using different isotopes that provide discrete γ-spectra: ^{67}Ga, ^{68}Ga, ^{99m}Tc, ^{111}In, ^{123}I, ^{131}I, ^{153}Sm, and ^{177}Lu. Micro test tubes were filled with approximately 100 kBq/10 μL each and were centered to the FOV. Radioisotope γ-emission spectra were acquired to at least 100,000 counts. To estimate the absolute and relative energy resolutions ΔE_ν and $\Delta E_\nu/E_\nu$, the full width at half maximum (FWHM) was calculated fitting the data to the following gaussianlike equation:

$$\dot{N}(E_\nu) = \dot{N}_{max} \cdot e^{-4\ln(2)\cdot\left(\frac{E_\nu - E_{\nu,0}}{\Delta E_\nu}\right)^2}.$$

Here, $\dot{N}(E_\nu)$ denotes the count rate with maximal intensity $\dot{N}_{max}$ at the γ-energy $E_{\nu,0}$. Finally, the overall energy response of the detector was described using the following exponential equation:

$$\frac{\Delta E_\nu}{E_\nu}(E_\nu) = \left(\frac{\Delta E_\nu}{E_\nu}\right)_{max} \cdot e^{-\lambda E} + \left(\frac{\Delta E_\nu}{E_\nu}\right)_{min}.$$

The capability of the detector to resolve an incident photon of energy E_ν is given by the fitting parameter λ, the best possible energy resolution $(\Delta E_\nu/E_\nu)_{min}$ and the worst $((\Delta E_\nu/E_\nu)_{max} + (\Delta E_\nu/E_\nu)_{min})$.

Count Rate Performance

A 2-fold serial dilution of ^{99m}Tc with activities from 25 MBq to 0.2 kBq was prepared and centered in the FOV. Planar images were acquired for 30 s without collimators using 4 energy windows: 40 keV ± 50%, 120 keV ± 50%, 360 keV ± 50%, and 900 keV ± 40%. The sum of counts for each detector head was extracted. Considering linearity under low-count-rate conditions, the true count rate was linearly extrapolated from the 5 lowest measured count rates. According to the paralyzed dead-time model, the real incident count rate n was related to the measured count rate m and the paralyzed dead-time extension τ by

$$m(n) = ne^{-n\tau} + n_{bkg}.$$

Assuming negligible background n_{bkg} and a decay constant $\lambda = \ln(2)$ for a 2-fold serial dilution, the dead time τ was determined substituting n by $n_o e^{-\lambda t}$ and rearranging the equation to

$$\ln(m) + \ln(2)t = -n_0\tau \cdot 2^{-t} + \ln(n_0).$$

Plotting $\ln(m) + \ln(2)t$ against 2^{-t}, the slope of the linear regression is given by $-n_0\tau$ and the intercept by $\ln(n_0)$. Dead time was determined by calculating the ratio of $n_0\tau$ and the initial true count rate n_0. To analyze the count pileup fraction, the count rate of the energy window 360 keV ± 50% was related to the total count rate, since it includes the double- and triple-piled ^{99m}Tc photo peaks at 281.0 and 421.5 keV.

System Sensitivity

For sensitivity measurements, micro test tubes were filled with approximately 10 MBq/10 μL of ^{99m}Tc, ^{111}In, ^{123}I, ^{177}Lu, or ^{201}Tl. The absolute activity in each sample was measured in a certified dose calibrator, ISOMED 2010 (MED Dresden GmbH). These point sources were centered in the FOV, and images were acquired in planar mode for 10 min using MH, MU, RH, and RU apertures. The sum of counts for each detector head was extracted and related to the total activity in the FOV. The experiment was repeated using 15%, 10%, and 5% energy windows.

Collimator Penetration

The fraction of collimator photon penetration was estimated for all apertures from the planar images acquired for sensitivity measurements (^{99m}Tc, ^{111}In, ^{123}I, ^{177}Lu, and ^{201}Tl). The pinhole projections of the point source on the planar images were segmented using an isocontour at 5% of the maximum intensity. This contour was enlarged by 1 FWHM of intrinsic spatial resolution (3.5 mm). The sum of counts outside the contour was assumed to be collimator penetration.

Hardware Scatter

Scatter, tungsten x-ray fluorescence, and photo-peak fractions as a function of phantom size were investigated for ^{99m}Tc to extrapolate the intrinsic hardware scatter fraction. A point source and cylindric

phantoms with diameters of 1, 6, 13, 21, and 30 mm were filled with 20 MBq of ^{99m}Tc. γ-photon spectra were collected for 5 min using MH apertures. The spectral components were separated with regard to the following Compton scatter equation:

$$E'_\nu(\theta) = \frac{E_\nu}{1 + \frac{E_\nu}{m_e c^2}(1 - \cos\theta)}.$$

The energy of the scattered photon E'_ν depends on the incident photon energy E_ν, the scattering angle θ, and the electron rest mass $m_e c^2$. Compton scattered photons lead to a continuous signal with energies between $E'_\nu(\pi)$ and $E'_\nu(0)$. Hence, in relation to the total count rate $\dot{N}_t$, fractions for tungsten x-ray fluorescence F_T, Compton scatter F_C, and the photo peak F_P were calculated using

$$\dot{N}_t = \int_0^\infty \dot{N}(E)dE$$

$$F_T = \frac{1}{\dot{N}_t}\int_{E_1}^{E_2} \dot{N}(E)dE$$

$$F_C = \frac{1}{\dot{N}_t}\left(\int_{E_2}^{E_3} \dot{N}(E)dE - \int_{E_3}^{E_4} \dot{N}(E)dE\right)$$

$$F_P = \frac{2}{\dot{N}_t}\int_{E_3}^{E_4} \dot{N}(E)dE$$

With regard to an energy resolution $\Delta E/E$ of 10% and tungsten's centroid energies for $k\alpha$ and $k\beta$ x-ray transitions $E_{k\alpha} = 67.6$ keV and $E_{k\beta} = 58.8$ keV, the lower and upper integral limits for ^{99m}Tc were set to

$$E_1 = E_{k\alpha}(1 - 2\Delta E/E) = 47.1 \text{ keV}$$

$$E_2 = \left(E_{k\beta} + E'_\nu(\pi)\right)\Big/2 = 79.1 \text{ keV}$$

$$E_3 = E_\nu = E'_\nu(0) = 140.5 \text{ keV}$$

$$E_4 = E_{k\alpha}(1 + 2\Delta E/E) = 168.6 \text{ keV}.$$

Hardware Crosstalk

Baseline multi-isotope quantification accuracy was investigated for all possible isotope combinations including ^{99m}Tc, ^{111}In, ^{123}I, ^{177}Lu, and ^{201}Tl (~10 MBq/10 μL). To minimize phantom scatter, a point source of each isotope was centered in the FOV, and energy spectra were sampled for 5 min successively using the MH apertures. If photons of isotope A were incorrectly measured in energy window w_B of isotope B, the absolute spectral crosstalk factors $SCF_{A\to B}$ for 1:1 mixtures were calculated by the following ratio:

$$SCF_{A\to B} = \dot{N}_B/\dot{N}_A.$$

The count rates $\dot{N}_A$ (spill-out) and $\dot{N}_B$ (spill-in), both induced by isotope A, were given by integration of the spectral count rate histogram $\dot{N}(E)$ within the energy windows w_A and w_B around its corresponding energy peak E_ν:

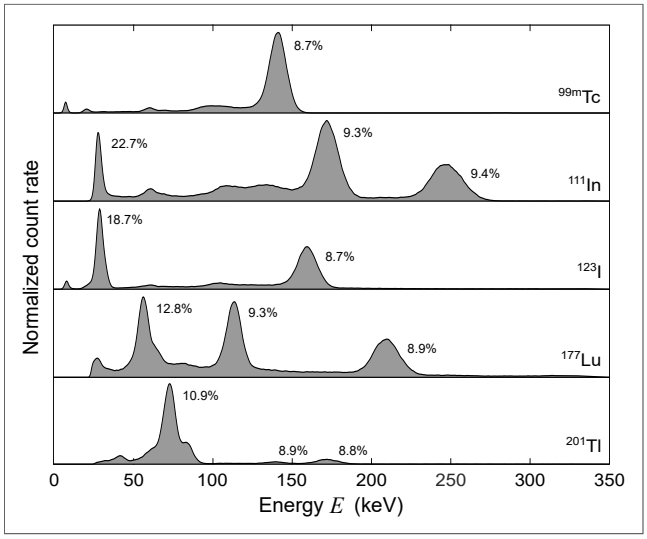

FIGURE 1. Spectra and photo peak energy resolutions of radioisotopes acquired on NanoSPECT/CT^{PLUS}. Different radioisotopes provide different decay properties that need to be considered for multi-isotope protocol optimization: ^{99m}Tc (6.0 h, 100% IT); ^{111}In (2.8 d, 100% ε); ^{123}I (13.2 h, 100% ε); ^{177}Lu (6.7 d; 78.6% β^-, 21.4% IT); ^{201}Tl (3.0 d, 100% ε). IT = isomeric transition; ε = electron capture.

$$\dot{N}_{A,B} = \int_{E_\nu\left(1-\frac{w_{A,B}}{2}\right)}^{E_\nu\left(1+\frac{w_{A,B}}{2}\right)} \dot{N}(E)dE.$$

For an arbitrary multi-isotope experiment, the falsified count rate of isotope B can be corrected in the first approximation by scaling the planar images according to

$$\dot{N}_{B,corr} = \dot{N}_B - \dot{N}_A \; SCF_{A\to B}.$$

Spatial Resolution and Registration

Glass capillary tubes with an inner diameter of 1 mm were filled with approximately 50 MBq/mL of either ^{99m}Tc, ^{111}In, ^{123}I, ^{177}Lu, or ^{201}Tl. Additional capillary tubes were filled with 1:1:1 mixtures of ^{99m}Tc/^{123}I/^{201}Tl, ^{99m}Tc/^{111}In/^{201}Tl, and ^{99m}Tc/^{111}In/^{177}Lu. Five capillary tubes of the same single-isotope probe were aligned circularly around the axial axis with a radial distance of 5 mm (Supplemental Fig. 1). SPECT was acquired using MH apertures. The acquisition was repeated for the multi-isotope mixtures aligned equally spaced between the single-isotope tubes (Supplemental Fig. 1). Single and multi-isotope measurements were repeated using the same setup, but centered within a 25-mm-diameter scatter phantom. All images were reconstructed using phantom parameters. FWHM and full width at tenth maximum (FWTM) were determined according to the National Electrical Manufacturers Association publication (*9*). For multiple-window spatial registration measurement, the line sources filled with ^{111}In were acquired for each γ-emission photo peak at 23.6, 171.3, and 245.4 keV using a 20% energy window. The reconstructed images underwent rigid registration using only transaxial translations.

Uniformity and Noise

To estimate reconstructed image uniformity and noise, 10-mm-diameter cylindric phantoms were filled with either ^{99m}Tc, ^{111}In, ^{123}I, ^{177}Lu, or ^{201}Tl. Additionally, phantoms with 1:1:1 mixtures of

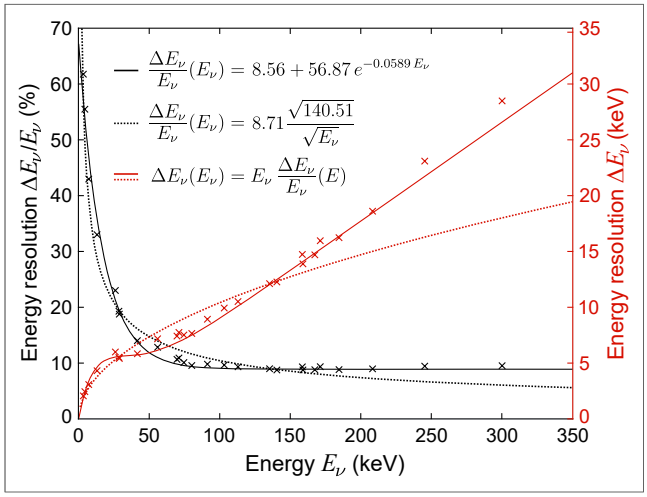

FIGURE 2. Relative (black) and absolute (red) energy resolution of NanoSPECT/CT^{PLUS} detector expressed as exponential (solid lines) and inverse square root law (dotted lines). Energy resolution is suitable for single-, dual- and triple-isotope studies above 75 keV. For energies below, resolution is restricted by nonproportional light yield of scintillator NaI(Tl) and hampers separation of multiple isotopes.

^{99m}Tc/^{123}I/^{201}Tl, ^{99m}Tc/^{111}In/^{201}Tl, and ^{99m}Tc/^{123}I/^{177}Lu were prepared. Three phantoms of the same single-isotope probe were aligned circularly around the axial axis with a radial distance of 10 mm (Supplemental Fig. 1). SPECT was acquired using MH apertures. The acquisitions were repeated for the multi-isotope mixtures equally spaced between the single-isotope phantoms (Supplemental Fig. 1). All images were reconstructed using phantom parameters. For the activity distribution A, the uniformity and noise coefficients UC and NC were calculated using

$$UC = \frac{A_{max} - A_{min}}{A_{max} + A_{min}}$$

$$NC = \frac{\sigma_A}{m_A}.$$

Here, σ_A denotes the SD and m_A the mean of the activity distribution.

Image Quality

The image quality was investigated for the isotope combinations ^{99m}Tc/^{123}I/^{201}Tl, ^{99m}Tc/^{111}In/^{201}Tl, and ^{99m}Tc/^{123}I/^{177}Lu. A micro Jaszczak phantom (d = 25 mm) with 6 fields of rods (d = 0.7−1.2 mm) was consecutively filled with each of the isotopes (~5 MBq/mL) and finally with a mixture of them (ratio, 1:1:1). SPECT was acquired using MH apertures. Images were reconstructed using phantom parameters. The experiment was repeated for spatially separated activity distributions using a modified Jaszczak phantom (d = 28 mm) with 6 fields of rods (d = 1.5/5.0 mm) and 2 activity ratios (2.5 and 5 MBq/mL).

RESULTS

Energy Resolution

Energy spectra and photo-peak energy resolutions of radioisotopes used in this study are shown in Figure 1. The energy response function of the detector is shown in Figure 2. For photon energies greater than 75 keV, the energy resolution was below 10% FWHM and remained stable up to 500 keV. For lower photon energies, the resolution decreased exponentially up to 60% FWHM. The commonly used but simplified $1/\sqrt{E}$ model did not reflect the measured energy response function sufficiently (Fig. 2).

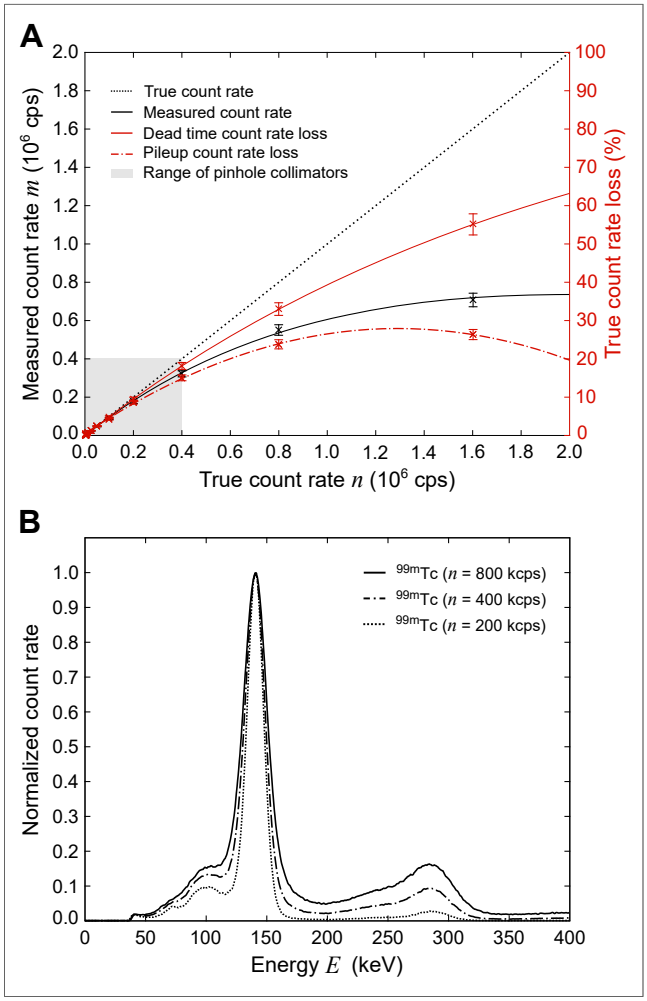

FIGURE 3. Count rate performance (A) and pileup spectra (B) of NanoSPECT/CT^{PLUS} detector. Count rate loss is low for single-, dual- and triple-isotope experiments, as sensitivity of pinhole collimation barely allow 400 kcps to be exceeded (gray area). For triple-isotope studies with high total activities, pileup may affect quantitative accuracy and image quality of high-energy radioisotopes.

Count Rate Performance

The count rate performance and relative count rate losses per NanoSPECT/CT^{PLUS} detector head are plotted in Figure 3A. The

TABLE 1
Count Rate Sensitivity per Detector Head Using 20% Energy Window

	Collimator sensitivity			
Isotope	MH	MU	RH	RU
^{99m}Tc	205 ± 11	77 ± 8	191 ± 6	81 ± 4
^{111}In	317 ± 25	154 ± 23	289 ± 17	158 ± 12
^{123}I	207 ± 13	89 ± 3	187 ± 7	96 ± 6
^{177}Lu	59 ± 5	25 ± 3	53 ± 3	26 ± 2
^{201}Tl	213 ± 12	83 ± 8	206 ± 4	95 ± 3

Data are mean ± SD in cps/MBq.

TABLE 2
Count Rate Sensitivity per Detector Head Using MH Collimators

Isotope	Energy	Energy window sensitivity				
		Total	20%	15%	10%	5%
^{99m}Tc	140.5	294	205	192	158	94
^{111}In	171.3	482	189	175	145	85
	245.4	482	128	120	101	60
^{123}I	159.0	562	207	190	155	90
^{177}Lu	56.1	84	15	12	9	5
	112.9	84	23	21	17	10
	208.4	84	21	19	16	9
^{201}Tl	72.3	516	188	164	127	72
	167.4	516	25	23	18	11

Energy is in keV; sensitivity is in cps/MBq.

dead time was found to be best described by the paralyzed dead-time model with a dead time of 492 ± 6 ns. Total count losses of 5%, 10%, and 20% were observed at true count rates of 104 ± 0.2, 214 ± 0.2, and 454 ± 0.2 kcps. Pileup fractions of 5%, 10%, and 20% were observed at true count rates of 112, 248, and 598 kcps. Exemplary pileup spectra for measured count rates of 200, 400, and 800 kcps are shown in Figure 3B.

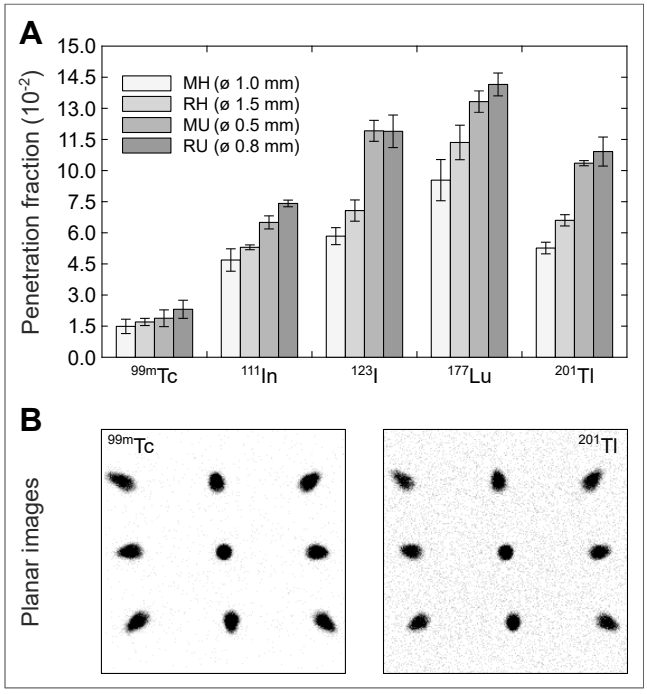

FIGURE 4. Photon penetration fractions for different collimators (A) and multi-pinhole projections of RU collimator (B). Given penetration fractions partly involve collimator scatter and, in case of ^{201}Tl, tungsten x-ray fluorescence. Photon penetration increases background counts in planar projections and therefore degrades image quality and signal-to-noise ratio of both single- and multi-isotope reconstructions.

System Sensitivity

Table 1 summarizes the system sensitivities per detector for all aperture sets and isotopes using 20% energy windows. Sensitivity was highest for the MH collimator, followed by RH, RU, and MU. Narrowing the energy window width from 20% to 15%, 10%, or 5% caused a mean sensitivity loss of 9.4%, 27.0%, and 57.6%, respectively (Table 2). This reduction was slightly higher for lower energy peaks, as for ^{177}Lu (56.1 keV) and ^{201}Tl (72.3 keV). For ^{111}In and a 20% energy window, the 171.3 and 245.4 keV photo peaks contributed 59.7% and 40.3%, respectively, to the sensitivity. For ^{177}Lu, 25.4%, 39.2%, and 35.4% of counts originated from 56.1, 112.9, and 208.4 keV photo peaks, respectively. For ^{201}Tl, 88.2% and 11.8% originated from the 72.3 and 167.4 keV photo peaks, respectively. These observed count contribution fractions changed with energy window width because of the improved

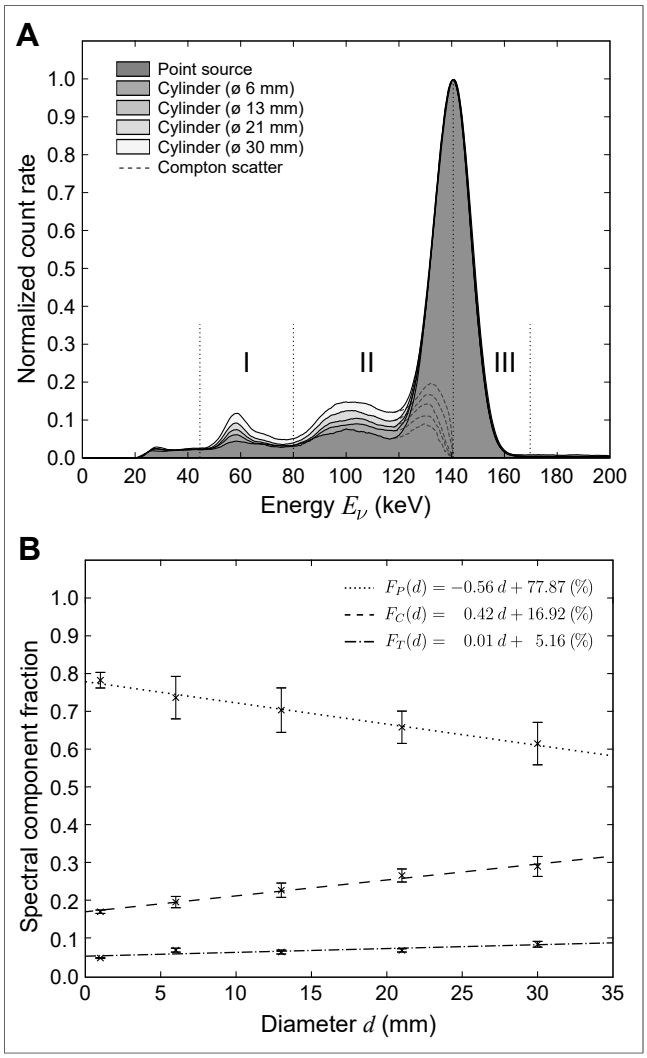

FIGURE 5. Spectra (A) and spectral component fractions (B) for ^{99m}Tc phantoms of different sizes. Three energy windows were used to estimate fractions of tungsten x-ray fluorescence F_T (I), Compton scatter F_C (II), and full-energy peak F_P (III). Scatter fraction increases only slightly for rodent-sized objects and therefore is caused mainly by hardware components. Disproportionately rising Compton maxima at 100 and 135 keV indicate change in detected scatter angles. Backward scatter from hardware is gradually overcome by forward scatter from measured object. Corresponding energy shift forces increase of tungsten x-ray fluorescence.

TABLE 3
Quantification Errors for Multi-isotope Studies Using 1:1 Activity Ratios and MH Apertures

		Isotope A (spill-out)									
		20% energy window					10% energy window				
Isotope B (spill-in)	Peak	^{99m}Tc	^{111}In	^{123}I	^{177}Lu	^{201}Tl	^{99m}Tc	^{111}In	^{123}I	^{177}Lu	^{201}Tl
^{99m}Tc	140.5	—	20.0	33.1	1.8	6.2	—	12.8	12.3	1.1	4.7
^{111}In	171.3	2.5	—	87.9	1.9	13.1	1.7	—	47.6	1.3	12.1
	245.4	2.5	—	7.5	2.4	1.8	1.8	—	4.8	0.8	0.7
^{123}I	159.0	33.0	72.5	—	1.7	11.2	5.4	40.1	—	1.1	5.1
^{177}Lu	56.1	32.7	67.1	55.2	—	105.8	29.3	59.1	47.8	—	82.5
	112.9	69.7	141.7	91.7	—	26.0	44.7	98.0	61.6	—	17.8
	208.4	15.0	93.9	57.4	—	32.1	10.0	46.8	36.6	—	21.6
^{201}Tl	72.3	2.9	4.9	4.6	2.2	—	2.0	3.6	3.6	1.4	—
	167.4	43.0	749.4	755.5	14.0	—	8.8	735.2	593.2	9.8	—

Peak is in keV; error is in %.

energy resolution at higher photo-peak energies. For assessment of isotope-specific dead-time behavior, the total point source sensitivities measured for the entire energy range are given in column "Total" in Table 2. The dark count rate for the full energy range was 54 ± 5 cps per detector head.

Collimator Penetration

Photon penetration fractions for different isotopes and collimators are shown in Figure 4. ^{99m}Tc showed low penetration fractions below 2.3% for all aperture sets, whereas ^{123}I and ^{177}Lu showed up to 13.2% photon penetration because of their branching ratios for high γ-emissions. Although ^{201}Tl does not emit high-energy photons, penetration fractions were higher than for ^{111}In, with up to 10% caused mainly by x-ray fluorescence of the collimator.

Hardware Scatter

Figure 5 shows ^{99m}Tc spectra and spectral component fractions for different phantom sizes. As expected, the fraction of Compton scatter increased with object size, associated with a reduction of the photo-peak fraction. Within the phantom diameter range evaluated, this dependency was found to be linear, with −0.56%/mm for the photo peak and 0.42%/mm for the Compton scatter fraction. The disproportionately rising maxima of the Compton spectrum at about 100 and 135 keV indicated a change in detected Compton scatter angles. With larger objects, the fraction of backward scattering that originates mainly from hardware components was superimposed by forward scattering from the phantom. Furthermore, the portion of characteristic x-rays from the shielding and the collimator increased slightly with phantom size. Overall, 16.9% scatter and 5.6% characteristic x-rays caused solely by the hardware were measured as baseline scatter for a ^{99m}Tc point source. Other radioisotopes showed higher overall scatter fractions including scatter, x-ray fluorescence, and collimator penetration, with 52.9% for ^{111}In, 42.8% for ^{123}I, 32.9% for ^{177}Lu, and 28.7% for ^{201}Tl.

Hardware Crosstalk

Table 3 summarizes the absolute quantification errors for dual-isotope combinations without object source scatter. The table columns list the isotope emissions (spill-out) that affect the energy windows of the isotopes shown in the rows (spill-in). For an optimal isotope combination, quantification errors should be below 10%. Narrowing the 20% energy window to 10% reduced errors specifically for those isotope combinations whose photo peaks overlap because of the restricted energy resolution. The error of ^{123}I caused by ^{99m}Tc spill-in, for instance, was reduced from 33.0% to 4.2%. Since the γ-branching ratio of ^{177}Lu is low (Table 1), it was heavily affected by all other admixed isotopes. This was also observed for the 167.0 keV peak of ^{201}Tl.

The overall error of an arbitrary multi-isotope combination can be estimated, summing all peaks and energy windows used. An experimental setup with 1:1:1 mixtures and energy windows ^{99m}Tc/140.5 keV/10%, ^{123}I/159.0 keV/10%, ^{177}Lu/112.9 keV/10%, and ^{177}Lu/208.4 keV/20% demonstrated quantification errors: ^{99m}Tc, 10% (9.2% + 0.8%); ^{123}I, 5.0% (4.2% + 0.8%); and ^{177}Lu, 153.0% (34.6% + 46.0% + 15.0% + 57.4%).

For other isotope mixing ratios, error values scale linearly. A 1:2:3 mixture would lead to the following errors: ^{99m}Tc, 20.8% (2 × 9.2% + 3 × 0.8%); ^{123}I, 3.3% (1/2 × 4.2% + 3/2 × 0.8%); and ^{177}Lu, 85.5% (1/3 × 34.6% + 2/3 × 46.0% + 1/3 × 15.0% + 2/3 × 57.4%).

TABLE 4
Spatial Resolution With and Without Scatter Using MH Collimators

	No scatter		Scatter	
Isotope	Single	Multi	Single	Multi
^{99m}Tc	0.70/1.27	0.71/1.81	0.72/1.46	0.80/1.93
^{111}In	0.72/1.35	0.80/1.55	1.07/2.08	1.07/2.06
^{123}I	0.73/1.38	0.69/1.30	0.75/1.82	0.78/1.97
^{177}Lu	0.69/1.37	0.70/2.18	0.81/1.78	0.81/2.33
^{201}Tl	0.71/1.35	0.71/1.35	0.79/1.62	0.82/1.82

Single = single and multiple adjacent.
Multi = multiple superimposed.
Data for FWHM/FWTM in mm.

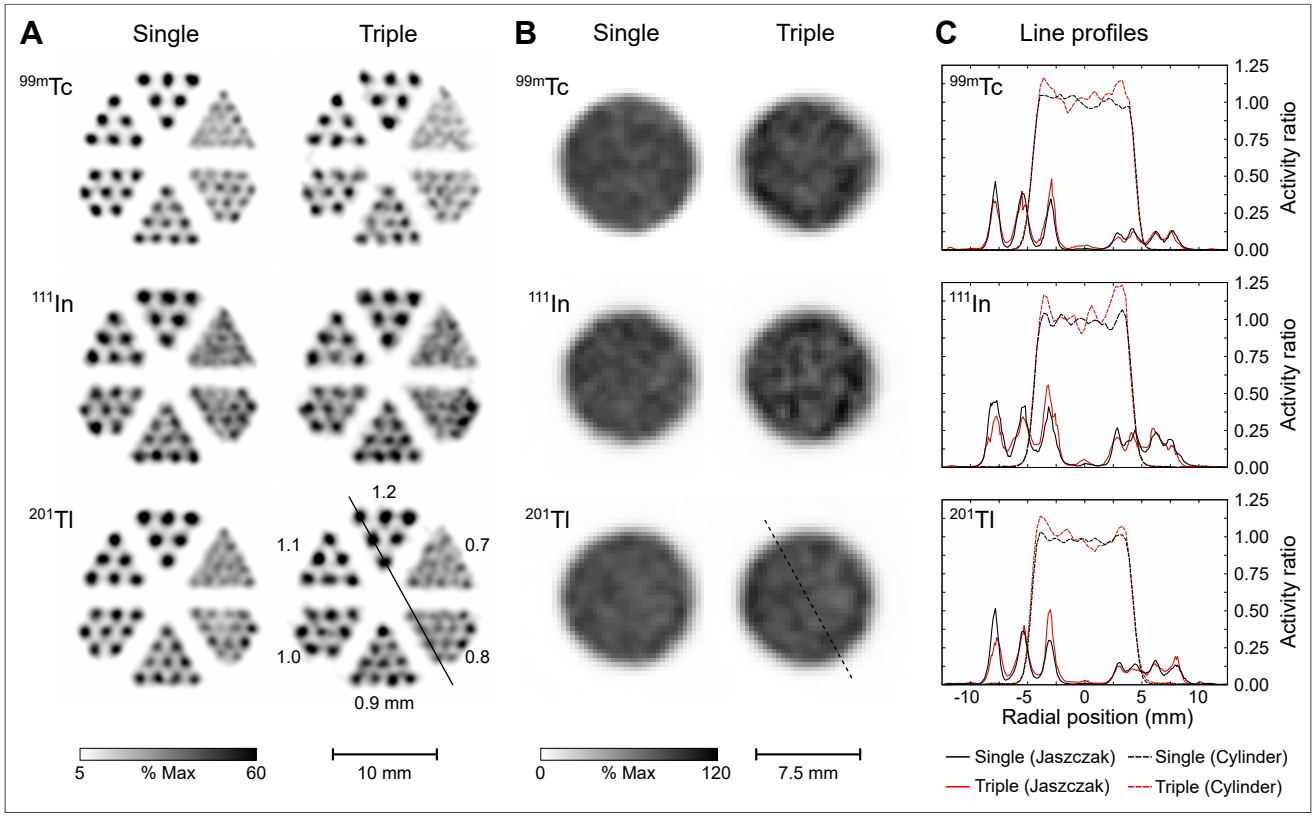

FIGURE 6. Small-animal Jaszczak phantom (A), uniformity phantom (B), and line profiles of single- and triple-isotope mixtures (C). Compared with single-isotope acquisitions, multiple superimposed isotopes degrade image quality slightly in terms of geometric distortion, background level, and overall noise. Multiple superimposed isotopes tend to degrade uniformity because of enhanced activity distributions at phantom edges.

Spatial Resolution and Registration

The spatial resolution for line sources in air and within a scatter phantom are summarized in Table 4. FWHM was not significantly affected by multiple isotopes, whereas FWTM was increased for spatially superimposed activity distributions. By contrast, scatter increased both FWHM and FWTM for single- and multi-isotope measurements. The spatial registration of multiple energy windows showed a negligible displacement of maximally 0.15 mm.

Uniformity and Noise

Single- and triple-isotope image reconstructions of the uniformity phantom for the most challenging isotope combination, ^{99m}Tc/^{111}In/^{201}Tl, are shown in Figure 6B. Numeric data results are listed in Table 5. The integral image uniformity was remarkably good for both single- and triple-isotope SPECT acquisitions. Multiple isotopes tended to degrade image uniformity only for superimposed activity distributions. Their line profiles showed slightly increased activity concentrations and enhanced edge profiles (Fig. 6C). Even though the image noise measure was similar for all single- and multi-isotope combinations, the line profiles indicated a slight increase in noise for multiple mixed isotopes. Background noise was significantly increased for both superimposed and adjacent multi-isotope distributions. These results were also found for other triple-isotope combinations evaluated (^{99m}Tc/^{123}I/^{201}Tl and ^{99m}Tc/^{123}I/^{177}Lu).

Image Quality

Image reconstructions of a micro Jaszczak phantom for the most complex isotope combination, ^{99m}Tc/^{111}In/^{201}Tl, are shown in Figure 6A. Compared with single-isotope acquisitions, multiple superimposed isotopes degraded image quality slightly in terms of geometric distortion, background level, and overall noise. The line profiles (Fig. 6C) showed a more irregular pattern for triple- than for single-isotope acquisitions. The mean reconstructed activity concentration for multiple superimposed isotopes was slightly increased (<10%) but was overcompensated by partial-volume effects of small activity distributions. To a lesser extent, these results were also observed for other triple-isotope combinations without ^{111}In (^{99m}Tc/^{123}I/^{201}Tl and ^{99m}Tc/^{123}I/^{177}Lu). In the case of adjacent

TABLE 5
Reconstructed Image Uniformity and Noise Using MH Collimators

	Uniformity		Noise	
Isotope	Single	Multi	Single	Multi
^{99m}Tc	21 ± 3	25 ± 5	7 ± 2	7 ± 1
^{111}In	20 ± 5	29 ± 7	7 ± 1	9 ± 3
^{123}I	18 ± 5	28 ± 7	7 ± 1	6 ± 1
^{177}Lu	46 ± 4	42 ± 4	12 ± 2	12 ± 2
^{201}Tl	20 ± 4	23 ± 3	6 ± 2	6 ± 1

Single = single and multiple adjacent.
Multi = multiple superimposed.
Data are mean ± SD.

activity distributions (Fig. 7), the image quality loss was negligible. Only a slight increase of background level and overall noise could be observed. Partial-volume effects contributed the main portion of error.

DISCUSSION

The present study evaluated the multi-isotope capabilities of the NanoSPECT/CT^{PLUS}. Although some performance characteristics of the NanoSPECT/CT have been reported (*10,11*), a comprehensive description on its improved successor, the NanoSPECT/CT^{PLUS}, has not (to our knowledge) been published.

The NanoSPECT/CT^{PLUS} showed an energy resolution of 8.7% FWHM for ^{99m}Tc (Fig. 2), which was in agreement with other photomultiplier tube–based 0.635 cm (0.25 in) NaI(Tl) detectors used for clinical and preclinical purposes (*10*). For photon energies below 75 keV, the energy resolution decreased exponentially because of the nonproportional light yield of the scintillator (*12*). The commonly used but simplified $1/\sqrt{E}$ model did not reflect the measured energy response sufficiently (Fig. 2). This model considers only the variation of photoelectrons released at the photocathode of the photomultiplier. Other parameters such as the variance of the photomultiplier gain or the associated electronics should be considered as well. Another reason might be the manifold characteristic x-ray energies below 100 keV, which are spin-off products of nuclear decay and disturb the monoenergetic measurement condition needed. However, the energy resolution was sufficient for single-isotope studies because self-scatter within the standard 20% energy window is negligible (*7*). For multiple radioisotopes, source scatter can lead to imperfect separation of close γ-lines as shown in the results obtained for ^{99m}Tc/^{123}I (140.5 keV, 159.0 keV, Δ13%) and ^{123}I/^{111}In (159.0 keV/171.3 keV, Δ9%) (Fig. 1; Table 3). Two individual photo peaks acquired with 10% energy resolution, for instance, with energy distances of 10%, 15%, and 20% will overlap by around 21%, 7%, and 2%, respectively. For isotope combinations with low energies such as ^{111}In/^{123}I (23.6 keV, 28.0 keV), this direct spectral crosstalk was increased because of the lower energy resolution. In general, crosstalk caused by the finite energy resolution can be reduced by narrowing the energy windows, but this also decreases valuable sensitivity (Table 2).

Compared with parallel-hole collimation, the sensitivity of pinhole collimators is reduced at the expense of spatial resolution (*13*). Therefore, the NanoSPECT/CT^{PLUS} provides multi-pinhole apertures (*8*) resulting in good system sensitivity comparable to other preclinical scanners (Table 1) (*10*). For multi-energy isotopes such as ^{111}In, the contribution fractions of each γ-energy changed with energy window width because of the improving energy resolution toward higher energies. For particular isotopes, the sensitivity was affected by collimator photon penetration. High-energy photons of ^{123}I (529.0 keV) or ^{177}Lu (319.0 keV, 413.7 kV, 418.5 keV), for instance, could not be fully absorbed in the collimators, were scattered, and contributed to background counts.

In addition to energy resolution and sensitivity, detector dead-time behavior is crucial for multi-isotope imaging. Compared with other NaI(Tl) SPECT systems, count rate performance for the NanoSPECT/CT^{PLUS} was excellent (*14*). The total dead time of 492 ns per detector head (Fig. 3) corresponds to nearly twice the scintillation decay time of NaI(Tl) at room temperature (*15*). The portion of pileup counts was low over a wide activity range. For pinhole apertures and activity levels of up to 350 MBq of ^{99m}Tc, 215 MBq of ^{111}In, 180 MBq of ^{123}I, 1,225 MBq of ^{177}Lu, or 200 MBq of ^{201}Tl, count rate losses were below 5% and can be considered negligible. These radioactivity amounts are not likely to be exceeded for either single- or multi-isotope studies because the intravenous administration volume is restricted to 0.125 mL for mice (25 g) and 1.25 mL for rats (250 g) (*16*). Overall, dead time and sensitivity results obtained in this study allow the conclusion to be drawn that the count rate performance of the NanoSPECT/CT^{PLUS} does not contribute significant errors to either single- or multi-isotope studies.

Although sensitivity, dead time, and energy resolution are constant detector properties, variable errors such as attenuation, scatter, and x-ray fluorescence depend on the geometry of both the photon source and the surrounding hardware. For ^{99m}Tc, the NanoSPECT/CT^{PLUS} showed a high baseline photo-peak fraction of about 78% (Fig. 5). Thus, 22% of photo-peak loss is caused by hardware effects. Of this fraction, 17% was due to Compton scatter in the animal bed, collimators, shielding, and the detector itself. Scatter increased only by 6% for mouse-sized and 12% for rat-sized objects. The disproportionate rise in the Compton

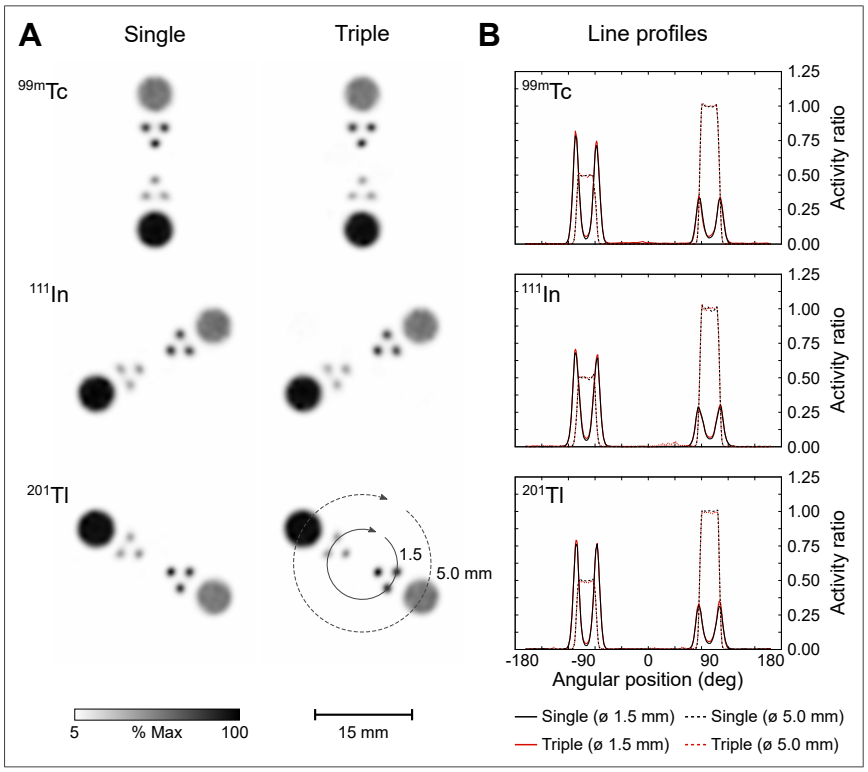

FIGURE 7. Modified small-animal Jaszczak phantom (A) and line profiles of spatially separated single- and multi-isotope mixtures (B). Multiple adjacent isotopes do not significantly affect image quality but slightly increase background noise.

spectrum at about 100 and 135 keV (Fig. 5A) indicated an initially high fraction of backscatter photons caused by shielding and electronic parts behind the scintillator. With increasing phantom size, this proportion was gradually overcome by forward scatter. The related energy shift to a lower mean photon energy increased the probability for photoelectric absorption in the collimator, and therefore, the tungsten x-ray fraction increased slightly from 5% to 8% (Fig. 5B). To correct attenuation, scatter, and x-ray fluorescence for single-isotope studies, it has been shown that simple calibration procedures with phantoms of appropriate diameter result in sufficient accuracies within 10% even for rat-sized objects (*11*). For multiple isotopes, though, scatter and x-ray fluorescence additionally caused significant spectral crosstalk between radionuclides (Table 3).

The proportion of this spectral crosstalk strongly depends on the radioisotope combination used (Table 3). As discussed before, the finite energy resolution hampered the separation of radioisotopes with close γ-energies, for example, ^{123}I/^{99m}Tc. In contrast, collimator x-ray fluorescence affected only particular isotopes in the range of 50–90 keV. ^{201}Tl image data, for instance, were slightly altered by x-ray fluorescence of tungsten at 67.6 keV (kα) and 58.8 keV (kβ). Moreover, theranostic radioisotopes such as ^{177}Lu are often challenging because they have low γ-branching ratios. They are prone to spectral crosstalk from other radioisotopes. They also emit electrons that generate a continuous spectrum of bremsstrahlung that intrude all isotopes with energies lower than the electron maximum kinetic energy (498.3 keV for ^{177}Lu). However, in this study, the measured crosstalk factors for 1-to-1 isotope combinations remained low compared with clinical SPECT. To improve quantitative accuracy, the NanoSPECT/CT^{PLUS} user guide proposes a first-order correction using crosstalk factors obtained with appropriate phantoms. It has been shown that quantitative accuracy was acceptable as long as the peak of the lower energy was predominant (*17,18*). However, the extent of crosstalk is a linear function of the radionuclide activity ratio (Eq. 16), and small deviations between calibration and experimental setup are amplified for varying ratios. Calibration factors also act globally and may not reflect local scatter variations.

To assess the image quality in multi-isotope experiments, spatially superimposed and adjacent activity distributions needed to be distinguished. Superimposed radioisotopes may interfere directly because spectral thresholding is the only mechanism for radioisotope separation. If activity distributions are spatially detached, they should be completely separable. However, a significant portion of spatial crosstalk can be introduced by multiplexed multi-pinhole collimation. Projections of several pinholes overlap and share detector surface to find a compromise between magnification and sensitivity. This provokes spatial ambiguities for single isotopes, which can be resolved with iterative reconstruction approaches (*13*). For multiple isotopes, double ambiguities are introduced, and SPECT systems need to tackle spatial and spectral uncertainties concurrently. To avoid multiplexing, single-pinhole collimators might be the best choice, if low count rate sensitivities are acceptable.

CONCLUSION

The intrinsic detector properties of the NanoSPECT/CT^{PLUS} were suitable for the simultaneous acquisition of up to 3 isotopes, with limitations for count rates exceeding 104 kcps and energies lower than 75 keV. Spectral crosstalk between isotopes was more likely mediated by hardware than by source scatter and was strongly dependent on the isotope combination. Simultaneous multi-isotope acquisitions slightly degraded spatial resolution and image uniformity for spatially superimposed but not for spatially separated activity distributions while background noise level was increased for all multi-isotope studies. For particular isotopes, collimator penetration and x-ray fluorescence contributed a significant portion of error.

We conclude that the NanoSPECT/CT^{PLUS} enables the simultaneous acquisition of 3 isotopes with high quantitative accuracy and only little loss of image quality when the activity ratio is adapted to isotope-specific count rate sensitivities and when the system calibration is performed with phantoms of appropriate size.

DISCLOSURE

This work was supported in part by the Technologiestiftung Berlin (TSB). Mathias Lukas is also employed by Siemens Healthcare GmbH. No other potential conflict of interest relevant to this article was reported.

ACKNOWLEDGMENTS

We thank Janet Francis Eary (National Cancer Institute) for careful revision of the manuscript.

KEY POINTS

QUESTION: What are the limits of multi-isotope imaging for the NanoSPECT/CT^{PLUS} and to what extent do hardware-related perturbations affect image quality and quantitative accuracy?

PERTINENT FINDINGS: The NanoSPECT/CT^{PLUS} enables the simultaneous acquisition of 3 isotopes with high quantitative accuracy and only little loss of image quality when the activity ratio is adapted to isotope-specific count rate sensitivities and when the system calibration is performed with phantoms of appropriate size.

IMPLICATIONS FOR PATIENT CARE: Preclinical multi-isotope SPECT reveals information about simultaneous pathophysiologic processes, increases economic efficiency of pharmaceutical drug development, and therefore accelerates the translation from bench to bedside.

REFERENCES

1. Meikle SR, Kench P, Kassiou M, Banati RB. Small animal SPECT and its place in the matrix of molecular imaging technologies. *Phys Med Biol.* 2005;50:R45–R61.
2. Martin EB, Williams A, Richey T, et al. Comparative evaluation of p5+14 with SAP and peptide p5 by dual-energy SPECT imaging of mice with AA amyloidosis. *Sci Rep.* 2016;6:22695.
3. Dresel SH, Kung MP, Huang XF, et al. Simultaneous SPECT studies of pre- and postsynaptic dopamine binding sites in baboons. *J Nucl Med.* 1999;40:660–666.
4. Xu B, Shokeen M, Sudlow GP, et al. Utilizing the multiradionuclide resolving power of SPECT and dual radiolabeled single molecules to assess treatment response of tumors. *Mol Imaging Biol.* 2015;17:671–679.
5. Hutton BF, Buvat I, Beekman FJ. Review and current status of SPECT scatter correction. *Phys Med Biol.* 2011;56:R85–R112.
6. Rault E, Staelens S, De Beenhouwer J, Van Holen R, Vandenberghe S. Accurate Monte Carlo modelling of the back compartments of SPECT cameras. *Phys Med Biol.* 2011;56:87–104.
7. Hwang AB, Franc BL, Gullberg GT, Hasegawa BH. Assessment of the sources of error affecting the quantitative accuracy of SPECT imaging in small animals. *Phys Med Biol.* 2008;53:2233–2252.
8. Schramm N, Hoppin J, Lackas C, Roelf FV, de Jong M. The NanoSPECT: a high-sensitivity multi-pinhole SPECT system with submillimeter (nanoliter) spatial resolution for imaging small rodents [abstract]. *J Nucl Med.* 2006;47(suppl):233P.
9. *NEMA Standards Publication NU 1-2012: Performance Measurements of Gamma Cameras.* Arlington, VA: National Electrical Manufacturers Association; 2012.

10. Deleye S, Van Holen R, Verhaeghe J, Vandenberghe S, Stroobants S, Staelens S. Performance evaluation of small-animal multipinhole μSPECT scanners for mouse imaging. *Eur J Nucl Med Mol Imaging.* 2013;40:744–758.
11. Lange C, Apostolova I, Lukas M, et al. Performance evaluation of stationary and semi-stationary acquisition with a non-stationary small animal multi-pinhole SPECT system. *Mol Imaging Biol.* 2014;16:311–316.
12. Payne SA, Cherepy NJ, Hull G, Valentine JD, Moses WW, Choong WS. Non-proportionality of scintillator detectors: theory and experiment. *IEEE Trans Nucl Sci.* 2009;56:2506–2512.
13. Islamian JP, Azazrm A, Mahmoudian B, Gharapapagh E. Advances in pinhole and multi-pinhole collimators for single photon emission computed tomography imaging. *World J Nucl Med.* 2015;14:3–9.
14. Silosky M, Johnson V, Beasley C, Kappadath SC. Characterization of the count rate performance of modern gamma cameras. *Med Phys.* 2013;40:032502.
15. Lecoq P. Development of new scintillators for medical applications. *Nucl Instruments Methods Phys.* 2016;809:130–139.
16. Diehl KH, Hull R, Morton D, et al. A good practice guide to the administration of substances and removal of blood, including routes and volumes. *J Appl Toxicol.* 2001;21:15–23.
17. Prior P, Timmins R, Petryk J, et al. A modified TEW approach to scatter correction for In-111 and Tc-99m dual-isotope small-animal SPECT. *Med Phys.* 2016;43:5503–5513.
18. Finucane CM, Murray I, Sosabowski JK, Foster JM, Mather SJ. Quantitative accuracy of low-count SPECT imaging in phantom and in vivo mouse studies. *Int J Mol Imaging.* 2011;2011:197381.

SUPPLEMENTAL TABLES

SUPPLEMENTAL TABLE 1
Geometric specifications for the nine-pinhole collimators of the NanoSPECT/CT^{PLUS} (in mm)

Aperture	NSP-106	NSP-116	NSP-105	NSP-125
Acronym	MH	MU	RH	RU
Hole Diameter	1.0	0.5	1.5	0.8
Thickness	10.0	10.0	10.0	10.0
FOV Axial	14.0	14.0	22.0	22.0
FOV Transaxial	30.0	16.0	60.0	30.0
Distance Central Axis	30.0	30.0	45.0	45.0
Distance Detector	145.0	145.0	130.0	130.0

Collimator: MH/MU Mouse high/ultra-high resolution, *RH/RU* rat high/ultra-high resolution

SUPPLEMENTAL TABLE 2
Energy windows used for single and multi-isotope studies (peak in keV, width in %).

	Energy window 1		Energy window 2		Energy window 3		Energy window 4	
Single-Isotope	Peak	Width	Peak	Width	Peak	Width	Peak	Width
^{99m}Tc	140.5	20	—	—	—	—	—	—
^{111}In	171.3	20	245.4	20	—	—	—	—
^{123}I	159.0	20	—	—	—	—	—	—
^{177}Lu	56.1	20	112.9	20	208.4	20	—	—
^{201}Tl	72.3	20	167.4	20	—	—	—	—
Dual-Isotope								
^{99m}Tc* + ^{111}In**	*140.5	15	**171.3	15	**245.4	20	—	—
^{99m}Tc* + ^{123}I**	*140.5	10	**159.0	10	—	—	—	—
^{99m}Tc* + ^{177}Lu**	**56.1	20	**112.9	20	*140.5	20	**208.4	20
^{99m}Tc* + ^{201}Tl**	**72.3	20	*140.5	20	**167.4	15	—	—
^{111}In* + ^{201}Tl**	**72.3	20	*245.4	20	—	—	—	—
^{111}In* + ^{177}Lu**	**112.9	20	*171.3	20	**208.4	15	*245.4	15
^{123}I* + ^{177}Lu**	**56.1	20	**112.9	20	*159.0	20	**208.4	20
^{123}I* + ^{201}Tl**	**72.3	20	*159.0	20	—	—	—	—
Triple-Isotope								
^{99m}Tc* + ^{111}In** + ^{201}Tl***	***72.3	20	*140.5	15	**171.3	15	**245.4	20
^{99m}Tc* + ^{111}In** + ^{177}Lu***	***112.9	20	*140.5	20	***208.4	15	**245.4	15
^{99m}Tc* + ^{123}I** + ^{177}Lu***	***112.9	20	*140.5	10	**159.0	10	***208.4	20
^{99m}Tc* + ^{123}I** + ^{201}Tl***	***72.3	20	*140.5	10	**159.0	10	—	—

$^{*/**/***}$ *Ordinal signs to ascribe the energies to their isotope*

SUPPLEMENTAL FIGURES

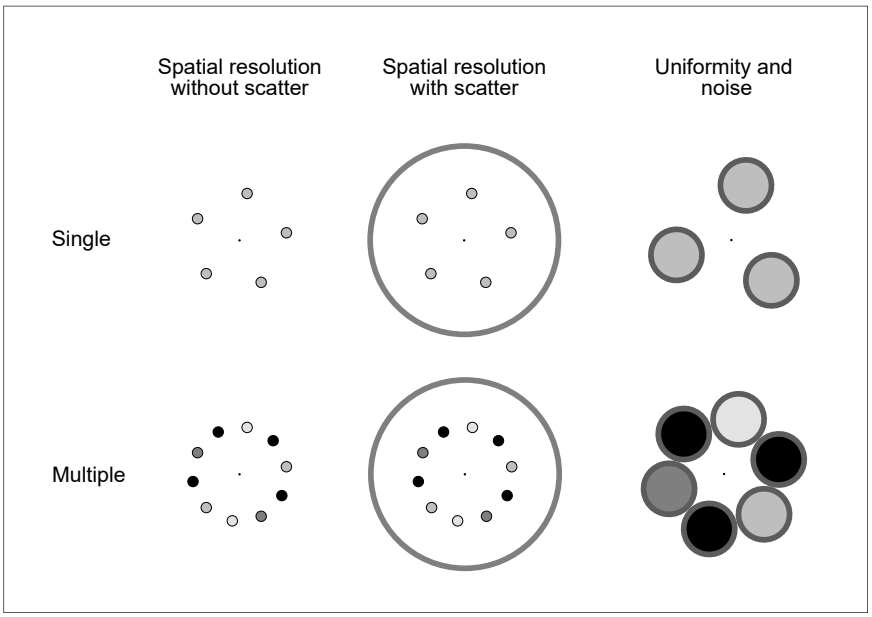

SUPPLEMENTAL FIGURE 1. Schematic geometry for the measurement of spatial resolution, uniformity and noise. Each isotope was measured separately (Single) and together with a mixture of two or three isotopes (Multiple) to represent adjacent and superimposed activity distributions (air/water: white, single-isotope: gray, triple-isotope: black).

Original Publication | Monte Carlo Simulations

Journal Summary List

Lukas M, Kluge A, Beindorff N, Brenner W. Accurate Monte Carlo Modeling of Small-Animal Multi-Pinhole SPECT for Non-Standard Multi-Isotope Applications. *IEEE Trans Med Imaging.* 2021 Sep; 40:2208-2220.

Journal Data Filtered By: **Selected JCR Year: 2021** Selected Editions: SCIE,SSCI
Selected Categories: **"RADIOLOGY, NUCLEAR MEDICINE and MEDICAL IMAGING"**
Selected Category Scheme: WoS
Gesamtanzahl: 136 Journale

Rank	Full Journal Title	Total Cites	Journal Impact Factor	Eigenfactor Score
1	RADIOLOGY	76,068	29.146	0.06701
2	JACC-Cardiovascular Imaging	17,107	16.051	0.03685
3	MEDICAL IMAGE ANALYSIS	16,080	13.828	0.01971
4	JOURNAL OF NUCLEAR MEDICINE	35,215	11.082	0.02946
5	**IEEE TRANSACTIONS ON MEDICAL IMAGING**	**32,367**	**11.037**	**0.03385**
6	CLINICAL NUCLEAR MEDICINE	6,843	10.782	0.00604
7	INVESTIGATIVE RADIOLOGY	8,071	10.065	0.00778
8	EUROPEAN JOURNAL OF NUCLEAR MEDICINE AND MOLECULAR IMAGING	24,002	10.057	0.02525
9	Photoacoustics	1,827	9.656	0.00293
10	European Heart Journal - Cardiovascular Imaging	10,941	9.130	0.01865
11	ULTRASOUND IN OBSTETRICS & GYNECOLOGY	19,564	8.678	0.01922
12	Circulation-Cardiovascular Imaging	8,707	8.589	0.01482
13	INTERNATIONAL JOURNAL OF RADIATION ONCOLOGY	53,680	8.013	0.03572
14	COMPUTERIZED MEDICAL IMAGING AND GRAPHICS	3,973	7.422	0.00342
15	NEUROIMAGE	131,266	7.400	0.10055
16	Diagnostic and Interventional Imaging	3,132	7.242	0.00353
17	Zeitschrift für Medizinische Physik	1,002	7.215	0.00146
18	KOREAN JOURNAL OF RADIOLOGY	5,788	7.109	0.00711
19	Physical and Engineering Sciences in Medicine	862	7.099	0.00114
20	EUROPEAN RADIOLOGY	35,461	7.034	0.04482
…				
136	Iranian Journal of Radiology	469	0.399	0.00042

Accurate Monte Carlo Modeling of Small-Animal Multi-Pinhole SPECT for Non-Standard Multi-Isotope Applications

Mathias Lukas, Anne Kluge, Nicola Beindorff, Winfried Brenner

***Abstract*—Recent advances in preclinical SPECT instrumentation enable non-standard multi-isotope acquisitions at the edge of physical feasibility to improve efficiency of pharmaceutical research. Due to the variety of applications, optimization of imaging hardware, acquisition protocols and reconstruction algorithms is a central and recurring task. For this purpose, we developed a Monte Carlo simulation model of a preclinical state-of-the-art multi-pinhole SPECT system, the NanoSPECT/CT^{PLUS}, with emphasis on high accuracy for multi-isotope experiments operating near the system range limits. The GATE/GEANT4 model included an accurate description of multi-pinhole collimators and all substructures of the detector back compartment. The readout electronics was modeled with a variety of signal processors partially extended to incorporate non-simplified measured response functions. The final model was able to predict energy spectra, planar images and tomographic reconstructions with high accuracy for both standard and non-standard multi-isotope experiments. Complex activity distributions could be reproduced for a wide range of noise levels and different modes of angular undersampling. Using the example of a dual-isotope triple-tracer experiment, the model has proven to be a powerful tool for protocol optimization and quantitative image correction at the performance range limits of multi-isotope multi-pinhole SPECT.**

***Index Terms*—Monte Carlo Simulation, Multi-Isotope, Multi-Pinhole, SPECT, GATE/GEANT4**

I. INTRODUCTION

SMALL animal single photon emission computed tomography (SPECT) has become an integral part of translational medicine. It is a powerful tool for validating drug targeting, safety, and efficacy at reasonable cost [1].

However, the technical demand on preclinical SPECT is high. Imaging objects are small and physiological processes are faster compared to clinical studies. Small injection volumes, low count rates as well as a large variety of radioisotopes need to be handled while data acquisition should be fast, sensitive and quantitative at once. Non-standard protocols with angular undersampling, non-conventional isotopes or multiple tracers are increasingly used to improve economic efficiency of pharmaceutical research. For these applications, preclinical SPECT frequently works at the edge of technical feasibility and the optimization of imaging hardware, acquisition protocols and reconstruction algorithms is a central and recurring task.

Monte Carlo simulations are widely used for such optimization procedures [2], [3]. The mathematical techniques used by this method are based on repeated random variable sampling. For this reason, they are well suited for solving problems related to statistical processes such as the stochastic nature of radioactivity and particle transport through matter. They are also based on first principles of physics and can be used to address a variety of problems that are difficult to study by experimental or analytical approaches.

Numerous open source Monte Carlo toolkits are available, each with individual strengths and limitations [2]. GEANT4, one of the most powerful all-purpose C++ code compilations for particle transport, covers a wide range of physical phenomena including electromagnetic, hadronic and optical processes within the energy range of 250 eV to 1 PeV [4]. A large set of subatomic particles, elements and materials along with a simplified geometry description framework facilitates the simulation of complex experimental setups with high accuracy. GATE, a C++ code extension for GEANT4, adds dedicated features for medical imaging applications and provides modules to imitate unideal signal formation of real radiation detectors [5]. Spatial, spectral and temporal blurring, energy discrimination, dead time, pileup, transfer rate limitations and other signal-processing related phenomena can be modeled as well as time-dependent processes such as detector movement or respiratory motion. Thus, tomographic imaging devices and imaging subjects can be virtualized in their entirety with high accuracy.

These advanced modeling capabilities are especially valuable for small animal multi-isotope SPECT. Since complex setups and limiting conditions are not unusual, inconspicuous effects can gain importance and need to be considered [6]. Single-pinhole collimators, small injection volumes and prototype tracers with low specific activities, for instance, can lead to low count rates just above system detectability [7]. Under these conditions, electronics dark currents or ^{210}Pb contamination of the radiation shielding cause substantial noise levels with energy-dependent and inhomogeneous spatial distributions. In contrast, simultaneous multi-isotope studies

Manuscript received January 10, 2021; revised March 14, 2021; accepted April 10, 2021. published April 14, 2021; printed September 10, 2021. *(Corresponding author: Mathias Lukas)*

M. Lukas is with the Department of Nuclear Medicine, Charité - Universitätsmedizin Berlin, 13353 Berlin, Germany, and also with Siemens Healthcare GmbH, 13629 Berlin, Germany (e-mail: mathias.lukas@charite.de).

A. Kluge is with the Department of Radiation Oncology and Radiotherapy, Charité - Universitätsmedizin Berlin, 13353 Berlin, Germany.

N. Beindorff is with the Berlin Experimental Radionuclide Imaging Center (BERIC), Charité - Universitätsmedizin Berlin, 13353 Berlin, Germany.

W. Brenner is with the Department of Nuclear Medicine, Charité - Universitätsmedizin Berlin, 13353 Berlin, Germany.

Digital Object Identifier 10.1109/TMI.2021.3073749

with multi-pinhole collimators increase count rates and system noise perturbations are usually replaced by dead-time effects [8]. Other sources of error include collimator penetration and x-ray fluorescence, which turned out to be perturbing effects most notably for preclinical multi-isotope studies [8], [9]. However, accurate modeling of these effects is possible, albeit computationally expensive, and substantially increases spectral and spatial accuracy of limiting case investigations.

Few studies on multi-pinhole SPECT modeling have been published so far. Mok *et al.*, for instance, developed a Monte Carlo model based on the small animal dual-head SPECT/CT system X-SPECT using MCNP and SimSET [10]. Chen *et al.* modeled the same system with a combination of SimSET and GATE [11] and the trimodal imaging system Inveon has been modeled by Lee *et al.* [12]. However, describing the entire signal processing chain has been given a low priority as simplified signal processing still provides sufficient results for single isotope imaging under normal conditions.

In this work, we developed a Monte Carlo model of the NanoSPECT/CT$^{\text{PLUS}}$ with emphasis on high accuracy for multi-isotope experiments operating near the system range limits. In addition, an easy-to-use software toolkit for simulation, data conversion and quantitative image reconstruction was established. This framework can be used for cost-effective optimization of imaging hardware, acquisition procedures and reconstruction algorithms that enables pioneering imaging protocols at the edge of SPECT system technological feasibility.

II. SYSTEM DESCRIPTION

The NanoSPECT/CT$^{\text{PLUS}}$ (Mediso, Hungary) is a dedicated small animal SPECT/CT system that can be configured with up to four detector heads (Fig. 1, Suppl. Fig. 1). Imaging collimation is achieved either by parallel-hole or by combined pyramid-pinhole collimators with bore opening sizes of 250 mm or 60-80 mm, respectively. Especially for rodent imaging, multi-pinhole collimation is preferred as it combines high spatial resolution of pinhole magnification with high count rate sensitivity.

Numerous multi-pinhole collimators are available for the SPECT system. They all differ in pinhole geometry and field of view (FOV). Each hole of a multi-pinhole collimator is drilled in a different axial and transaxial direction and therefore defines an individual three-dimensional projective view (Fig. 2). These projective views are multiplexed at the detector plane, which maximizes object magnification, spatial resolution and count rate sensitivity for a given detector surface. Multiplexing introduces spatial ambiguities that need to be addressed by iterative reconstruction algorithms.

The four detector heads and multi-pinhole collimation of the NanoSPECT/CT$^{\text{PLUS}}$ enables stationary and semi-stationary acquisition schemes for high temporal resolution [13]. In conventional non-stationary SPECT, the detectors need to rotate around the imaging object for angular sampling ($\geq$108 pinhole projections per time frame). Differently angulated pinholes of a multi-pinhole collimator, though, provide sufficient data for three-dimensional reconstruction without detector movement

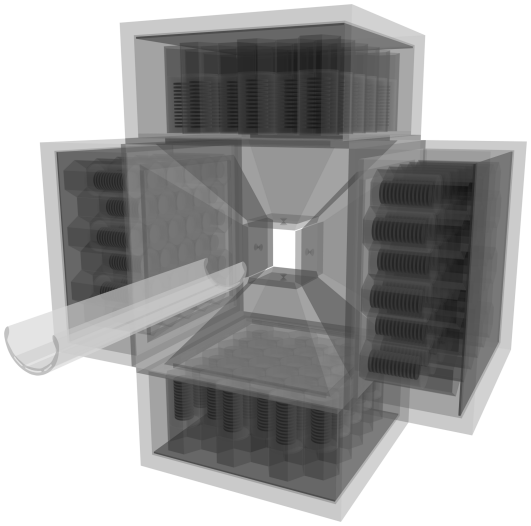

Fig. 1. Geometric model of the NanoSPECT/CT$^{\text{PLUS}}$ used for Monte Carlo simulations.

(36 pinhole projections per time frame). The semi-stationary acquisition mode combines angular sampling of multi-pinhole collimators with a two-step pendular gantry movement (72 pinhole projections per time frame), which is a good compromise between angular integrity and temporal resolution [13].

The NanoSPECT/CT$^{\text{PLUS}}$ also provides capabilities to acquire four isotopes simultaneously. It is delivered with the software HiSPECT (Scivis GmbH, Germany), an ordered subsets-expectation maximization (OSEM) algorithm for iterative SPECT image reconstruction.

III. MONTE CARLO MODEL DEVELOPMENT

A. Environment

The NanoSPECT/CT$^{\text{PLUS}}$ was modeled with GATE v8.1.p01 [5] compiled with GEANT4 v4.10.04.p02 [4], and ROOT v6.14.06 [14]. The simulations were executed on a Debian-based Linux operating system with two Intel i7 4770 CPUs (64 bit, 3.4 GHz, 2×4 cores, 2×8 threads). The simulation time for 1 second of $^{99\text{m}}$Tc, ^{111}In, ^{123}I and ^{201}Tl point source emission in air was 47, 23, 28, and 24 s/MBq, respectively. Data conversion and data analysis was performed using Matlab 9.3.0 (The MathWorks, Inc., United States).

B. Physics

Electromagnetic processes of the GEANT4 physics list *emstandard_opt3* were used including photoelectric effect, Compton and Rayleigh scattering, multiple scattering, bremsstrahlung, ionization, x-ray fluorescence, particle induced x-ray emission, auger electron emission, and radioactive decay. For highest spectral accuracy, radioactive sources were defined as excited state ion sources with isotropic emission distribution. In all simulations, γ-rays and charged particles were tracked through the objects until their energy fell below 1 keV (cut-off energy).

TABLE I
GEOMETRIC SPECIFICATIONS OF PINHOLE COLLIMATORS (IN MILLIMETER)

Aperture	**115**	**105**
Acronym	SP	MP
Hole diameter	1.5	1.5
Thickness	10.0	10.0
FOV axial	40.0	22.0
FOV transaxial	40.0	60.0
Distance central axis	45.0	45.0
Distance detector	130.0	130.0

SP Single-pinhole collimator, *MP* Multi-pinhole collimator

C. Geometry

The geometric model of the NanoSPECT/CT$^{\text{PLUS}}$ comprised an accurate description of gantry, detector heads, pyramid collimators, pinhole collimators and subject table (Fig. 1, Suppl. Fig. 1). Conceptual drawings depicting all considered components are shown in Fig. 2.

The SPECT gantry consists of four detector heads, each equipped with a thallium doped sodium iodide scintillation crystal (NaI(Tl), $262 \times 255 \times 6.35\,\text{mm}^3$, $3.7\,\text{g/cm}^3$) covered by protection layers made of plastic (1 mm, $1.18\,\text{g/cm}^3$) and aluminum (1 mm, $2.7\,\text{g/cm}^3$). Each crystal is coupled via a glass light guide ($310 \times 310 \times 6.35\,\text{mm}^3$, $2.5\,\text{g/cm}^3$) to 33 position-sensitive 2″ diameter photomultiplier tubes (PMT). These PMTs were modeled according to the Hamamatsu R6231-01, a cylindrically shaped air-evacuated glass tube PMT (⌀51 mm × 80 mm, 1 mm glass housing, $2.5\,\text{g/cm}^3$). Due to the difficulty of simulating the complex geometry of the focusing electrode and the dynodes, these parts were approximated with 13 equally spaced electronic boards (⌀30 mm, 2.5 mm) [15]. The PMTs are connected to a back-end circuit board ($310 \times 310 \times 5\,\text{mm}^3$) and are embedded in a hexagonal mu-metal grid for electromagnetic shielding (wall thickness 1 mm). The material of the electronic boards was approximated with a material composed of 75% plexiglass, 5% copper and 20% iron, with a mass density of $1.2\,\text{g/cm}^3$. Mu-metal was approximated by a composition of 77% nickel, 16% iron, 5% copper and 2% chromium, with a mass density of $8.7\,\text{g/cm}^3$. Finally, a leaden layer shrouded the detector for radiation shielding (15 mm, $11.4\,\text{g/cm}^3$).

Imaging collimation was achieved by pinhole collimators (HPM1850 tungsten, $18.5\,\text{g/cm}^3$) mounted on top of pyramid shielding (lead, $11.4\,\text{g/cm}^3$). For this study, the single-pinhole (SP) collimator APT-115 and the multi-pinhole (MP) collimator APT-105 were simulated, both intended for rodent imaging. Their geometric specifications are summarized in Table I. Pinhole locations, angulations and acceptance angles of SP and MP collimators were determined using a set of $^{99\text{m}}$Tc point source measurements and trigonometric calculations [16].

D. Signal Processing

The readout electronics of the NanoSPECT/CT$^{\text{PLUS}}$ were modeled using a sequence of GATE Digitizer modules as shown in Fig. 3. The GEANT4 *Hits* module generates visible

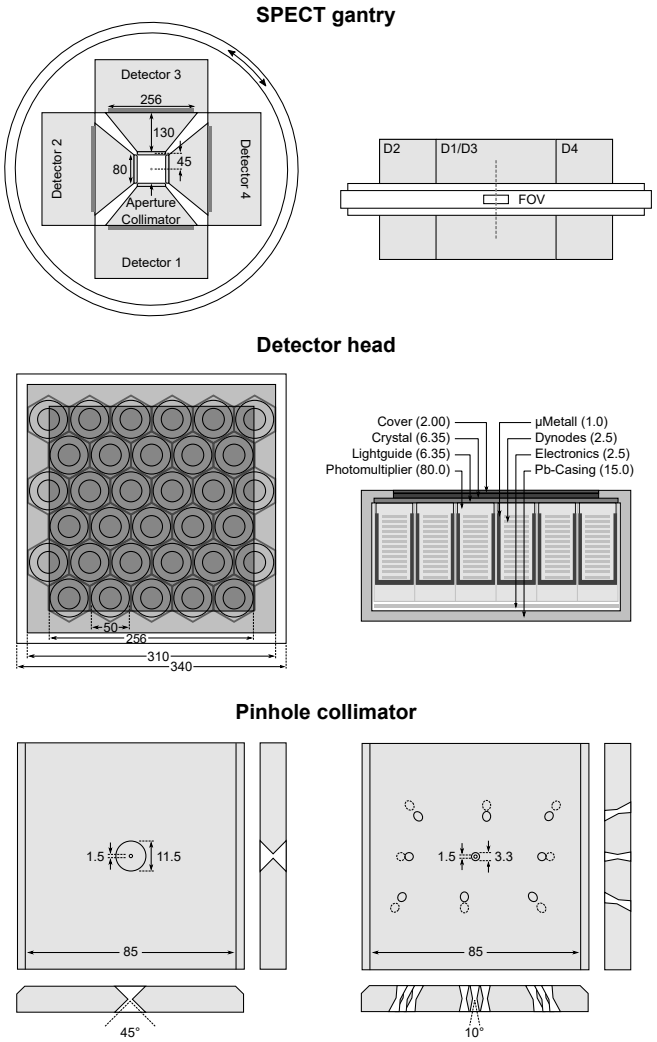

Fig. 2. Geometric dimensions of the NanoSPECT/CT$^{\text{PLUS}}$ gantry, detector head, and pinhole collimators used for Monte Carlo simulation (in millimeter).

photons (hits) from interactions of γ-rays with the NaI(Tl) crystals. The *Adder* module integrates all hits that occur within the same crystal and generates a valid pulse with the integral energy E_ν and the energy-weighted centroid coordinate $P(x, y)$. To mimic signal losses due to limited photon transfer efficiency, PMT quantum efficiency and scintillator light yield inhomogeneity, the *Efficiency* module randomly rejects 29.4% of all valid pulses. The *Pileup* module emulates the finite time resolution of the detection system that arises from scintillation decay and limited readout frequency. The dead time τ for each crystal was set to 490 ns according to [8].

The scintillation process, optical photon transport and light detection were not simulated in this study. To account for these effects, spatial position $P(x, y)$ and energy E_ν of the detected photons were blurred with measured response functions given by [8]. Therefore, the *Spatial resolution* module applies a two-dimensional Gaussian kernel with 3.0 mm full width at half maximum (FWHM) to the coordinate of interaction $P(x, y)$. This leads to isotope-specific spatial resolutions due to energy dependent depth-of-interaction effects (e.g. 3.2 mm FWHM

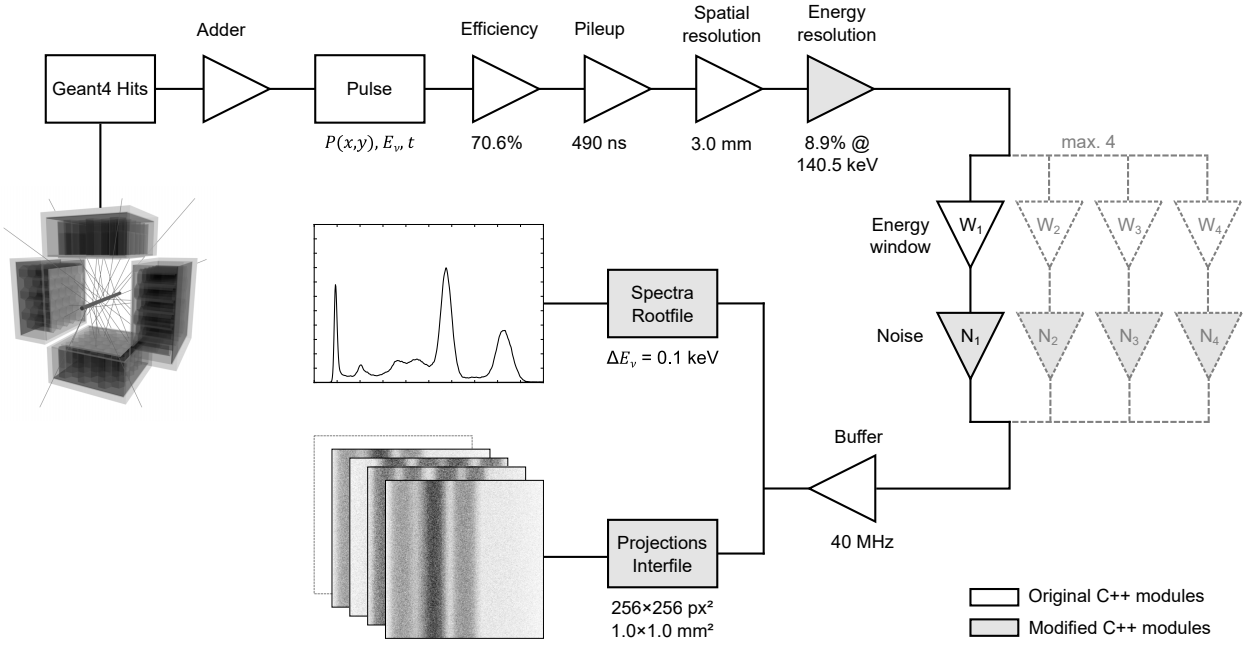

Fig. 3. Signal processing model of the NanoSPECT/CT$^{\text{PLUS}}$ readout electronics used for Monte Carlo simulation. The GATE modules *Energy Resolution* and *Noise* were extended to incorporate measured non-analytical response functions for improved accuracy at the performance range limits.

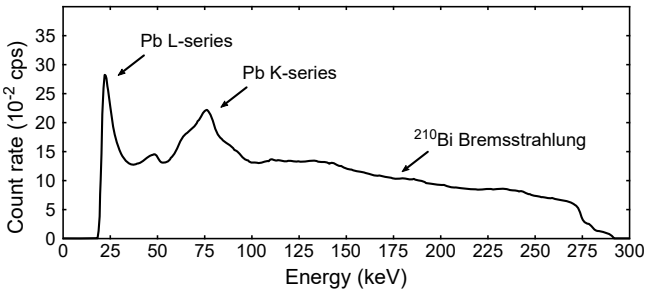

Fig. 4. Dark spectrum of the NanoSPECT/CT$^{\text{PLUS}}$ acquired for 10 hours. The dark count rate is predominantly caused by ^{210}Pb contamination of the radiation shielding. Its β^- decay product ^{210}Bi emits high-energy β^- radiation, which induces bremsstrahlung and Pb x-ray fluorescence (L/K-series). These data were used as input for the modified GATE *Noise* module to improve accuracy of ultra-low count rate simulations.

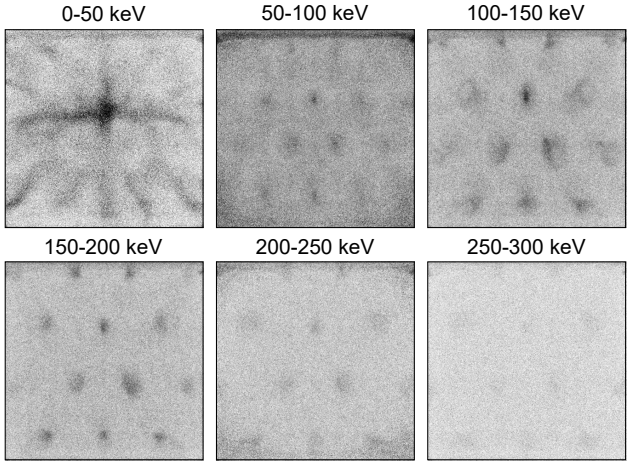

Fig. 5. Dark image of the NanoSPECT/CT$^{\text{PLUS}}$ acquired for 10 hours. The ^{210}Pb perturbation was most prominent close to the lead septum separating SPECT and CT gantries (upper edge). With increasing energy, the absolute count rate was 3.7 ± 1.0, 10.5 ± 0.9, 8.1 ± 0.6, 7.1 ± 0.5, 6.3 ± 0.6, and 4.3 ± 0.3 cps, respectively. These data were used as input for the modified GATE *Noise* module to improve accuracy for ultra-low count rate simulations.

on average for $^{99\text{m}}$Tc). For energy blurring, the C++ code of the *Energy resolution* module was extended by the energy response function R_{FWHM} given in [8]:

$$R_{FWHM}(E_\nu) = 8.56 + 56.87\, e^{-0.0589 E_\nu} \quad [\%] \tag{1}$$

$$E_{FWHM}(E_\nu) = R_{FWHM}(E_\nu)\; E_\nu \quad [keV] \tag{2}$$

The energy E_ν of the incident pulses is blurred by a Gaussian distribution with FWHM E_{FWHM}. Subsequently, pulses are sorted into isotope specific *Energy window* modules (max. 4 for the NanoSPECT/CT$^{\text{PLUS}}$), which then are populated with energy-window-specific spatial and spectral noise. Therefore, the C++ code of the *Noise* module was reprogrammed to randomly add counts from a pool of measured dark rate acquisitions. The measured dark spectra and dark images used are shown in Fig. 4 and Fig. 5, respectively. Finally, signal flow effects such as electronics bandwidth and disk transfer limitations were considered with a 40 MHz *Buffer* module. The data are saved to ROOT files from which energy spectra and tomographic projections can be extracted to Interfile format. The Interfiles were converted to a specific data format that can be reconstructed with HiSPECT.

IV. Monte Carlo Model Validation

In order to assess the accuracy of the simulation model, different measurements and the corresponding simulations were performed. Prior to the measurements, the SPECT system was calibrated according to the manufacturer's instructions, which included calibrations for energy, linearity, uniformity, center of rotation and collimator offset.

A. Energy Spectra

A cylinder phantom was consecutively filled with ^{99m}Tc, ^{111}In, ^{123}I or ^{201}Tl ($\varnothing$10 mm $\times$ 20 mm, $\sim$1 MBq) and was placed in the gantry isocenter. Energy spectra were sampled/simulated for at least 10^5 counts using equidistant, energy range adapted channel widths (0.2-0.7 keV/channel) and MP collimators. ^{99m}Tc and ^{111}In were also measured/simulated as point sources in air ($\varnothing$1 mm, $\sim$100 kBq) with and without MP collimators in order to verify pyramid shielding composition and its impact on collimator x-ray fluorescence. Photopeak fractions F_{PP} were extracted for all multi-isotope combinations using the following equation:

$$F_{PP} = \int_{w_A} \dot{N}_B(E)dE \Big/ \int_{w_B} \dot{N}_B(E)dE \tag{3}$$

Here, w_A and w_B are the energy windows for isotope A and B, respectively. $\dot{N}_B(E)$ denotes the count rate of isotope B that depends on energy E.

B. Count Rate Performance

A 2-fold serial dilution of ^{99m}Tc with activities from 25 MBq to 0.2 kBq was prepared and centered in the FOV. Planar images were acquired/simulated for 30 s without collimators using 4 energy windows: 40 keV $\pm$ 50%, 120 keV $\pm$ 50%, 360 keV $\pm$ 50%, and 900 keV $\pm$ 40%. The sum of counts for all detector heads was extracted. To analyze the count pileup fraction, the count rate of the energy window 360 keV $\pm$ 50% was related to the total count rate, since it includes the double- and triple-piled ^{99m}Tc photopeaks at 281.0 and 421.5 keV.

C. System Sensitivity

Point sources ($\varnothing$1 mm) with $\sim$10 MBq ^{99m}Tc, ^{111}In, ^{123}I or ^{201}Tl were measured/simulated at different positions in the FOV using SP and MP collimators. Energy spectra were sampled/simulated and count rate sensitivities were extracted for all energy windows listed in Table II. The absolute activity in each sample was measured with a certified dose calibrator ISOMED 2010 (MED Dresden GmbH, Germany).

TABLE II
Energy windows used for image acquisition (peak in keV width in %)

	Window 1		Window 2	
Isotope	**Peak**	**Width**	**Peak**	**Width**
^{99m}Tc	140.5	20	-	-
^{111}In	171.3	20	245.4	20
^{123}I	159.0	20	-	-
^{201}Tl	72.3	20	167.4	20

D. Spatial Resolution

The intrinsic spatial resolution was measured/simulated using a lead slit plate (1 mm slit width, 4 mm plate thickness) and a ^{99m}Tc flood source (40 mm source thickness, 12 mm plastic casing) covering the detector head. The mean intrinsic spatial resolution $\bar{R}_i$ was determined using the following equations:

$$N(x) = \sum_y N(x, y) \tag{4}$$

$$N(x) = \sum_n N_{max,n}(x) \cdot e^{-4\ln(2)\left(\frac{x - x_{0,n}}{\Delta x_n}\right)^2} \tag{5}$$

$$\bar{R}_i = \frac{1}{n} \sum_n \Delta x_n \tag{6}$$

The acquired/simulated planar image $N(x, y)$ was integrated in slit direction to derive the line spread function $N(x)$. This profile was fitted to a sum of Gaussian like equations with maximum intensities $N_{max,n}(x)$ and spatial peak position $x_{0,n}$ to calculate the FWHM Δx_n for n slits. $\bar{R}_i$ was corrected for slit width W_s using the following equation:

$$R_{i,c} = \sqrt{\bar{R_i}^2 - {W_s}^2} \tag{7}$$

To determine the reconstructed spatial resolution, ^{99m}Tc point sources ($\varnothing$1 mm, $\sim$10 MBq) were measured/simulated in air at different transaxial and axial positions in the FOV using SP and MP collimators. SPECT images were acquired/simulated for 60 s using energy windows according to Table II (12 angular projections, 256×256 px^2, 1.0×1.0 mm^2/px^2). Tomographic images were reconstructed using HiSPECT ($0.4 \times 0.4 \times 0.4$ mm^3, 3×3 iterations, 25% Gaussian smoothing). The spatial resolution at each position was determined by computing the mean FWHM of the resulting point spread function image obtained by interpolation between adjacent pixels in radial, tangential and axial profiles.

E. Image Quality

For evaluation of the complete simulation model (geometry, signal processing, format conversion, reconstruction), a micro Jaszczak phantom ($\varnothing$25 mm) with 6 fields of rods

(⌀1.0-1.5 mm) was filled with ^{99m}Tc (~50 MBq/ml). SPECT was acquired/simulated after 0, 6 and 12 hours of decay to vary count statistics and dark rate impact ($100{\cdot}10^6$, $50{\cdot}10^6$, $25{\cdot}10^6$ counts, 40 angular projections, $256 \times 256\,\text{px}^2$, $1.0 \times 1.0\,\text{mm}^2/\text{px}^2$).

Additionally, a cylinder phantom (⌀28 mm) was filled with ^{99m}Tc (~10 MBq/ml) in order to compare uniformity and noise of different angular undersampled acquisition modes provided by the NanoSPECT/CT^{PLUS} (stationary/semi-stationary/fast-helical mode with 4/8/12 angular projections). These measurements/simulations were acquired with a constant count statistic of $25{\cdot}10^6$ counts for SP and MP collimators. Tomographic images were reconstructed using HiSPECT ($0.4 \times 0.4 \times 0.4\,\text{mm}^3$, 3×3 iterations, 25% Gaussian smoothing).

The reconstructed spatial resolution R_r was calculated from the micro Jaszczak phantom using three-dimensional derivations of Equation 4 to 7. The uniformity coefficient UC and the noise coefficients NC were calculated from cylinder phantom using:

$$UC = \frac{A_{max} - A_{min}}{A_{max} + A_{min}} \tag{8}$$

$$NC = \frac{\sigma_A}{m_A} \tag{9}$$

Here, A_{min} denotes the the minimum, A_{max} the maximum, m_A the mean and σ_A the standard deviation of the spatial activity distribution A.

F. Image Quantification

The quantitative accuracy of single-, dual- and triple-isotope simulations was assessed by a phantom experiment with 7 circularly arranged cylinder sources (⌀10 mm) filled with different mixtures of ^{99m}Tc (isotope A, 10.0 MBq/ml), ^{123}I (isotope B, 13.5 MBq/ml) and ^{201}Tl (isotope C, 15.0 MBq/ml). The amount of activity for each isotope was sensitivity adjusted to get equivalent count rate contribution. Multi-isotope SPECT images were acquired/simulated for 30 s using MP collimators and energy windows according to Table II (40 angular projections, $256 \times 256\,\text{px}^2$, $1 \times 1\,\text{mm}^2$). Tomographic images were reconstructed for each isotope using HiSPECT ($0.4 \times 0.4 \times 0.4\,\text{mm}^3$, 3×3 iterations, 25% Gaussian smoothing). Quantitative activity values were extracted for each isotope and cylinder source.

Additionally, planar images of attenuation, self-scatter and spectral crosstalk were extracted from simulated data for component analyses and model-based correction of measured data. For each detector angulation θ, these images were normalized to the total number of photons simulated and were smoothed using a Gaussian kernel with $2 \times 2\,\text{mm}^2$. Finally, the simulated planar fraction images for attenuation $p_a(x, y, \theta)$, self-scatter $p_s(x, y, \theta)$ and crosstalk $p_c(x, y, \theta)$ were multiplied by the uncorrected measured planar images $p_{mu}(x, y, \theta)$ in order to obtain corrected images $p_{mc}(x, y, \theta)$ for re-reconstruction:

$$p_{mc} = p_{mu} \cdot p_a \cdot p_s \cdot p_c \tag{10}$$

V. Monte Carlo Model Application

Multi-isotope imaging enables the simultaneous characterization of different physiological and pathological pathways and their mutual interactions down to the picomolar range. It has been used successfully for comparative studies [17], competing studies [18], and dose-response assessment in therapeutic applications [19]. However, imaging multiple isotopes simultaneously introduces a number of physical interferences that hamper image quality and quantification accuracy. Monte Carlo simulations can help improving quality of acquired primary and reconstructed secondary data.

As an example of application, the Monte Carlo model devoloped in this study was used to optimize the imaging protocol of a dual-isotope triple-tracer experiment in silico. The radiotracers ^{123}I-NaI, ^{99m}Tc-$NaTcO_4$ and ^{99m}Tc-MDP were intended to be imaged in a single mouse with lowest tracer amount possible without losing kinetic information for late pharmakokinetic clearance. After optimization and translation to an in-vivo experiment, the Monte Carlo model was used to estimate attenuation, self-scatter and spectrospatial crosstalk to improve image quality and quantitative accuracy of the measured data. This investigation was part of a 3*R* initiative that aimed to replace, reduce and refine animal experiments in pharmaceutical research by establishing species- and tracer-specific normal databases with minimum number of laboratory animals.

A. In Silico - Protocol Optimization

A computed tomography scan of a mouse (C57BL/6) was segmented into bone, soft and lung tissue compartments to obtain a three-dimensional attenuation model. For the radioactive source distribution model, bone, thyroid and salivary glands were segmented and provided with tracer-specific pharmakokinetic data from literature (Suppl. Table 1) [20], [21]. The resultant four-dimensional model was simulated (40 angular projections) and reconstructed repeatedly ($0.4 \times 0.4 \times 0.4\,\text{mm}^3$, 3×3 iterations, 25% Gaussian smoothing) in order to estimate optimum hardware settings, energy windows, activity ratios and injection timing.

Collimators: Four 9-pinhole collimator sets with different specifications (Table V) were simulated to find the best trade-off between effective FOV, spatial resolution, count rate sensitivity, septum penetration and multiplexing for the given mouse geometry. Count rate sensitivity, collimator penetration and percentage of multiplexing were extracted from simulated spectrospatial data. Spatial resolution was calculated from reconstructed images using spatial deconvolution and thyroid as sphere source with known diameter. Partial volume effects were calculated as the ratio of simulated to reconstructed counts in thyroid (⌀1.5 mm) and salivary gland (⌀5.0 mm).

Energy windows: The energy window width for ^{99m}Tc and ^{123}I were varied from 1% to 40% to find the best trade-off between count rate sensitivity and count rate perturbations (self scatter, cross scatter, hardware scatter and x-ray fluorescence). The optimum energy window w was

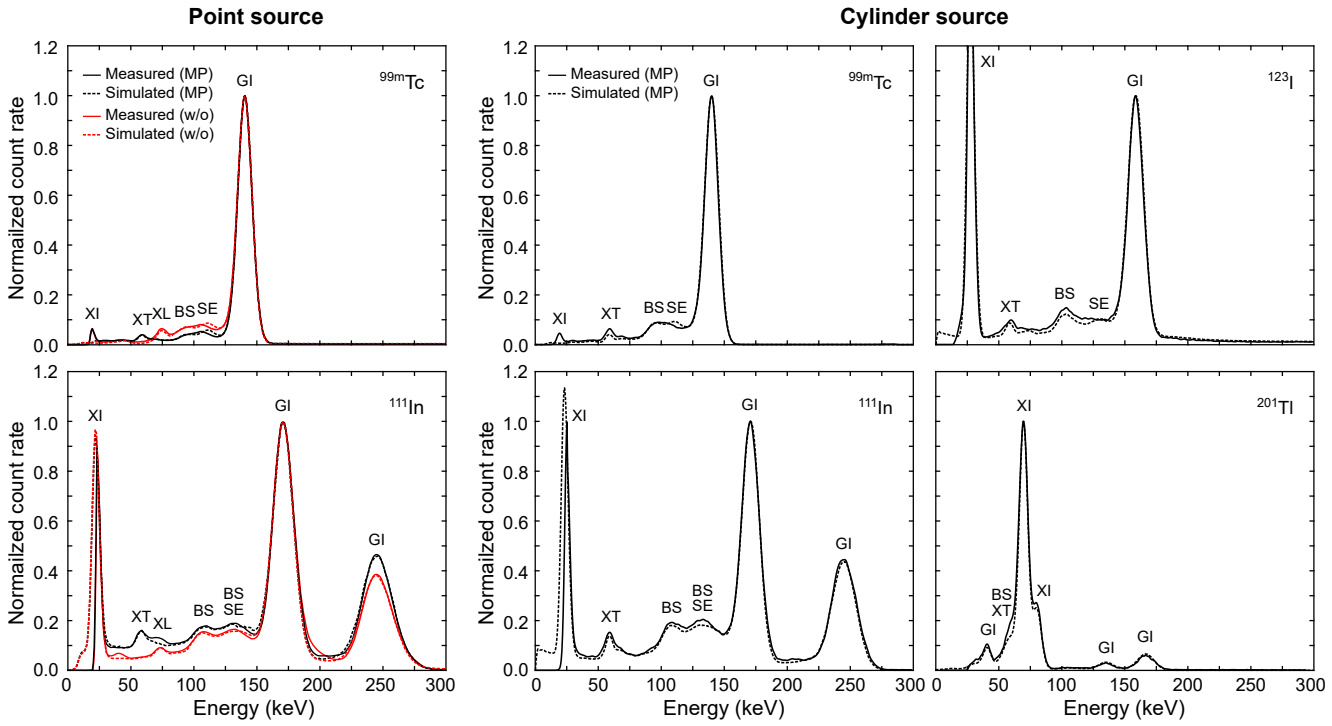

Fig. 6. Energy spectra of point and cylinder sources for different radioisotopes at the NanoSPECT/CT$^{\text{PLUS}}$. Simulated (dotted) and measured (solid) spectra with multi-pinhole apertures (MP) and without (w/o) were in excellent agreement for all isotopes and phantoms. Spectral components are isotope-specific gamma emission (GI), isotope-specific x-ray emission (XI), tungsten x-ray fluorescence (XT), lead x-ray fluorescence (XL), Compton backscatter (BS), and iodine single escape (SE).

calculated by minimizing the error fraction F_w of primary and secondary count rate $\dot{N}_p(w)$ and $\dot{N}_s(w)$:

$$F_w = \min\left\{\left\|\frac{\dot{N}_p(w)}{\dot{N}_s(w)^2}\right\|^2\right\} \tag{11}$$

Activity ratios: The mixing ratio of the simultaneously injected tracer ^{99m}Tc-NaTcO$_4$: ^{123}I-NaI was varied from 6 : 1 to 1 : 6. Considering the results from collimator and energy window optimization, the optimum activity ratio was determined by minimizing the total error function F_r for the given pharmakokinetic setting (Suppl. Table 1):

$$F_r = \min\left\{\left\|\sum_{i,o,t} F_{i,o,t}(r)\right\|^2\right\} \tag{12}$$

The total error fraction F_r is given by the sum of error fractions of isotopes i (^{99m}Tc-NaTcO$_4$, ^{123}I-NaI), target organs o (thyroid, salivary gland), and target times t (maximum uptake time t_{max}, biological half-life t_{bio}). The error fractions $F_{i,o,t}(r)$ were defined as crosstalk-to-primary ratio within the reconstructed region of interest. The delay for injection of the third tracer ^{99m}Tc-MDP was varied from 12 h to 30 h to find the shortest offset with background errors smaller than 1%.

Acquisition time: The acquisition time of one time frame was varied from 1 to 10 min using fractions of the simulated data. The signal-to-noise ratio (SNR) of ^{99m}Tc and ^{123}I was extracted from reconstructed images for thyroid, salivary gland and bone. The acquisition time was determined at which the SNR is greater than 1.5 for all organs at their individual biological half-life t_{bio} (Suppl. Table 1).

B. In Vivo - Quantitative Image Correction

Based on the in-silico results, 5 MBq/100 μl of ^{123}I-NaI and 20 MBq/75 μl of ^{99m}Tc-NaTcO$_4$ were simultaneously injected into the tail vein of a healthy female C57BL/6 mouse (age 110 days, weight 22.2 g) while dynamic SPECT scans were acquired (8×10 min time frames, 10×60 s gantry angulations, 40 angular projections, ^{99m}Tc 10% and ^{123}I 5% energy window, MP-105). Additional static SPECT scans were acquired after 8, 16, 24 and 42 h post injection (p.i.). After radioactive decay and physiological clearance of ^{99m}Tc-TcO$_4^-$, the bone tracer ^{99m}Tc-MDP was injected into the same mouse 10 min before the 24 h p.i. acquisition. The tomographic images were reconstructed using HiSPECT ($0.4 \times 0.4 \times 0.4$ mm^3, 3×3 iterations, 25% Gaussian smoothing). After reconstruction of time frames, ^{99m}Tc and ^{123}I SPECT images served as four-dimensional source model for Monte Carlo simulation. Using

TABLE III
PHOTOPEAK FRACTIONS FOR MULTI-ISOTOPE STUDIES USING CYLINDER PHANTOMS, MULTI-PINHOLE COLLIMATORS AND 20% ENERGY WINDOWS

	Energy window															
	Measurement (%)				Simulation (%)				Absolute difference (%)				Relative difference (%)			
Isotope	^{99m}Tc	^{111}In	^{123}I	^{201}Tl	^{99m}Tc	^{111}In	^{123}I	^{201}Tl	^{99m}Tc	^{111}In	^{123}I	^{201}Tl	^{99m}Tc	^{111}In	^{123}I	^{201}Tl
^{99m}Tc	100.0	1.1	30.8	7.1	100.0	0.7	30.9	5.6	0.0	-0.4	0.1	-1.5	0.0	-36.4	0.3	-21.1
^{111}In	16.9	100.0	51.0	65.7	15.9	100.0	50.8	65.9	-1.0	0.0	-0.2	0.2	-5.9	0.0	-0.4	0.3
^{123}I	39.0	83.0	100.0	98.0	38.1	83.3	100.0	95.6	-0.9	0.3	0.0	-2.4	-2.3	0.4	0.0	-2.4
^{201}Tl	4.9	10.7	9.7	100.0	5.4	10.8	10.6	100.0	0.5	0.1	0.9	0.0	10.2	0.9	9.3	0.0

TABLE IV
COUNT RATE SENSITIVITY PER DETECTOR HEAD USING POINT SOURCES AND 20% ENERGY WINDOWS

	Measurement (cps/MBq)		Simulation (cps/MBq)		Difference (%)	
Isotope	SP	MP	SP	MP	SP	MP
^{99m}Tc	41.2	191.1	41.7	204.2	1.2	6.9
^{111}In	62.3	288.6	68.1	316.1	9.4	9.5
^{123}I	40.2	186.5	37.8	169.1	-6.0	-9.4
^{201}Tl	44.5	206.5	43.3	201.4	-2.7	-2.4

SP Single-pinhole collimator, *MP* Multi-pinhole collimator

the simulation results, the planar images were corrected for attenuation, self-scatter and spectral crosstalk for re-reconstruction according to Equation 10.

VI. RESULTS

A. Energy Spectra

Fig. 6 shows energy spectra of point and cylinder sources for different isotopes. The agreement between simulated and measured spectra was excellent for all isotopes and phantoms. The energy response function and the associated photopeak widths were in good accordance. Subtle differences could be seen in lower energy spectral components caused by secondary processes, which might be relevant for multi-isotope applications using disadvantageous activity ratios.

The ^{99m}Tc point source simulations overestimated the iodine single escape peaks (SE; ~112 keV) with and without MP collimators by 16% and 11%, respectively. For the ^{111}In point source simulation with MP collimators, the lead x-ray fluorescence peak (XL, ~75 keV) was underestimated by 15%. In general, lead x-ray fluorescence that is primarily induced in the pyramid shielding was displaced by tungsten x-ray fluorescence if pinhole collimators were mounted.

The ^{99m}Tc cylinder source simulations underestimated the tungsten x-ray fluorescence peak (XT, ~59 keV) by 18% and overestimated the iodine single escape peak (SE, ~112 keV) by 14%. The simulated backscatter peaks for ^{111}In (BS, ~103 keV), ^{111}In (BS, ~125 keV), ^{123}I (BS, ~98 keV), and ^{201}Tl (BS, ~56 keV) cylinder sources were underestimated by 4, 6, 10, and 19%, respectively.

Table III summarizes the resulting errors for multi-isotope studies expressed as photopeak fractions. The absolute difference between measurement and simulation was below 2.4% for all isotope combinations. Relative differences are increased for energy windows with low count rates. Example reading: The simulation of an ^{111}In source (Table III, row) with a count rate of 1000 cps (100%) for the ^{111}In energy window will cause a spectral crosstalk of 159 cps (15.9%) to the ^{99m}Tc energy window (Table III, column). The relative and absolute difference between measured and simulated photopeak fraction was -1.0% and -5.9%, respectively.

B. Count Rate Performance

Fig. 7 shows the count rate performance and ^{99m}Tc pileup spectra of a NanoSPECT/CT^{PLUS} detector. The difference between measured and simulated absolute count rate, dead-time loss, and pileup loss was negligible with $0.8 \pm 4.7\%$, $1.1 \pm 4.5\%$, and $0.1 \pm 0.7\%$ (mean $\pm$ SD), respectively. The double- and triple-piled photopeaks are in good agreement between measurement and simulation. For count rates greater than 200 kcps, the measured single photopeaks were increasingly broadened and resulted in simulated energy resolution differences of -0.5, -0.7 and -1.3 keV FWHM for 200, 400 and 800 kcps, respectively. However, the resulting count rate deviations for a 20% energy window were negligible ($< 0.8\%$).

C. System Sensitivity

Table IV summarizes the absolute count rate sensitivities per detector head for different isotopes. Measured and simulated absolute sensitivities were in good agreement with errors below 10% for both SP and MP collimators.

Fig. 8 shows the normalized sensitivities for different positions within the gantry. The measured sensitivity distributions could be simulated accurately for SP ($< 2.5\%$) and MP collimators ($< 7.4\%$) throughout the entire FOV. Only for two detectors with MP collimators, the simulated sensitivity at the outermost axial position (Z = 15.0 mm) was up to 38.2% different from measurement due to very low count rate statistics.

In general, the sensitivity decreases with increasing distance to the detector for SP collimators. The combined SP sensitivity

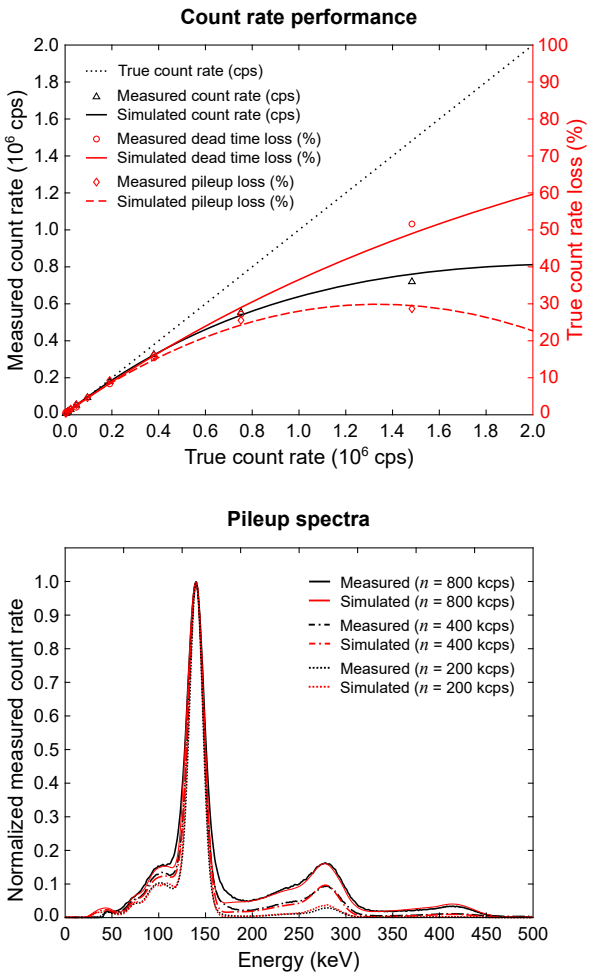

Fig. 7. Count rate performance and pileup spectra of the NanoSPECT/CT$^{\text{PLUS}}$ detector. The simulated dead-time model was in good agreement with measurements. The spectral photopeak broadening measured for extremely high count rates was not emulated in this study as it contributes only negligible count rate deviations.

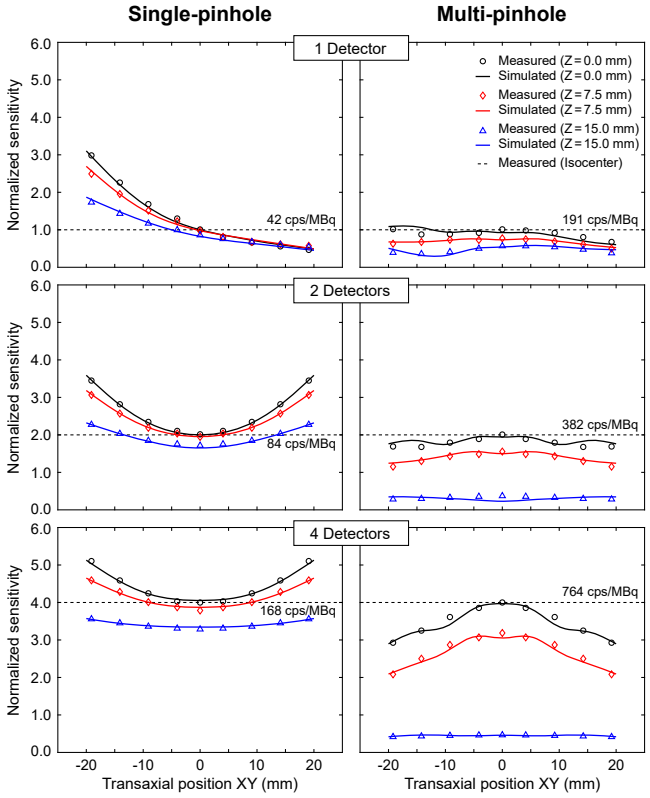

Fig. 8. Count rate sensitivity at various positions within the NanoSPECT/CT$^{\text{PLUS}}$. Simulated and measured profiles were in excellent agreement throughout the entire field of view. Multi-pinhole collimators improved absolute sensitivity by a factor of 4.5 and shifted the sensitivity focus to the isocenter. The sensitivities are normalized to the system sensitivity of one detector at the isocenter (dashed line).

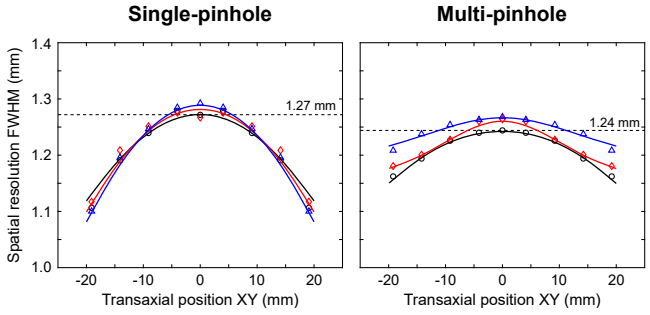

Fig. 9. Reconstructed spatial resolution at various positions within the NanoSPECT/CT$^{\text{PLUS}}$. Simulated and measured profiles were in excellent agreement throughout the entire field of view. Multi-pinhole collimators slightly decreased spatial resolution towards the periphery (legend see Fig. 8)

of multiple detectors shows its minimum at the axial central axis of the FOV. For MP collimators, in contrast, the sensitivity distribution is more homogeneous for one detector head and becomes highest at the isocenter of the FOV for multiple detectors. However, the axial sensitivity gradient is steeper for MP than for SP collimators but can be compensated with adapted table incrementation.

D. Spatial Resolution

The intrinsic spatial resolution of the nanoSPECT/CT$^{\text{PLUS}}$ was measured with 3.2 ± 0.2 mm FWHM. The simulated intrinsic spatial resolution was 0.7 ± 0.0 mm FWHM. According to the convolution theory for Gaussian distributions (Equation 7), planar images needed to be filtered with a $3.0 \times 3.0\,\text{mm}^2$ Gaussian kernel to match the measured spatial resolution (Suppl. Fig. 2).

Fig. 9 shows the reconstructed spatial resolution at different positions in the FOV. The measured reconstructed spatial resolution could be simulated accurately for SP ($< 0.9\%$) and MP ($< 2.2\%$) collimators within the entire FOV. MP collimators showed a more homogeneous distribution of spatial resolution in transaxial but not in axial direction.

E. Image Quality

Fig. 10 (top) shows reconstructed uniformity phantoms with low count statistics and angular undersampling for different acquisition modes. Uniformity, artifact pattern and noise propagation of the measured data could be simulated with high

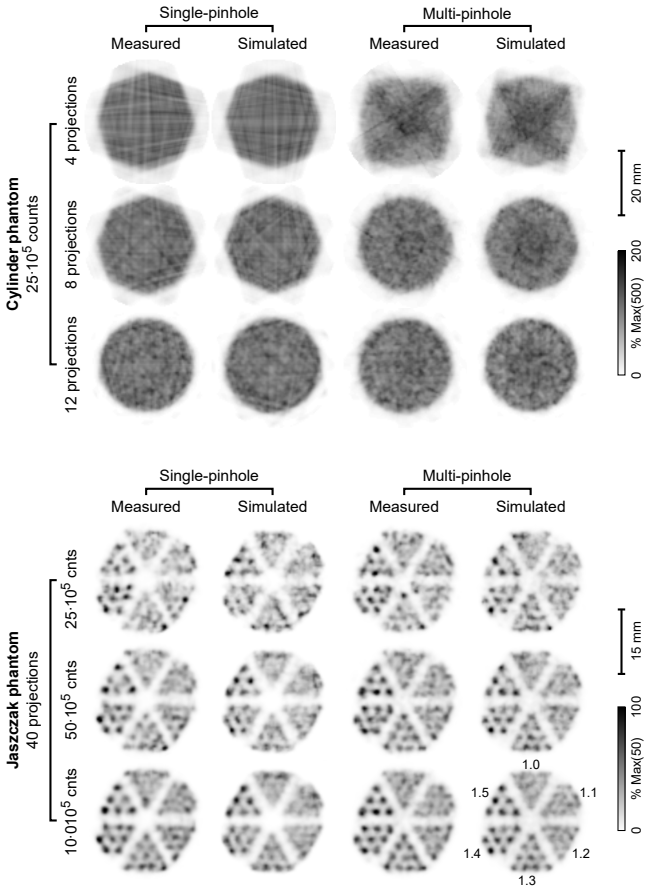

Fig. 10. Uniformity phantom and small-animal Jaszczak phantom acquired with the NanoSPECT/CT^{PLUS}. The system provides different stationary and semi-stationary modes for ultra-fast SPECT acquisitions, which could be replicated accurately in terms of uniformity, artifact pattern, noise propagation and quantification. Complex inhomogeneous activity distributions could be simulated with equivalent visual impression and spatial resolution over a wide range of noise levels.

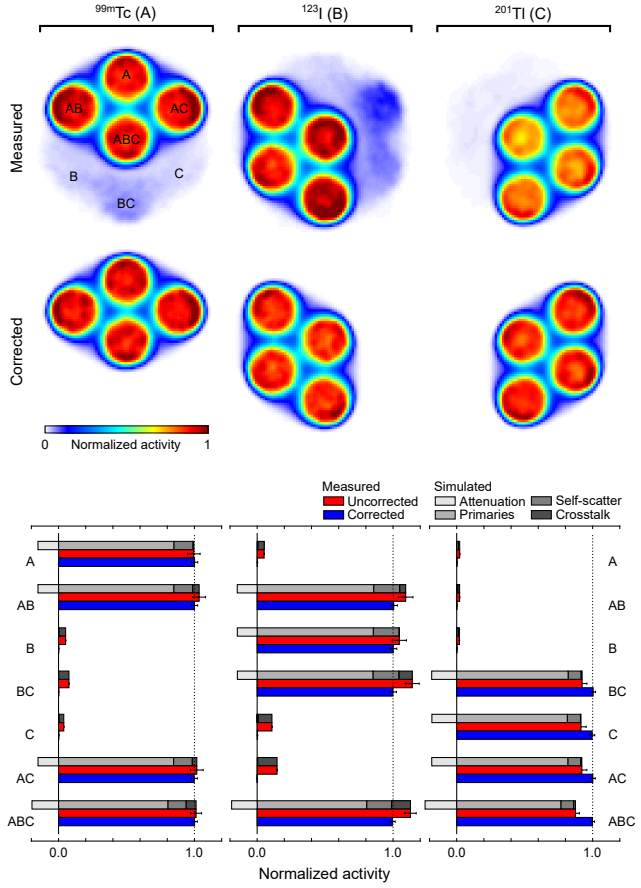

Fig. 11. Image reconstructions and component analysis of a multi-isotope experiment acquired with the NanoSPECT/CT^{PLUS}. Activity distributions and absolute count rates could be simulated accurately. Monte Carlo based correction of attenuation, self-scatter and spectral crosstalk improved quality and quantitative accuracy of the reconstructed images. In contrast to calibration methods, simulations provide spectrospatial information that can be used to increase image uniformity and contrast within the entire field of view.

accuracy. The simulation error of the uniformity and noise coefficients ranged from 1.7% to 8.6% and from 2.3% and 7.2%, respectively (Suppl. Table 2).

Fig. 10 (bottom) shows reconstructed Jaszczak phantoms with different count statistic and sufficient angular sampling (40 angular projections). Visual impression, reconstructed spatial resolution and noise propagation could be emulated accurately. The simulation error of the spatial resolution ranged from 1.5% to 3.8% (Suppl. Table 2).

F. Image Quantification

Fig. 11 shows image reconstructions of multiple simultaneously acquired isotopes before (top) and after (middle) model-based image reconstruction together with the corresponding image component analysis (bottom). The absolute count rates for the multi-isotope experiment could be simulated accurately with small deviations of 2.8%, -3.4% and -1.1% for ^{99m}Tc, ^{123}I and ^{201}Tl, respectively (gray bars).

Model-based correction of attenuation, self-scatter and spectral crosstalk improved both quantitative accuracy and image quality. The error of quantification could be reduced from a maximum of 7.7%, 14.7% and -8.5% to 0.5%, 0.6% and -0.4% for ^{99m}Tc, ^{123}I, ^{201}Tl, respectively (red vs. blue bars). Due to the spatiality of model-based image correction, images showed improved homogeneity, increased contrast and reduced background noise within the entire FOV. Self-scatter and spectral crosstalk was most prominent for ^{99m}Tc and ^{123}I while ^{201}Tl was most affected by attenuation.

G. In Silico - Protocol Optimization

The Monte Carlo model enabled full access to physical processes that could be used for refinement of the entire imaging chain. Virtualization of recurring pretrials could save 4 laboratory animals and 50 MBq of radioactivity per use case.

Collimators: Table V lists geometric specifications and simulated performance parameters of different multi-pinhole collimators. With a pinhole diameter of 1.5 mm, MP-105 showed the poorest spatial resolution (^{99m}Tc/^{123}I 1.16/1.17 mm FWHM). However, count rate sensitivities were high (^{99m}Tc/^{123}I 173/141 cps/MBq) and partial volume effect for the smallest target organ thyroid

TABLE V
SIMULATED SYSTEM PERFORMANCE PARAMETERS FOR AN IN-VIVO MOUSE EXPERIMENT USING DIFFERENT 9-PINHOLE COLLIMATORS

Multi-pinhole aperture	**105**	**125**	**106**	**116**
Geometry				
Pinhole diameter (mm)	1.5	0.8	1.0	0.5
FOV axial (mm)	22.0	22.0	14.0	14.0
FOV transaxial (mm)	60.0	30.0	30.0	16.0
FOV volume (cm^3)	22.8	11.4	4.6	2.5
Simulation for ^{99m}Tc				
Spatial resolution (mm)	1.16	0.82	0.69	0.62
Partial volume effect (Ø1.5 mm)	4.7%	3.6%	3.1%	2.8%
Partial volume effect (Ø5.0 mm)	1.4%	1.1%	0.9%	0.8%
Detector multiplexing	1.1%	5.2%	8.4%	15.8%
Collimator penetration	1.7%	2.3%	1.5%	1.9%
Sensitivity (cps/MBq)	173	74	186	70
FOV sensitivity (cps·cm^3/MBq)	3946	844	859	172
Simulation for ^{123}I				
Spatial resolution (mm)	1.17	0.86	0.73	0.66
Partial volume effect (Ø1.5 mm)	4.8%	3.7%	3.2%	3.0%
Partial volume effect (Ø5.0 mm)	1.4%	1.1%	1.0%	0.9%
Detector multiplexing	1.8%	5.9%	8.8%	16.4%
Collimator penetration	7.1%	10.9%	5.8%	10.9%
Sensitivity (cps/MBq)	141	72	156	67
FOV sensitivity (cps·cm^3/MBq)	3216	821	720	165

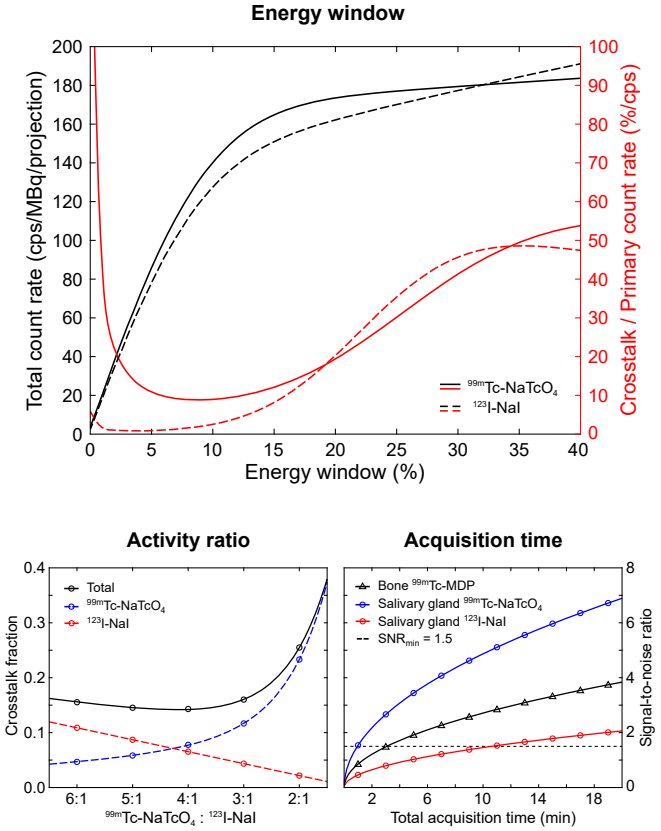

Fig. 12. Monte Carlo based optimization of imaging protocol parameters for a dual-isotope triple-tracer mouse experiment at the NanoSPECT/CT^{PLUS}. Monte Carlo simulations enabled full access to physical processes and could be used to refine the entire imaging chain. For the given experimental setup, ^{99m}Tc and ^{123}I energy windows of 10% and 5%, ^{99m}Tc-NaTcO$_4$: ^{123}I-NaI activity ratios of 4 : 1, and ^{99m}Tc-MDP injection delays of 24 h were found to be optimal.

(⌀1.5 mm) was acceptable (^{99m}Tc/^{123}I 4.7%/4.8%). The large transaxial FOV of 60 mm resulted in lowest multiplexing percentage (^{99m}Tc/^{123}I 1.1%/1.8%). Image reconstruction degrading perturbations, such as collimator penetration (^{99m}Tc/^{123}I 1.7%/7.1%) and spectrospatial double ambiguities were minimized. Therefore, the optimum collimator for the given experimental issue was found to be MP-105 as it provides sufficient spatial resolution, highest FOV sensitivity and lowest multiplexing percentage.

Energy windows: Fig. 12 (top) shows simulated count rates and crosstalk-to-primary fractions depending on energy window width. The crosstalk-to-primary fractions were minimzed to 8.8 and 0.8 %/cps at energy window widths of 8.9% and 3.6% for ^{99m}Tc and ^{123}I, respectively. Therefore, the energy windows for the given experimental setup were chosen to be 10% for ^{99m}Tc and 5% for ^{123}I.

Activity ratios: Fig. 12 (bottom left) shows spectral crosstalk fractions of ^{99m}Tc and ^{123}I for different mixing ratios. The overall error induced by spectral crosstalk was minimized to 14.2% at a ^{99m}Tc : ^{123}I mixing ratio of 3.9 : 1.0. As the injection volume for mice is limited to 200 μl per injection and the activity concentrations of ^{99m}Tc-NaTcO$_4$ and ^{123}I-NaI are limited to 250 and 50 MBq/ml due to the in-house radiochemical labeling process, optimum injection doses were calculated to be 20 MBq for ^{99m}Tc-NaTcO$_4$ and 5 MBq for ^{123}I-NaI, respectively.

Residual activity in the FOV after 12, 18, 24, 30 h p.i. was 2.9, 0.3, 0.1, 0.0 MBq ^{99m}Tc-NaTcO$_4$ and 13.6, 8.1, 5.4, 3.6 MBq ^{123}I-NaI. The induced background error for late ^{99m}Tc-MDP injection was 9.2, 2.7, 1.4, 0.9%. Therefore, a good delay for injection of ^{99m}Tc-MDP was found to be 24 h.

Acquisition time: Fig. 12 (bottom right) shows the signal-to-noise ratio of bone and salivary gland with increasing acquisition times. The predefined condition SNR $\geq$ 1.5 for all isotopes and target organs at t_{bio} was met after a minimum acquisition time of 10.6 min. The SNR was lowest for ^{123}I in the salivary gland. Thyroid SNR exceeded 73 and 38 for ^{99m}Tc-NaTcO$_4$ and ^{123}I-NaI due to high tracer uptake and small target volume. Therefore, the optimum acquisition time for the given experimental and radiopharmaceutical setup was chosen to be 10 min (10 angular projections, 60 s/projection, 4 detectors).

H. In Vivo - Quantitative Image Correction

Fig. 13 shows axial SPECT/CT image reconstructions over time and corresponding time activity curves of a dual-isotope in-vivo mouse experiment using ^{99m}Tc-NaTcO$_4$ and ^{123}I-NaI. Both tracers showed high uptake in thyroid and salivary gland with different clearance rates. Crosstalk from ^{123}I to ^{99m}Tc within the thyroid and salivary glands was 40.3% and 22.3% 10 min p.i. and 23.1% and 25.8% 90 min p.i., respectively.

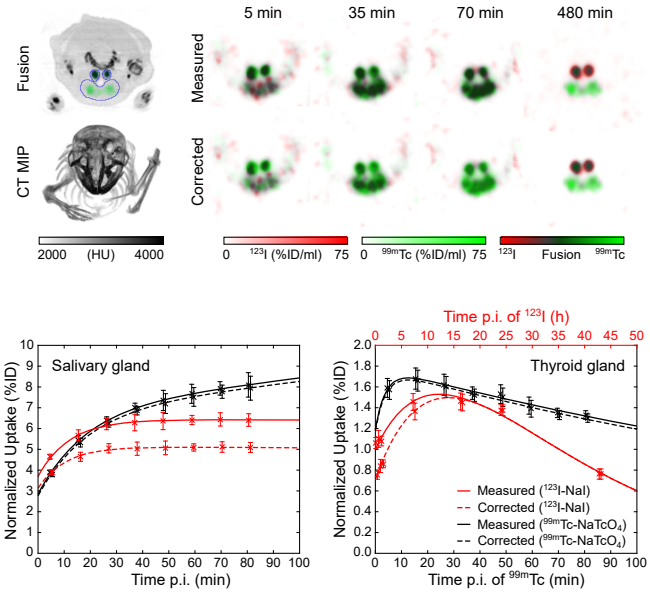

Fig. 13. Reconstructed images and time activity curves of an in-vivo experiment with simultaneously injected ^{123}I-NaI and ^{99m}Tc-NaTcO$_4$, both targeting thyroid and salivary glands. The Monte Carlo model was used for imaging protocol optimization and for spectrospatial crosstalk correction, which improved image quality as well as quantitative accuracy.

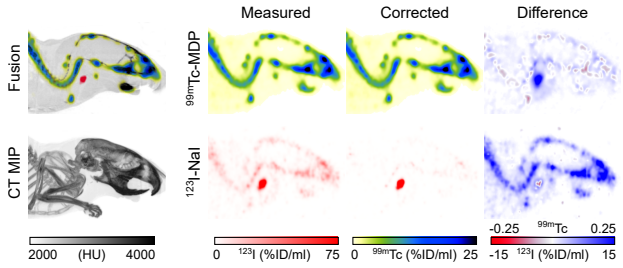

Fig. 14. Reconstructed SPECT/CT images of a dual-isotope in-vivo mouse experiment with ^{123}I-NaI and ^{99m}Tc-MDP. Model-based crosstalk correction improved quantitative accuracy and image quality most notably for ^{123}I.

Crosstalk from ^{99m}Tc to ^{123}I remained below 2.9% for all organs and time points. Therefore, model-based crosstalk correction improved quantitative accuracy most notably for ^{99m}Tc.

Fig. 14 shows sagittal SPECT/CT images of the dual-isotope in-vivo experiment with ^{99m}Tc-MDP and ^{123}I-NaI. Crosstalk from ^{99m}Tc to ^{123}I, observable as misclassified counts in bone, could be reduced from 94 to 34 kBq/ml applying model-based crosstalk correction. Crosstalk correction affected quantification of ^{123}I thyroid uptake (5.5%) and ^{99m}Tc bone uptake (0.7%) only slightly but improved visual reading due to reduced background noise.

VII. Discussion

The NanoSPECT/CT$^{\text{PLUS}}$ is a dedicated SPECT/CT system designed for high-resolution, high-sensitivity small animal imaging [22]. Its submillimeter spatial resolution is achieved by pinhole collimation able to overcome the poor intrinsic resolution of scintillation detectors by object magnification. Multiple pinholes per collimator can raise count rate sensitivities above the capabilities of parallel-hole collimators [23]. However, due to the magnifying nature of pinholes, slight inaccuracies in modeling can cause reconstruction artifacts and quantitative misrepresentations. This particularly holds true for multiplexed multi-pinhole collimators, where multiple projections share valuable detector surface to maximize utilization. In this study, pinhole positions, pinhole angulations and acceptance angles were initially unknown and were obtained by point source measurements and trigonometric calculations [16]. The geometric accuracy of our model could be validated by simulation of large-sized cylinder phantoms, which did not show uniformity divergences or relevant reconstruction artifacts (Fig. 10).

Besides pinhole collimators and detector material, seemingly unimportant parts of the gantry needed to be modeled with care. In small animal imaging, source scatter is reduced [24] and hardware scatter turned out to be the predominant source of error [8]. It has been shown, that particularly the back compartment of a detector head contributes a significant portion of detected scatter [15]. Underestimation of this backscatter inevitably leads to quantitative inaccuracy most notably for multi-energetic single-isotope and multi-isotope investigations with several energy windows acquired.

The established Monte Carlo model was able to simulate energy spectra for different isotopes very close to the measurements within the energy range of 25 to 500 keV (Fig. 6). This not only confirmed the integrity of the geometric model including the back compartment but also the validity of the extended energy response function that was implemented in this study. As determined in previous investigations, the simplified $1/\sqrt{E}$-model provided by GATE does not sufficiently replicate the measured response function of a real SPECT device for imaging situations at the system performance limits [8]. It only considers variations of photoelectrons released at the photocathode of the photomultiplier and neglects other signal forming parameters such as the variance of photomultiplier gain or associated electronics. The introduced advanced energy response module, by contrast, incorporates a non-theoretical measured energy response function into the simulation. Still, slight deviations could be observed for secondary processes such as characteristic x-ray fluorescence and backscatter (Fig. 6). The iodine single escape peak, for instance, was overestimated while collimator x-ray fluorescence was slightly underestimated. Bonifacio *et al.* observed similar discrepancies of characteristic x-ray fluency for radiological applications and concluded that this might be related to the ionization process or the atomic relaxation model implemented in GEANT4 [25]. Backscatter underestimations, on the other hand, could be observed for cylinder sources but not for point sources. This might be related to the simplified cylinder model that disregarded asymmetric filling geometry at the outer axial boundaries of the measured phantoms.

Due to excellent spectral accuracy, simulation errors for isotope-specific count rate sensitivities remained below 10%

for all conditions (Table IV). Spectral crosstalk factors for multi-isotope investigations could be well reproduced with deviations below 2.5% (Table III). Moreover, sensitivity losses due to dead time and pileup could be modeled accurately (Fig. 7) with deviations below 1.1%. Only the spectral photopeak broadening measured for extremely high count rates has not been reproduced but can be neglected as the related simulation errors remained below 1%.

The count rate sensitivities, but also the reconstructed spatial resolution, were investigated in dependence on the collimator distance in order to confirm the tomographic properties of the Monte Carlo model (Fig. 8 and 9). Both single- and multi-pinhole simulations were in good accordance with measurements. The errors for sensitivity remained below 7.4% and for spatial resolution below 2.2% within the entire FOV. The multi-pinhole collimators showed higher deviations in sensitivity compared to the single-pinhole collimators, which might indicate imprecise source positioning during measurement or a minor model discrepancy of the pinhole acceptance angles.

However, uniformity and Jaszczak phantoms could be well reproduced (Fig. 10). Their three-dimensional image reconstructions showed almost identical spatial resolution, image uniformity, artifact pattern, noise propagation and quantitation compared to those from measurement. This also holds true for investigations at the system performance range limits. Angular undersampling, for instance, acquired in stationary, semi-stationary and fast-helical mode, showed almost identical streak artifact pattern and geometric distortions for simulation and measurements. The noise propagation of ultra-low count rate acquisitions could be modeled precisely by incorporation of real measured spectral and temporal dark count data into the simulation. This especially considers irregular noise patterns caused by cosmic radiation ($< 1\%$) [26], electronics dark current (5-40% $\propto E$) [27] and ^{210}Pb contamination of the radiation shielding (60-95% $\propto E$) [28]. Here, the ^{210}Pb β^- decay product ^{210}Bi emits high-energy β^- radiation (1.2 MeV), which induces bremsstrahlung and Pb x-ray fluorescence (Fig. 4). ^{210}Pb perturbation was found to be most prominent close to the lead septum between SPECT and CT gantry (Fig. 5).

In this study, we established a Monte Carlo model that was able to mimic energy spectra, planar and reconstructed images of the NanoSPECT/CT$^{\text{PLUS}}$ with highest qualitative and quantitative accuracy for both standard and non-standard experiments. The model can be used to optimize multi-isotope studies with regard to activity ratios, energy windows and scatter corrections. It may be further used to assess period limits of longitudinal studies where count rates change from high to ultra-low levels over time. Monte Carlo investigations are able to reduce costs and primarily the number of animals sacrificed.

VIII. Conclusion

In this work, we developed a highly accurate Monte Carlo model of the NanoSPECT/CT$^{\text{PLUS}}$ and established a comprehensive framework for simulation, data conversion and image reconstruction. The model has been validated for different performance measurements with emphasis on high-accuracy for non-standard multi-isotope applications operating near the system range limits. It may be used for cost-effective optimization of imaging hardware, acquisition protocols and quantitative reconstructions at the edge of SPECT system technological feasibility.

Acknowledgment

The authors gratefully acknowledge funding from the Technologiestiftung Berlin (TSB) and the German Research Foundation (GRK 2260 - BIOQIC, CRC 1340 - Matrix in Vision). We would like to thank Dr. Janet F. Eary, M.D. (US National Institutes of Health/NCI/DCTD) for the careful editing of the manuscript.

References

[1] B. L. Franc, P. D. Acton, C. Mari, and B. H. Hasegawa, "Small-animal SPECT and SPECT/CT: Important tools for preclinical investigation", *J. Nucl. Med.*, vol. 49, no. 10, pp. 1651–1663, Sep. 2008.

[2] I. Buvat and I. Castiglioni, "Monte Carlo simulations in SPET and PET", *Quart. J. Nucl. Med.*, vol. 46, no. 1, pp. 48–61, Mar. 2002.

[3] A. Sadremomtaz and Z. Telikani, "Capabilities of the Monte Carlo simulation codes for modeling of a small animal SPECT camera", *Nucl. Med. and Mol. Imag.*, vol. 52, no. 4, pp. 303–310, Aug. 2018.

[4] S. Agostinelli, J. Allison, K. Amako, J. Apostolakis, H. Araujo, P. Arce *et al.*, "GEANT4 - A simulation toolkit", *Methods Phys. Res. A, Accel. Spectrom. Detect. Assoc. Equip.*, vol. 506, no. 3, pp. 250–303, Jul. 2003.

[5] S. Jan, G. Santin, D. Strul, S. Staelens, K. Assié, D. Autret *et al.*, "GATE: A simulation toolkit for PET and SPECT", *Phys. Med. Biol.*, vol. 49, no. 19, pp. 4543–4561, Oct. 2004.

[6] C.-L. Chen, Y. Wang, J. J. S. Lee, and B. M. W. Tsui, "Toward quantitative small animal pinhole SPECT: Assessment of quantitation accuracy prior to image compensations", *Mol. Imag. Biol.*, vol. 11, no. 3, pp. 195–203, May 2009.

[7] C. M. Finucane, I. Murray, J. K. Sosabowski, J. M. Foster, and S. J. Mather, "Quantitative accuracy of low-count SPECT imaging in phantom and in vivo mouse studies", *Int. J. Mol. Imag.*, vol. 2011, p. 1–8, Mar. 2011.

[8] M. Lukas, A. Kluge, N. Beindorff, and W. Brenner, "Multi-Isotope capabilities of a small animal multi-pinhole SPECT system", *J. Nucl. Med.*, vol 61, no. 1, pp. 152–161, Jan. 2020.

[9] H. M. Deloar, H. Watabe, T. Aoi, and H. Iida, "Evaluation of penetration and scattering components in conventional pinhole SPECT: Phantom studies using Monte Carlo simulation", *Phys. Med. Biol.*, vol. 48, no. 8, pp. 995–1008, Apr. 2003.

[10] G. S. P. Mok, Y. Du, Y. Wang, E. C. Frey, and B. M. W. Tsui, "Development and validation of a Monte Carlo simulation tool for multi-pinhole SPECT", *Mol. Imag. Biol.*, vol. 12, no. 3, pp. 295–304, Jun. 2010

[11] C.-L. Chen, Y. Wang, J. J. S. Lee, and B. M. W. Tsui. "Integration of SimSET photon history generator in GATE for efficient Monte Carlo simulations of pinhole SPECT", *Med. Phys.*, vol. 35, no. 7, pp. 3278–3284, Jun. 2008

[12] S. Lee, J. Gregor, and D. Osborne, "Development and validation of a complete GATE model of the Siemens Inveon trimodal imaging platform", *Mol. Imag.*, vol. 12, no. 7, pp. 1–13, Oct. 2013

[13] C. Lange, I. Apostolova, M. Lukas, K. Huang, F. Hofheinz, B. Gregor-Mamoudou *et al.*, "Performance evaluation of stationary and semi-stationary acquisition with a non-stationary small animal multi-pinhole SPECT system", *Mol. Imag. and Biol.*, vol. 16, no. 3, pp. 311–316, Jun. 2014.

[14] R. Brun and F. Rademakers, "ROOT - An object oriented data analysis framework", *Nucl. Instrum. Methods Phys. Res. A, Accel. Spectrom. Detect. Assoc. Equip.*, vol. 389, no. 1-2, pp. 81–86, Apr. 1997.

[15] E. Rault, S. Staelens, R. Van Holen, J. De Beenhouwer, and S. Vandenberghe, "Accurate Monte Carlo modelling of the back compartments of SPECT cameras", *Phys. Med. Biol.*, vol. 56, no. 1, pp. 87–104, Jan. 2011.

[16] D. Bequé, J. Nuyts, P. Suetens, and G. Bormans, "Optimization of geometrical calibration in pinhole SPECT", *IEEE Trans. Med. Imag.*, vol. 24, no. 2, pp. 90–180, Feb. 2005.

[17] E. B. Martin, A. Williams, T. Richey, A. Stuckey, R. E. Heidel, S. J. Kennel *et al.*, "Comparative evaluation of p5+14 with SAP and peptide p5 by dual-energy SPECT imaging of mice with AA amyloidosis", *Sci. Rep.*, vol. 6, p. 22695, Mar. 2016.

[18] S. H. Dresel, M. P. Kung, X. F. Huang, K. Plössl, C. Hou, S. K. Meegalla *et al.*, "Simultaneous SPECT studies of pre- and postsynaptic dopamine binding sites in baboons", *J. Nucl. Med.*, vol. 40, no. 4, pp. 660–666, 1999.

[19] B. Xu, M. Shokeen, G. P. Sudlow, S. E. Harpstrite, K. Liang, P. P. Cheney *et al.*, "Utilizing the multiradionuclide resolving power of SPECT and dual radiolabeled single molecules to assess treatment response of tumors", *Mol. Imag. Biol.*, vol. 17, no. 5, pp. 671–679, Oct. 2015.

[20] N. Beindorff, A. Bartelheimer, K. Huang, M. Lukas, C. Lange, E. L. Huang *et al.*, "Normal values of thyroid uptake of 99m-technetium pertechnetate SPECT in mice with respect to age, sex, and circadian rhythm", *NuklearMedizin*, vol. 57, no. 5, pp. 181–189, Sep. 2018.

[21] E. L. Huang, I. G. Steffen, M. Lukas, K. Huang, J. R. Aschenbach, J. F. Eary *et al.*, "Normal values for parotid gland and submandibular-sublingual salivary gland complex uptake of 99m-technetium pertechnetate using SPECT in mice with respect to age, sex, and circadian rhythm", *NuklearMedizin*, vol. 58, no. 1, pp. 39–49, Feb. 2019.

[22] N. Schramm, J. Hoppin, C. Lackas, F. V. Roelf, and M. de Jong, "The NanoSPECT: A high-sensitivity multi-pinhole SPECT system with submillimeter (nanoliter) spatial resolution for imaging small rodents", *J. Nucl. Med.*, vol. 47, no. suppl. 1, p. 233P, 2006.

[23] R. A. De Kemp, F. H. Epstein, C. Catana, B. M. W. Tsui, and E. L. Ritman, "Small-animal molecular imaging methods", *J. Nucl. Med.*, vol. 51, no. suppl 1, pp. 18S–32S, May 2010.

[24] A. B. Hwang, B. L. Franc, G. T. Gullberg, and B. H. Hasegawa, "Assessment of the sources of error affecting the quantitative accuracy of SPECT imaging in small animals", *Phys. Med. Biol.*, vol. 53, no. 9, pp. 2233–2252, May 2008.

[25] D. A. B. Bonifacio, H. M. Murata, and M. Moralles, "Monte Carlo simulation of x-ray spectra in diagnostic radiology and mammography using Geant4", *Proc. Int. Nucl. Atlantic Conf. (INAC)*, p. 4886, Sep. 2005.

[26] W. Preusse, and S. Unterricker, "The contribution of cosmic ray muons to the background spectrum of gamma ray spectrometers", *Nucl. Instrum. Methods Phys. Res. B, Beam Interact. Mater. At.*, vol. 94, no. 4, pp. 569–574, Dec. 1994

[27] K. Lung, K. Arisaka, A. Bargetzi, P. Beltrame, A. Cahill, T. Genma *et al.*, "Characterization of the Hamamatsu R11410-10 3-in. photomultiplier tube for liquid xenon dark matter direct detection experiments", *Nucl. Instrum. Methods Phys. Res. A, Accel. Spectrom. Detect. Assoc. Equip.*, vol. 696, pp. 32–39, Dec. 2012

[28] W. A. Kolb, "Die Eigenaktivität von Blei", *Proc. 1st Int. Congr. Radiat. Protection*, vol. 2, pp. 1385–1390, 1986

[29] L. Chen, B. M. W. Tsui, and G. S. P. Mok, "Design and evaluation of two multi-pinhole collimators for brain SPECT", *Ann. Nucl. Med.*, vol. 31, no. 8, pp. 636–648, Oct. 2017

[30] Y. Du, E. C. Frey, W. T. Wang, C. Tocharoenchai, W. H. Baird, and B. M. W. Tsui, "Combination of MCNP and SimSET for Monte Carlo simulation of SPECT with medium- and high-energy photons", *IEEE Trans. Nucl. Sci.*, vol. 49, no. 3, pp. 668–674, Jun. 2002

SUPPLEMENTAL TABLES

SUPPL. TABLE I
PHARMACOKINETIC PARAMETERS OF THE SIMULATED 4D MOUSE MODEL

	Thyroid		Salivary gland		Bone
Kinetic parameter	**^{99m}Tc-NaTcO$_4$**	**^{123}I-NaI**	**^{99m}Tc-NaTcO$_4$**	**^{123}I-NaI**	**^{99m}Tc-MDP**
Maximum uptake (%ID$_{max}$)	2	6	4	4	25
Maximum uptake time (min)	30	900	80	70	10
Biological half-life (min)	140	4200	180	300	1440
Organ volume (mm^3)	4	4	132	132	1800

SUPPL. TABLE II
IMAGE QUALITY PARAMETERS FOR DIFFERENT ACQUISITION MODES

	Measurement		Simulation		Difference (%)	
Parameter	**SP**	**MP**	**SP**	**MP**	**SP**	**MP**
Uniformity						
4 projections	0.35	0.67	0.32	0.63	-8.6	-6.0
8 projections	0.45	0.56	0.43	0.54	-4.4	-3.6
12 projections	0.52	0.59	0.51	0.58	-1.9	-1.7
Noise						
4 projections	10.41	3.44	11.16	3.64	7.2	5.8
8 projections	8.32	5.25	8.72	5.42	4.8	3.2
12 projections	6.78	5.19	7.04	5.31	3.8	2.3
Resolution (mm)						
$25{\cdot}10^5$ cnts	1.33	1.31	1.31	1.26	-1.5	-3.8
$50{\cdot}10^5$ cnts	1.33	1.29	1.31	1.26	-1.5	-2.3
$100{\cdot}10^5$ cnts	1.31	1.28	1.28	1.25	-2.3	-2.3

SP Single-pinhole aperture, *MP* Multi-pinhole aperture

SUPPLEMENTAL FIGURES

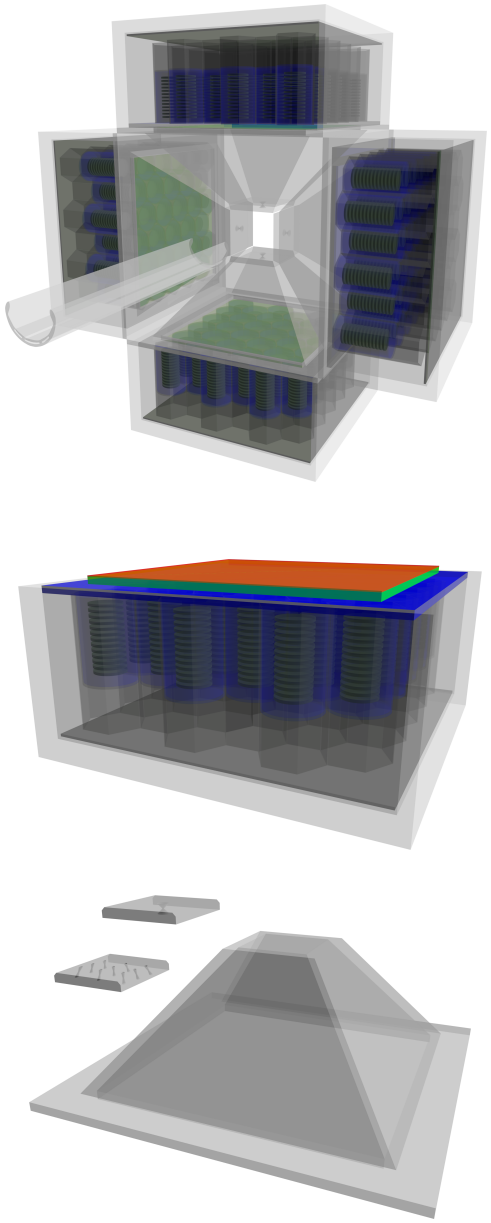

Suppl. Fig. 1. Three-dimensional rendering of SPECT gantry, detector head and pyramid-pinhole collimators of the NanoSPECT/CT^{PLUS}. The SPECT gantry consists of four detector heads equipped with thallium doped sodium iodide scintillation crystals, which are coupled to 132 position-sensitive photomultiplier tubes via glass light guides.

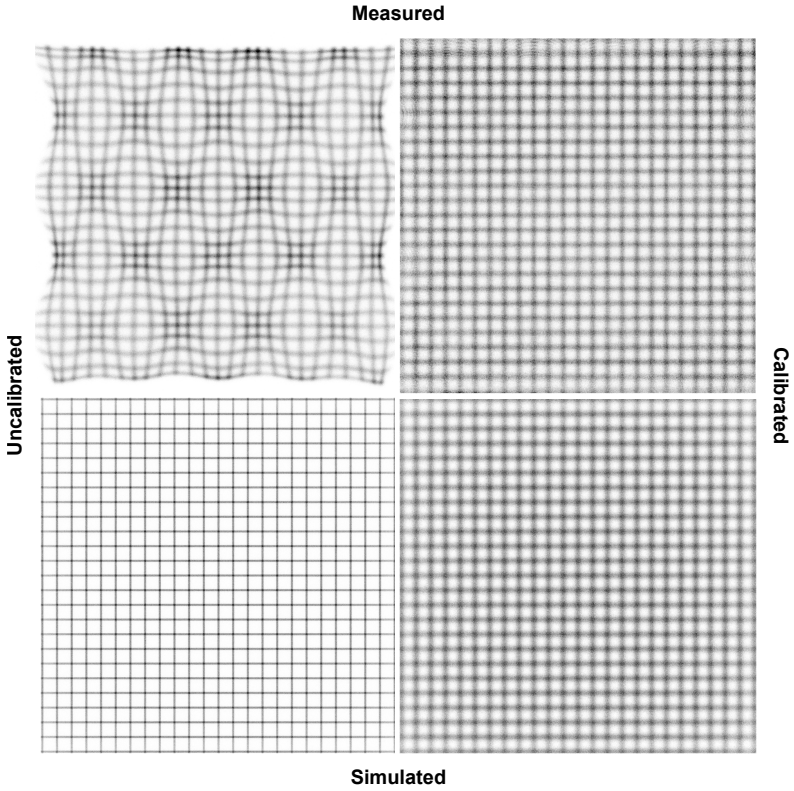

Suppl. Fig. 2. Planar images of measured and simulated flood sources covered by a lead slit plate for derivation of the intrinsic spatial resolution. The simulated resolution was 0.7 mm FWHM and needed to be filtered with a $3.0 \times 3.0\,\mathrm{mm}^2$ Gaussian kernel to conform the measured resolution of 3.2 mm FWHM for $^{99\mathrm{m}}$Tc after calibration.

Statutory Declaration

I, Mathias Lukas, by personally signing this document in lieu of an oath, hereby affirm that I prepared the submitted dissertation on the topic ...

Multi-Isotope Multi-Pinhole Spect Imaging in Small Laboratory Animals - Experimental Measurements and Monte Carlo Simulations (English)

Multi-Isotope Multi-Pinhole Spect Bildgebung in kleinen Labortieren - Experimentelle Messungen und Monte Carlo Simulationen (German)

... independently and without the support of third parties, and that I used no other sources and aids than those stated.

All parts which are based on the publications or presentations of other authors, either in letter or in spirit, are specified as such in accordance with the citing guidelines. The sections on methodology (in particular regarding practical work, laboratory regulations, statistical processing) and results (in particular regarding figures, charts and tables) are exclusively my responsibility.

Furthermore, I declare that I have correctly marked all of the data, the analyses, and the conclusions generated from data obtained in collaboration with other persons, and that I have correctly marked my own contribution and the contributions of other persons. I have correctly marked all texts or parts of texts that were generated in collaboration with other persons.

My contributions to any publications to this dissertation correspond to those stated in the below joint declaration made together with the supervisor. All publications created within the scope of the dissertation comply with the guidelines of the ICMJE (International Committee of Medical Journal Editors; www.icmje.org) on authorship. In addition, I declare that I shall comply with the regulations of Charité – Universitätsmedizin Berlin on ensuring good scientific practice.

I declare that I have not yet submitted this dissertation in identical or similar form to another faculty.

The significance of this statutory declaration and the consequences of a false statutory declaration under criminal law (§§ 156, 161 of the German Criminal Code) are known to me.

Date	Signature

Contribution Declaration

Publication 1 | Experimental Measurements

Lukas M, Kluge A, Beindorff N, Brenner W. Multi-Isotope Capabilities of a Small-Animal Multi-Pinhole SPECT System. *J Nucl Med.* 2020 Jan; 61:152-161.

Impact factor: 10.057
Share: 90 %

Contributions:
- Development of hypothesis, study concept and design (Lukas)
- Theoretical pre-calculations and experimental pre-studies (Lukas)
- Procurement of laboratory resources (Lukas, Beindorff, Brenner)
- Development of software for processing proprietary data formats (Lukas)
- Calibration of measurement systems (Lukas)
- Experimental measurements and image acquisitions (Lukas)
- Data sampling, preparation, processing and analysis (Lukas)
- Evaluation and interpretation of the results (Lukas, Kluge)
- Drafting of the manuscript including all texts, figures, and tables (Lukas)
- Proofreading and revision of the manuscript (Kluge, Beindorff, Brenner)

Publication 2 | Monte Carlo Simulations

Lukas M, Kluge A, Beindorff N, Brenner W. Accurate Monte Carlo Modeling of Small-Animal Multi-Pinhole SPECT for Non-Standard Multi-Isotope Applications. *IEEE Trans Med Imaging.* 2021 Sep; 40:2208-2220.

Impact factor: 11.037
Share: 90 %

Contributions:
- Development of hypothesis, study concept and design (Lukas)
- Development of software for processing proprietary data formats (Lukas)
- Development of software framework for multi-isotope image reconstruction (Lukas)
- Development of geometric and electronic Monte Carlo models (Lukas)
- Procurement of laboratory resources (Lukas, Beindorff, Brenner)
- Calibration of measurement systems (Lukas)
- Experimental measurements and Monte Carlo simulations (Lukas)
- Animal experiments and animal keeping (Beindorff, Lukas)
- Data sampling, preparation, processing and analysis (Lukas)
- Evaluation and interpretation of the results (Lukas, Kluge)
- Drafting of the manuscript including all texts, figures, and tables (Lukas)
- Proofreading and revision of the manuscript (Kluge, Beindorff, Brenner)

Mathias Lukas

Prof. Dr. Winfried Brenner

Curriculum Vitae

The curriculum vitae does not appear in the electronic version of the thesis for reasons of data protection.

List of Publications

Journal Articels

1. **Lukas M**, Kluge A, Beindorff N, and Brenner W. Accurate Monte Carlo Modeling of Small-Animal Multi-Pinhole SPECT for Non-Standard Multi-Isotope Applications. *IEEE Trans Med Imaging.* 2021 Sep; 40:2208–20. (Impact Factor 11.037)
2. Schwarz C, Lange C, Benson GS, Horn N, Wurdack K, **Lukas M**, Buchert R, Wirth M, and Floel A. Severity of Subjective Cognitive Complaints and Worries in Older Adults Are Associated With Cerebral Amyloid-β Load. *Front Aging Neurosci.* 2021 Aug; 13:675583. (Impact Factor 5.702)
3. Ippoliti M, **Lukas M**, Brenner W, Schatka I, Furth C, Schaeffter T, Makowski MR, and Kolbitsch C. Respiratory motion correction for enhanced quantification of hepatic lesions in simultaneous PET and DCE-MR imaging. *Phys Med Biol.* 2021 Apr; 66:95012. (Impact Factor 4.174)
4. Graef J, Senger C, Wetz C, Baur ADJ, Kluge A, **Lukas M**, Rogasch JMM, Walter-Rittel TC, Kohnert D, Makowski RM, Acker G, Huang K, Budach V, Amthauer H, Schatka I, and Furth C. Shortened Tracer Uptake Time in (68)Ga-DOTATOC-PET of Meningiomas Does Not Impair Diagnostic Accuracy and PET Volume Definition. *Diagnostics (Basel).* 2020 Dec; 10:1084. (Impact Factor 3.706)
5. Dorau-Rutke V, Huang K, **Lukas M**, Schulze MO, Rosner C, Gregor-Mamoudou B, Steffen IG, Brenner W, and Beindorff N. (18)F-sodium fluoride bone deposition quantitation with PET in Mice: Variation with age, sex, and circadian rhythm. *Nuklearmedizin.* 2020 Dec; 59:428–37. (Impact Factor 1.379)
6. Mohan AM, **Lukas M**, Albrecht J, Dorau-Rutke V, Koziolek EJ, Huang K, Prasad S, Brenner W, and Beindorff N. Relationship of Renal Function in Mice to Strain, Sex and (177)Lutetium-Somatostatin Receptor Ligand Treatment. *Nuklearmedizin.* 2020 Sep; 59:381–6. (Impact Factor 1.379)
7. **Lukas M**, Kluge A, Beindorff N, and Brenner W. Multi-Isotope Capabilities of a Small-Animal Multi-Pinhole SPECT System. *J Nucl Med.* 2020 Jan; 61:152–61. (Impact Factor 10.057)
8. Rogasch JMM, Suleiman S, Hofheinz F, Bluemel S, **Lukas M**, Amthauer H, and Furth C. Reconstructed spatial resolution and contrast recovery with Bayesian penalized likelihood reconstruction (Q.Clear) for FDG-PET compared to time-of-flight (TOF) with point spread function (PSF). *EJNMMI Phys.* 2020 Jan; 7:2. (Impact Factor 3.309)
9. Acker G, Meinert F, Conti A, Kufeld M, Jelgersma C, Nguyen P, Kluge A, **Lukas M**, Loebel F, Pasemann D, Kaul D, Budach V, Vajkoczy P, and Senger C. Image-Guided Robotic Radiosurgery for Treatment of Recurrent Grade II and III Meningiomas. A Single-Center Study. *World Neurosurg.* 2019 Nov; 131:e96–e107. (Impact Factor 1.829)
10. Ippoliti M, **Lukas M**, Brenner W, Schaeffter T, Makowski MR, and Kolbitsch C. 3D nonrigid motion correction for quantitative assessment of hepatic lesions in DCE-MRI. *Magn Reson Med.* 2019 Nov; 82:1753–66. (Impact Factor 3.635)
11. Senger C, Conti A, Kluge A, Pasemann D, Kufeld M, Acker G, **Lukas M**, Gruen A, Kalinauskaite G, Budach V, Waiser J, and Stromberger C. Robotic stereotactic ablative radiotherapy for renal cell carcinoma in patients with impaired renal function. *BMC Urol.* 2019 Oct; 19:96. (Impact Factor 1.592)

12. Liesche F, **Lukas M**, Preibisch C, Shi K, Schlegel J, Meyer B, Schwaiger M, Zimmer C, Foerster S, Gempt J, and Pyka T. (18)F-Fluoroethyl-tyrosine uptake is correlated with amino acid transport and neovascularization in treatment-naive glioblastomas. *Eur J Nucl Med Mol Imaging.* 2019 Sep; 46:2163–8. (Impact Factor 7.081)

13. Acker G, Kluge A, **Lukas M**, Conti A, Pasemann D, Meinert F, Nguyen PTA, Jelgersma C, Loebel F, Budach V, Vajkoczy P, Furth C, Baur ADJ, and Senger C. Impact of (68)Ga-DOTATOC PET/MRI on robotic radiosurgery treatment planning in meningioma patients: first experiences in a single institution. *Neurosurg Focus.* 2019 Jun; 46:E9. (Impact Factor 3.647)

14. Rogasch JMM, Albers J, Steinkrueger FL, **Lukas M**, Wedel F, Amthauer H, and Furth C. Point Spread Function Reconstruction for Integrated (18)F-FET PET/MRI in Patients With Glioma: Does It Affect SUVs and Respective Tumor-to-Background Ratios? *Clin Nucl Med.* 2019 Apr; 44:e280–e285. (Impact Factor 6.622)

15. Huang EL, Steffen IG, **Lukas M**, Huang K, Aschenbach JR, Eary JF, Brenner W, and Beindorff N. Normal Values for Parotid Gland and Submandibular-Sublingual Salivary Gland Complex Uptake of (99m)Technetium Pertechnetate using SPECT in Mice with Respect to Age, Sex, and Circadian Rhythm. *Nuklearmedizin.* 2019 Feb; 58:39–49. (Impact Factor 1.087)

16. Huang K, **Lukas M**, Steffen IG, Lange C, Huang EL, Dorau V, Brenner W, and Beindorff N. Normal Values of Renal Function measured with (99m)Technetium Mercaptoacetyltriglycine SPECT in Mice with Respect to Age, Sex, and Circadian Rhythm. *Nuklearmedizin.* 2018 Dec; 57:224–33. (Impact Factor 1.270)

17. Beindorff N, Bartelheimer A, Huang K, **Lukas M**, Lange C, Huang EL, Aschenbach JR, Eary JF, Steffen IG, and Brenner W. Normal Values of Thyroid Uptake of (99m)Technetium Pertechnetate SPECT in Mice with Respect to Age, Sex, and Circadian Rhythm. *Nuklearmedizin.* 2018 Sep; 57:181–9. (Impact Factor 1.270)

18. Maughan NM, Eldib M, Faul D, Conti M, Elschot M, Knesaurek K, Leek F, Townsend D, DiFilippo FP, Jackson K, Nekolla SG, **Lukas M**, Tapner M, Parikh PJ, and Laforest R. Multi institutional quantitative phantom study of yttrium-90 PET in PET/MRI: the MR-QUEST study. *EJNMMI Phys.* 2018 Apr; 5:7. (Impact Factor 3.475)

19. Preibisch C, Shi K, Kluge A, **Lukas M**, Wiestler B, Goettler J, Gempt J, Ringel F, Al Jaberi M, Schlegel J, Meyer B, Zimmer C, Pyka T, and Foerster S. Characterizing hypoxia in human glioma: A simultaneous multimodal MRI and PET study. *NMR Biomed.* 2017 Nov; 30:e3775. (Impact Factor 3.031)

20. Golkowski D, Merz K, Mlynarcik C, Kiel T, Schorr B, Lopez-Rolon A, **Lukas M**, Jordan D, Bender A, and Ilg R. Simultaneous EEG-PET-fMRI measurements in disorders of consciousness: an exploratory study on diagnosis and prognosis. *J Neurol.* 2017 Sep; 264:1986–95. (Impact Factor 3.783)

21. Shi K, Fuerst S, Sun L, **Lukas M**, Navab N, Foerster S, and Ziegler SI. Individual refinement of attenuation correction maps for hybrid PET/MR based on multi-resolution regional learning. *Comput Med Imaging Graph.* 2017 Sep; 60:50–7. (Impact Factor 2.435)

22. Schulz J, Rohracker M, Stiebler M, Goldschmidt J, Stoeber F, Noriega M, Pethe A, **Lukas M**, Osterkamp F, Reineke U, Hoehne A, Smerling C, and Amthauer H. Proof of Therapeutic Efficacy of a (177)Lu-Labeled Neurotensin Receptor 1 Antagonist in a Colon Carcinoma Xenograft Model. *J Nucl Med.* 2017 Jun; 58:936–41. (Impact Factor 7.439)

23. Goettler J, **Lukas M**, Kluge A, Kaczmarz S, Gempt J, Ringel F, Mustafa M, Meyer B, Zimmer C, Schwaiger M, Foerster S, Preibisch C, and Pyka T. Intra-lesional spatial correlation of static and dynamic FET-PET parameters with MRI-based cerebral blood volume in patients with untreated glioma. *Eur J Nucl Med Mol Imaging.* 2017 Mar; 44:392–7. (Impact Factor 7.704)

24. Ladefoged CN, Law I, Anazodo U, St Lawrence K, Izquierdo-Garcia D, Catana C, Burgos N, Cardoso MJ, Ourselin S, Hutton B, Merida I, Costes N, Hammers A, Benoit D, Holm S, Juttukonda M, An H, Cabello J, **Lukas M**, Nekolla SG, Ziegler SI, Fenchel M, Jakoby B, Casey ME, Benzinger T, Hojgaard L, Hansen AE, and Andersen FL. A multi-centre evaluation of eleven clinically feasible brain PET/MRI attenuation correction techniques using a large cohort of patients. *Neuroimage.* 2017 Feb; 147:346–59. (Impact Factor 5.426)

25. Cabello J, **Lukas M**, Kops ER, Ribeiro A, Shah NJ, Yakushev I, Pyka T, Nekolla SG, and Ziegler SI. Comparison between MRI-based attenuation correction methods for brain PET in dementia patients. *Eur J Nucl Med Mol Imaging.* 2016 Nov; 43:2190–200. (Impact Factor 7.277)

26. Wiestler B, Kluge A, **Lukas M**, Gempt J, Ringel F, Schlegel J, Meyer B, Zimmer C, Foerster S, Pyka T, and Preibisch C. Multiparametric MRI-based differentiation of WHO grade II/III glioma and WHO grade IV glioblastoma. *Sci Rep.* 2016 Oct; 6:35142. (Impact Factor 4.259)

27. Kluge A, **Lukas M**, Toth V, Pyka T, Zimmer C, and Preibisch C. Analysis of three leakage-correction methods for DSC-based measurement of relative cerebral blood volume with respect to heterogeneity in human gliomas. *Magn Reson Imaging.* 2016 May; 34:410–21. (Impact Factor 2.225)

28. Tillner F, Thute P, Loeck S, Dietrich A, Fursov A, Haase R, **Lukas M**, Rimarzig B, Sobiella M, Krause M, Baumann M, Buetof R, and Enghardt W. Precise image-guided irradiation of small animals: a flexible non-profit platform. *Phys Med Biol.* 2016 Apr; 61:3084–108. (Impact Factor 2.742)

29. Cabello* J, **Lukas* M**, Foerster S, Pyka T, Nekolla SG, and Ziegler SI. MR-based Attenuation Correction Using Ultrashort-Echo-Time Pulse Sequences in Dementia Patients. *J Nucl Med.* 2015 Mar; 56:423–9. (Impact Factor 5.849)

30. Mallinckrodt B von, Thakur M, Weng A, Gilabert-Oriol R, Durkop H, Brenner W, **Lukas M**, Beindorff N, Melzig MF, and Fuchs H. Dianthin-EGF is an effective tumor targeted toxin in combination with saponins in a xenograft model for colon carcinoma. *Future Oncol.* 2014 Nov; 10:2161–75. (Impact Factor 2.477)

31. Lange C, Apostolova I, **Lukas M**, Huang K, Hofheinz F, Gregor-Mamoudou B, Brenner W, and Buchert R. Performance Evaluation of Stationary and Semi-Stationary Acquisition with a Non-Stationary Small Animal Multi-Pinhole SPECT System. *Mol Imaging Biol.* 2014 Jun; 16:311–6. (Impact Factor 2.774)

32. Haeckel A, Appler F, Figge L, Kratz H, **Lukas M**, Michel R, Schnorr J, Zille M, Hamm B, and Schellenberger E. XTEN-Annexin A5: XTEN Allows Complete Expression of Long-Circulating Protein-Based Imaging Probes as Recombinant Alternative to PEGylation. *J Nucl Med.* 2014 Mar; 55:508–14. (Impact Factor 6.160)

33. Maus J, Hofheinz F, Schramm G, Oehme L, Beuthien-Baumann B, **Lukas M**, Buchert R, Steinbach J, Kotzerke J, and Hoff J van den. Evaluation of PET quantification accuracy in vivo. Comparison of measured FDG concentration in the bladder with urine samples. *Nuklearmedizin.* 2014 Mar; 53:67–77. (Impact Factor 1.494)

34. Apostolova I, Wunder A, Dirnagl U, Michel R, Stemmer N, **Lukas M**, Derlin T, Gregor-Mamoudou B, Goldschmidt J, Brenner W, and Buchert R. Brain perfusion SPECT in the mouse: Normal pattern according to gender and age. *Neuroimage.* 2012 Dec; 63:1807–17. (Impact Factor 6.252)

35. Zuchner T, Schumer F, Berger-Hoffmann R, Mueller K, **Lukas M**, Zeckert K, Marx J, Hennig H, and Hoffmann R. Highly Sensitive Protein Detection Based on Lanthanide Chelates with Antenna Ligands Providing a Linear Range of Five Orders of Magnitude. *Anal Chem.* 2009 Nov; 81:9449–53. (Impact Factor 5.214)

Conference Proceedings

1. Mohan AM, **Lukas M**, Albrecht J, Huang K, Brenner W, and Beindorff N. Kidney function in mice with respect to strain, sex and (177)Lu-DOTATOC treatment. *Nuklearmedizin.* 2020 Apr; 59:P127.

2. Albers J, Senger C, Kluge A, **Lukas M**, Acker G, Baur A, Huang K, Thiele F, Schatka I, Amthauer A, and Furth C. Einfluss der Uptake-Zeit in der (68)Ga-DOTATOC PET/MRT auf das Planungszielvolumen von Meningeomen vor stereotaktischer Strahlentherapie. *Nuklearmedizin.* 2020 Apr; 59:P111.

3. Rogasch J, Hofheinz F, Suleiman S, **Lukas M**, Amthauer H, and Furth C. Does Bayesian penalized likelihood reconstruction (Q.Clear) for FDG-PET always outperform image quality of OSEM-based reconstruction? *Eur J Nucl Med Mol Imaging.* 2019 Oct; 46:EP855.

4. Senger C, Kluge A, **Lukas M**, Conti A, Pasemann D, Budach V, Vajkoczy P, Bauer A, and Acker G. Impact of (68)Ga-DOTATOC PET/MRI on robotic radiosurgery treatment planning in meningioma patients: First experiences in a single institution. *Strahlenther Onkol.* 2019 May; 195:P15–7.

5. Rogasch J, Albers J, Steinkrüger F, **Lukas M**, Wedel F, Amthauer H, and Furth C. Point spread function (PSF) reconstruction for integrated F18-FET-PET/MRI in patients with glioma: Does it affect standardized uptake values and respective tumor-to-background ratios? *Nuklearmedizin.* 2019 Mar; 58:P73.

6. Suleiman S, Rogasch J, **Lukas M**, Brenner W, Amthauer H, and Furth C. Potential for acquisition time reduction using Bayesian penalized likelihood reconstruction (Q.Clear) for clinical FDG-PET/CT: Intraindividual comparison with PSF+TOF and OSEM+TOF. *Nuklearmedizin.* 2019 Mar; 58:V35.

7. Beindorff N, Steinemann G, Prasad S, **Lukas M**, Koziolek E, Hoepfner M, and Brenner W. Chorioallantoic membrane assay of chicken eggs as a replacement method for preclinical radionuclide imaging of tumors. *Nuklearmedizin.* 2018 Mar; 87:V117.

8. Beindorff N, Bartelheimer A, Huang K, **Lukas M**, Lange C, Huang E, Steffen I, and Brenner W. (99m)Tc-pertechnetate thyroid uptake correlates with physiological changes in estrous cycle in mice. *Nuklearmedizin.* 2018 Mar; 87:V57.

9. **Lukas M**, Kluge A, Shi K, Pyka T, Foerster S, and Preibisch C. Multimodal PET/MR imaging of hypoxia in human high-grade glioma. *Nuklearmedizin.* 2018 Mar; 87:V42.

10. Schau F, Wedel F, **Lukas M**, Furth C, Amthauer H, Hoehne R, and Brenner W. Initiale Erfahrungen mit (18)F-FET-Hirnuntersuchungen am PET/MRT. *Nuklearmedizin.* 2018 Mar; 87:TV12.

11. Pyka T, Gempt J, **Lukas M**, Schlegel J, Ringel F, Foerster S, Zimmer C, Preibisch C, and Schwaiger M. Stereotactic histologic correlation of dynamic FET-PET/MRI in untreated high-grade glioma patients. *Eur J Nucl Med Mol Imaging.* 2017 Sep; 44:EP497.

12. Beindorff N, Dorau V, Huang K, Rosner C, Schulze O, **Lukas M**, Lange C, Koziolek E, Gregor-Mamoudou B, Steffen I, and Brenner W. Longitudinal PET studies on bone uptake of (18)F-fluoride in healthy mice with respect to age, sex and circadian rhythm. *Eur J Nucl Med Mol Imaging.* 2017 Sep; 44:EP187.

13. Beindorff N, Broenner A, Huang E, Huang K, **Lukas M**, Lange C, Steffen I, and Brenner W. Longitudinal SPECT studies on thyroid uptake in mice over a period of 24 months with respect to age, sex and circadian rhythm. *Eur J Nucl Med Mol Imaging.* 2016 Sep; 43:EP663.

14. Pyka T, Göttler J, **Lukas M**, Kluge A, Gempt J, Ringel F, Zimmer C, Schwaiger M, Förster S, and Preibisch C. Intra- and inter-dividual correlation of simultaneously acquired 18F-fluorethyltyrosine PET and perfusion MRI parameters in patients with untreated glioma. *J Nucl Med.* 2016 May; 57:184.

15. Goettler J, Kluge A, **Lukas M**, Kaczmarz S, Gempt J, Ringel F, Mustafa M, Schwaiger M, Zimmer C, Foerster S, Preibisch C, and Pyka T. Intra- And Inter-Individual Association of FET-PET- and MR-Perfusion-Parameters in Untreated Glioma. *Proc Intl Soc Mag Reson Med 24.* 2016 May; 24:1387.

16. Preibisch C, **Lukas M**, Kluge A, Zimmer C, Foerster S, and Pyka T. Characteristics of Apparent Relative Oxygen Extraction Fraction (rOEF) in Human High Grade Glioma. *Proc Intl Soc Mag Reson Med 24.* 2016 May; 24:4189.

17. Cabello J, **Lukas M**, Rota Kops E, Ribeiro A, Shah J, Yakushev I, Nekolla S, and Ziegler S. Comparison of MR-based Attenuation Correction Methods for Brain PET. *Nuklearmedizin.* 2016 Jan; 55:V112.

18. Huang K, Steffen I, **Lukas M**, Lange C, Rosner C, Brenner W, and Beindorff N. Longitudinal SPECT studies on kidney function in mice over a period of 24 months with respect to age, sex and circadian rhythm. *Nuklearmedizin.* 2016 Jan; 55:P44.

19. Heimann U, **Lukas M**, Bartel C, Schatka I, Schreiter V, and Schreiter N. Neue Methode zur patientenindividuellen Quantifizierung des Leber-Lungenshunts vor SIR-Therapie. *Nuklearmedizin.* 2016 Jan; 55:V41.

20. Pyka T, Goettler J, **Lukas M**, Kluge A, Gempt J, Ringel F, Mustafa M, Zimmer C, Schwaiger M, Foerster S, and Preibisch C. Simultane FET-PET/MR zur praetherapeutischen Charakterisierung von Gliomen: Korrelation zwischen statischen und dynamischen PET-Parametern und MR-Perfusion. *Nuklearmedizin.* 2016 Jan; 55:V36.

21. Huang K, Steffen I, **Lukas M**, Lange C, Rosner C, Brenner W, and Beindorff N. The influence of age, sex and circadian rhythm on kidney function in mice measured by (99m)Tc-MAG3 SPECT. *Eur J Nucl Med Mol Imaging.* 2015 Oct; 42:P226.

22. Preibisch C, **Lukas M**, Kluge A, Keinath S, Toth V, Shi K, Pyka T, and Foerster S. Multimodal MR/PET imaging for characterization of hypoxia in human glioblastoma. *Proc Intl Soc Mag Reson Med 23.* 2015 May; 23:480.

23. **Lukas M**, Kluge A, Cabello J, Preibisch C, and Nekolla S. Reliability of MR sequences used for attenuation correction in PET/MR. *Proc Intl Soc Mag Reson Med. 23.* 2015 May; 23:3426.

24. Kluge A, **Lukas M**, Toth V, Foerster S, Zimmer C, and Preibisch C. Comparison of different leakage-correction methods for DSC-based CBV measurements in human gliomas. *Proc Intl Soc Mag Reson Med 23.* 2015 May; 23:3059.

25. Rota Kops E, Ribeiro A, Caldeira L, Hautzel H, **Lukas M**, Antoch G, Lerche C, and Shah J. Attenuation correction for hybrid MR/PET scanners: a comparison study. *EJNMMI Physics.* 2015 May; 2:A38.

26. Beindorff N, Broenner A, **Lukas M**, Lange C, Heimann U, Huang K, Steffen I, and Brenner W. Significant impact of age, gender, and circadian rhythm on bone uptake in mice. *Nuklearmedizin.* 2015 Mar; 54:P45.

27. Cabello J, **Lukas M**, Foerster S, Pyka T, Nekolla S, and Ziegler S. MR-Based Attenuation Correction Using UTE Pulse Sequences in Dementia Patients. *Proc Eur Soc for Mol Imaging 10.* 2015 Mar; 10:273.

28. Broenner A, Beindorff N, **Lukas M**, Heimann U, Huang K, Steffen I, and Brenner W. (99m)Tc-MDP bone uptake in healthy mice with respect to age, gender, and circadian rhythm. *Eur J Nucl Med Mol Imaging.* 2014 Oct; 41:P782.

29. Broenner A, **Lukas M**, Huang K, Heimann U, Steffen I, Brenner W, and Beindorff N. The influence of age, gender and circadian rhythm on (99m)Tc-pertechnetate thyroid uptake in mice. *Eur J Nucl Med Mol Imaging.* 2014 Oct; 41:P730.

30. **Lukas M** and Ziegler S. Signal stability of MR sequences used for attenuation correction in PET/MR. *Abstractband der 45. Jahrestagung der DGMP.* 2014 Sep; 45:P56.

31. Pyka T, Keinath S, **Lukas M**, Shi K, Toth V, Gempt J, Ringel F, Zimmer C, Schwaiger M, Ziegler S, Preibisch C, and Foerster S. Characterization of intratumoral heterogeneity in glioma by simultaneous dynamic (18)F-FET-PET/MR. A pilot study. *Nuklearmedizin.* 2014 Jan; 53:P69.

32. Lange C, **Lukas M**, Apostolova I, Gregor-Mamoudou B, Michel R, Brenner W, and Buchert R. Stationary and semi-stationary acquisition mode in small animal multi-pinhole SPECT: impact on spatial resolution, noise propagation and overall image quality. *Nuklearmedizin.* 2013 Jan; 52:V138.

33. Apostolova I, Buchert R, **Lukas M**, Michel R, Rosner C, Prasad V, Marnitz S, Koehler C, and Brenner W. Combined PET with (18)F-FDG and (15)O-water for treatment planning in advanced cervical carcinoma: a pilot study. *Mol Imaging Biol.* 2012 Feb; 14:P810.

34. Apostolova I, **Lukas M**, Goldschmidt J, Brenner W, and Buchert R. Brain perfusion SPECT in the mouse: physiologic pattern according to gender and age. *Mol Imaging Biol.* 2012 Sep; 14:P039.

35. Langner J, Hofheinz F, Schramm G, Oehme L, Beuthien-Baumann B, **Lukas M**, Buchert R, Steinbach J, and Hoff J van den. A novel method for in-vivo evaluation of quantification accuracy in PET. *Nuklearmedizin.* 2012 Jan; 51:V192.

36. Tillner F, Thute P, Hietschold V, Khaless A, **Lukas M**, Rimarzig B, Rothe G, Sobiella M, and Enghardt W. Bildgefuehrtes Praezisionsbestrahlungsgeraet fuer Kleintiere (SAIGRT) - vom Konzept zur praktischen Umsetzung. *Abstractband der 43. Jahrestagung der DGMP.* 2012 Sep; 43:P84.

37. Apostolova I, Teichgraeber L, Stemmer N, **Lukas M**, Goldschmidt J, Wunder A, Brenner W, and Buchert R. Quantitative brain perfusion SPECT in the mouse with (99m)Tc-HMPAO. *Mol Imaging Biol.* 2012 Feb; 14:P744.

38. Apostolova I, Rudolph I, **Lukas M**, Steffen I, Rohwer N, Dupuy E, Wunder A, Cramer T, Buchert R, and Brenner W. Time-course of CT contrast enhancement by two novel nanoparticle-based contrast agents in comparison to eXIA T160 in normal mice and mice with hepatocellular carcinoma. *Mol Imaging Biol.* 2012 Feb; 14:P720.

Acknowledgments

Hereby, I would like to express my gratitude to everyone who contributed to this work. Without support, this thesis would not have been possible.

Many thanks to Prof. Winfried Brenner and Dr. Nicola Beindorff for their incentive motivation and continuous support. Thank you for sharing your expertise and for being enduring patient.

Many thanks also to Dr. Ralph Buchert and Dr. Anne Kluge for their insightful comments and competent help. I really enjoyed your deliberations and brilliant ideas.

Finally, I would like to thank Janet F. Eary, M.D., for careful revision of all our manuscripts.